Design, development and application of protein-templated gold nanoclusters in biosensing of glutathione, sodium and potassium ions

By

WONG XIN YI

Under the advisory of

Dr. Kasturi Muthoosamy

Prof. Dr. Sivakumar Manickam

Prof. Dr. Arben Merkoçi

A PhD thesis submitted in fulfilment of the requirements for the degree of Doctor of Philosophy in Chemical Engineering

DECEMBER 2020

Abstract

Protein-templated gold nanoclusters (AuNCs) are emerging nanomaterials with diverse applications in biomedical fields. AuNCs display discrete energy levels, large Stokes shift, good water solubility, distinctive fluorescence properties, high photostability and biocompatibility. These features make AuNCs a perfect candidate for imaging, biosensing and theranostics in the cellular and molecular level.

This project aims to develop AuNCs-based platform tools for biosensing applications. First, a facile and optimised protocol for the fabrication of BSA/AuNCs is developed. The protocol requires shorter synthesis time (only 6 h) and lower protein amount (only 20 mg mL^{-1}), while giving higher QY (10.62 %). Functionalisation of reduced graphene oxide (rGO) with folic acid (FA) is performed using EDC/NHS cross-linking agents and their interaction after loading with BSA/AuNCs is demonstrated. Finally, a fluorescence "turn-off" sensing strategy is developed using the as-synthesised FA-rGO-BSA/AuNCs for sensitive and selective detection of glutathione. The strategy requires incubation time as short as 2 min only to observe a linear range from 0 to 1.75 μM and LOD of 0.1 μM towards GSH under pH 7.4.

Following this, RNase A/AuNCs is synthesised using the optimised protocol. An RNase A/AuNCs-based platform is used to detect the presence of metal ions in aqueous solution. Besides, the activity of RNase A protein after the formation of RNase A/AuNCs is studied. It is found that 50.8 % of RNase A remain active in RNase A/AuNCs. The addition of FA-rGO onto RNase A/AuNCs serve as a "turn-on" and "turn-off" fluorescence sensor for biosensing of sodium and potassium ions.

Lastly, since electroanalytical methods are fast, simple, sensitive and cost-effective, electrochemical approaches have been used, as a proof-of-concept, to investigate the interaction between FA and folate receptor, on a graphene platform. With this, laser scribed graphene oxide (GO) and GO-FA electrodes have been prepared using different

approaches for the studies. $Ru(NH_3)_6Cl_3$ is found to be more suitable to be used as the redox probe in the present electrochemical measurements than Fe^{2+}/Fe^{3+}. Meanwhile, different GO platforms have been studied using various substrates.

Overall, these facile fabricated AuNCs-based biosensors pave the way and highlight the possibilities to detect important biomarkers in cancer cells, presenting potential nanotheranostic applications in biological detection and clinical diagnosis.

Keywords: gold nanoclusters, protein templates, folic acid, graphene, biosensing, laser scribing

Graphical abstracts

1. Integrating gold nanoclusters, folic acid and reduced graphene oxide for nanosensing of glutathione based on "turn-off" fluorescence

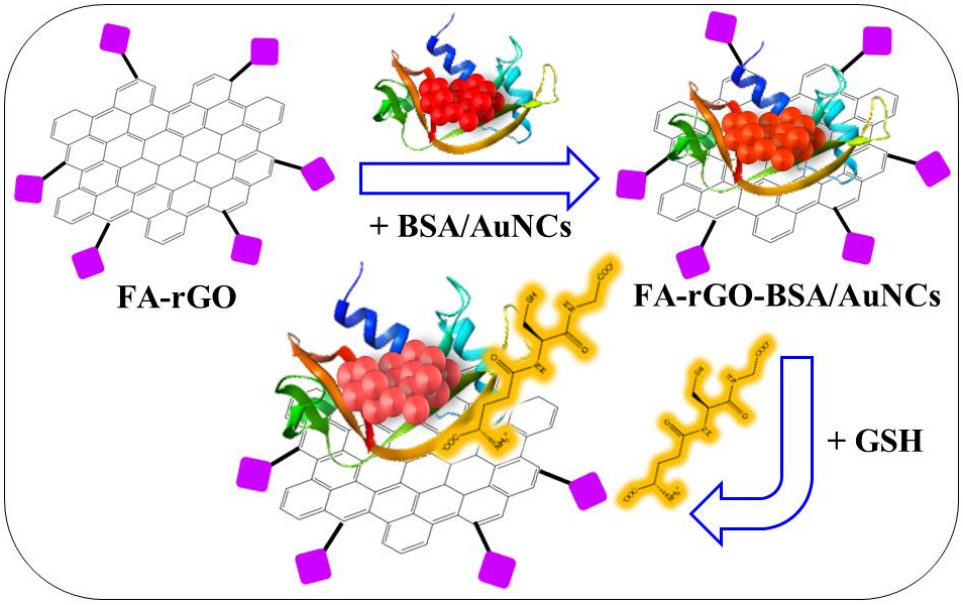

2. Fluorescence "turn-off/turn-on" biosensing of metal ions by gold nanoclusters, folic acid and reduced graphene oxide

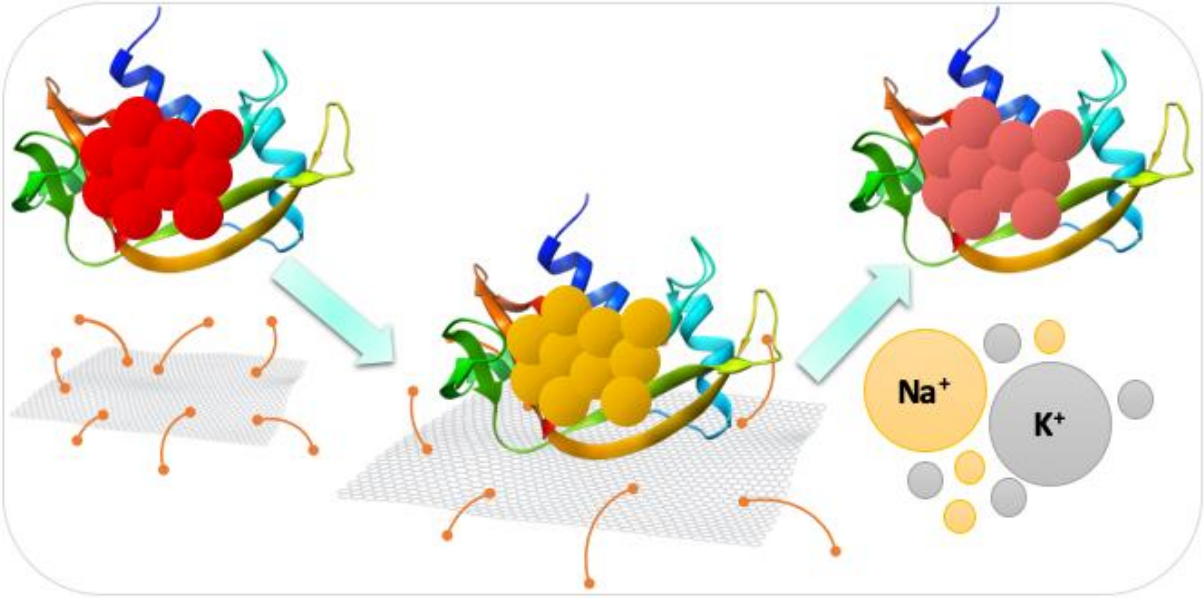

3. Development of an electrochemical sensing platform for the determination of folate receptor using laser scribed graphene electrodes

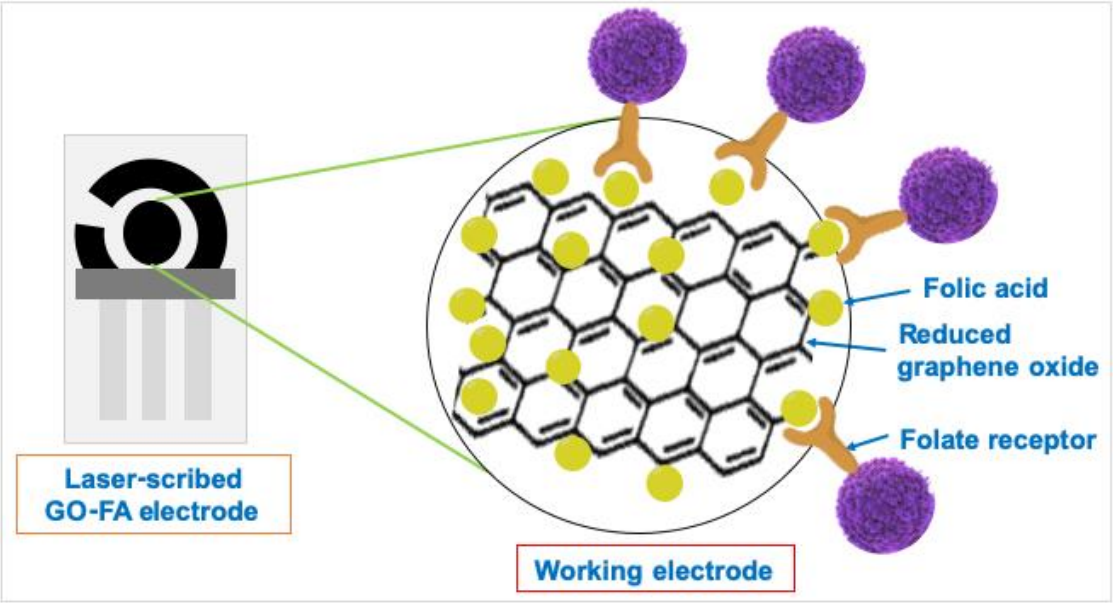

List of publications

1. **Wong, X.Y.**, Sena-Torralba, A., Alvarez-Diduk, R., Muthoosamy, K. & Merkoçi, A. Nanomaterials for nanotheranostics: tuning their properties according to disease needs. ACS Nano 14, 2585–2627 (2020) (IF 14.588) (As attached in Appendix)
2. **Wong, X. Y.** *et al.* Integrating gold nanoclusters, folic acid and reduced graphene oxide for nanosensing of glutathione based on "turn-off" fluorescence. Scientific Reports 11, 2375 (2021) (IF 3.998) (As attached in Appendix)
3. **Wong, X. Y.** *et al*. Fluorescence "turn-off/turn-on" biosensing of metal ions by gold nanoclusters, folic acid and reduced graphene oxide. *Review under second revision @ Analytica Chimica Acta* (IF 5.977)

Acknowledgements

I would like to express my utmost gratitude to my primary supervisor, Dr. Kasturi Muthoosamy, for her continuing assistance, guidance, and inspiration throughout my journey as a PhD student. Thank you for motivating and inspiring me to grow as a research practitioner. Your selfless care, undivided support and wholesome advice for the past few years have been of invaluable importance.

I would also like to thank my co-supervisors, Prof. Sivakumar Manickam, Prof. Arben Merkoçi, and Dr. New Siu Yee, for their assistance, guidance, and patience in my research. Thank you for taking time off your busy schedule to follow up with my research progress and give me great advice, which has spurred me to understand my work better.

I am grateful to Prof. Arben for accepting me as a visiting PhD student in Nanobioelectronics and Biosensors Group, ICN2, Spain. The experience has been remarkable. I am thankful that I have been given the opportunity to meet great researchers and be part of the ICN2 family. I would like to thank Dr. Ruslan Álvarez for being my advisor, and Dr. Daniel Quesada for being a great mentor to me during my PhD journey. Your guidance and patience has helped develop me into a better researcher.

My PhD journey would have been impossible without the financial support of the Fundamental Research Grant Scheme (FRGS) scholarship from Ministry of Higher Education (MOHE), Malaysia [FRGS/1/2016/STG07/UNIM/02/1] for funding my research expenses, tuition fee and stipend for 3 years of my PhD studies. I acknowledge financial support from Department of Foundation of Engineering, University of Nottingham Malaysia for me to attend local or international conferences. I would like to thank CERCA Programme/Generalitat de Catalunya for covering my research expenses during my 1-year lab attachment in Spain. ICN2 is supported by the Severo Ochoa Centres of Excellence programme, funded by the Spanish Research Agency (AEI, Grant no. SEV-2017-0706).

A very special thanks to my family for all the sacrifices that they made for me. Thank you for supporting me for everything, and most importantly have more faith in me than I do in myself. This work is dedicated to my Dad and Mom, who have always supported and motivated me.

Finally, this work would not have been possible without the support, both mentally and physically, from my fellow friends, colleagues, and technical staffs.

Thank you all.

Declaration

The investigation presented in this thesis was conducted in the Department of Chemical and Environmental Engineering, University of Nottingham Malaysia (between Nov 2016–Dec 2017; Feb 2019–Nov 2020) and in Nanobioelectronics and Biosensors Group, ICN2, Spain (between Jan 2018–Jan 2019). Hereby, I declare that this work is purely based on my research findings and has not been submitted for any degree to any other institution.

Abbreviations

CONH	Amide
RGD	Arginine-glycine-aspartate
AFM	Atomic force microscopy
PBFI	Benzofuranisophthalate
BSA	Bovine serum albumin
BSA/AuNCs	BSA-templated gold nanoclusters
CdTe	Cadmium telluride
CVD	Chemical vapor deposition
CA	Chronoamperometry
CD	Circular dichroism
CV	Cyclic voltammetry
DNA	Deoxyribonucleic acid
DPV	Differential pulse voltammetry
K_d	Dissociation constant
EIS	Electrochemical impedance spectroscopy
λ_{ex}	Excitation wavelength
FA-rGO	FA-modified rGO
Fe^{2+}/Fe^{3+}	Ferrocyanide/ferricyanide $[Fe(CN)_6]^{3-/4-}$
FRET	Fluorescence resonance energy transfer
FR	Folate receptor
FA	Folic acid
FTIR	Fourier transform infrared spectroscopy
GL	*Ganoderma lucidum*
GSH	Glutathione
Au	Gold

$HAuCl_4$	Gold (III) chloride
AuNCs	Gold nanoclusters
AuNPs	Gold nanoparticles
GO	Graphene oxide
GO-FA	Graphene oxide-folic acid
$Ru(NH_3)_6Cl_3$	Hexaammineruthenium (III) chloride
HRTEM	High-resolution transmission electron microscope
PbS	Lead sulfide
LOD	Limit of detection
MnO_2	Manganese dioxide
MF	Membrane filter
MWCO	Molecular weight cut-off
EDC	*N*-(3-Dimethylaminopropyl)-*N*′-ethylcarbodiimide hydrochloride
NEM	*N*-ethylmaleimide
NHS	*N*-hydroxysuccinimide
NGO	Nano-GO
NPs	Nanoparticles
PBS	Phosphate buffered saline
PEG	Poly(ethylene glycol)
PVA	Poly(vinyl alcohol)
PET	Polyethylene terephthalate
K	Potassium
KCl	Potassium chloride
K^+	Potassium ion
QY	Quantum yield
E_0	Rate determination

E_S	Rate determination of RNase A/AuNCs sample
rGO	Reduced graphene oxide
RNase A	Ribonuclease A
RNase A/AuNCs	Ribonuclease A-templated gold nanoclusters
RNases	Ribonucleases
SPEs	Screen-printed electrodes
SNR	Signal-to-noise ratio
Na	Sodium
NaCl	Sodium chloride
NaOH	Sodium hydroxide
Na^+	Sodium ion
SPR	Surface plasmon resonance
E_f	Total hydrolysis
TAC	Triazacryptand
Tris-HCl	Tris-hydrochloride
Trp	Tryptophan
UV-vis	Ultraviolet-visible spectroscopy
XPS	X-ray photoelectron spectroscopy

Table of Contents

CHAPTER 1

1. Objectives

The main objective of this PhD thesis is to develop a facile and optimised protocol for the fabrication of protein-templated AuNCs for biosensing applications.

Most of the reported biomolecule and metal ion sensors involve complicated, time-consuming and costly procedures with limited effectiveness. Herein, two different fluorescent AuNCs-based nanobiosensors for the detection of glutathione (GSH) and metal ions under physiological pH conditions are presented. In addition, an electrochemical sensing platform is developed using laser scribed graphene-based electrodes for the detection of a cancer biomarker, namely FR.

This research work can be broken down into three specific objectives:

1. Integrating gold nanoclusters, folic acid and reduced graphene oxide for nanosensing of glutathione based on "turn-off" fluorescence
2. Fluorescence "turn-off/turn-on" biosensing of metal ions by gold nanoclusters, folic acid and reduced graphene oxide
3. Development of an electrochemical sensing platform for determination of folate receptor using laser scribed graphene electrodes

CHAPTER 2

2. Literature review

Nanomaterials can be broadly categorised according to their composition, such as metal, carbon, inorganic and organic nanoparticles (NPs)[1,2]. Some of the important advantages of nanomaterials are undoubtedly their small size and large functional surface area to volume ratio, in addition to interesting optical and electrical properties. These properties allow the diagnostic agents to be adsorbed, dissolved, or covalently attached to the surface, to form NP-drug/imaging/targeting complexest[3]. The complex can subsequently signal (diagnostics) to the cancer cells[4,5].

Researchers have been putting effort into designing and tailoring different nanomaterials to serve as a diagnostic platform for specific disease/cancer/illness. The main motivation of this PhD work is to design and develop protein-templated gold nanoclusters (AuNCs) as a potential biosensing nanomaterial. The following section provides an overview of the features of AuNCs, FA and graphene derivatives, together with their potential in biomedical applications.

2.1. Fluorescent gold nanoclusters as a functional nanomaterial

Metallic gold (Au) renders good chemical stability and physicochemical properties at sub-nanometre size range[6,7]. The size of gold nanoparticles (AuNPs) is in the range of 3-100 nm, which is close to the wavelength of light[8]. The collective oscillation of free conduction band electrons on the surface of AuNPs can interact with electromagnetic waves, generate localised surface plasmon resonance (SPR) effect that prompts intense light scattering and absorption at about 520 nm[9,10]. The SPR contributes to the optical and electronic properties of AuNPs.

AuNCs are groups of several to a few hundreds of Au atoms which have been widely explored since the past decade[11]. AuNCs have dimensions between those of atoms and metallic NPs[12]. The size of AuNCs is comparable to the Fermi wavelength of conduction

electrons[13–15]. Owing to the ultrasmall size (<2 nm and <150 Au atoms), although the size of AuNCs is too small to support the SPR effect[8], AuNCs exhibit strong quantum confinement effects which contribute to its strong luminescence[7]. The strong fluorescence emission of AuNCs permits quantification of nucleus targeting materials at single-particle sensitivity[16]. In other words, a single wavelength source is sufficient for simultaneous excitation of AuNCs of varying emission. In addition, AuNCs are sensitive to cluster size. Modification of the composition of NCs (adding, removing, replacing at least one Au atom) would lead to different physiochemical properties. This is known as metal engineering. These features make AuNCs a versatile and multifaceted platform for biomedical applications[17].

Ligand engineering is another strategy to design AuNCs with desirable features[18]. Atomically precise AuNCs are endowed with rich coordination chemistry owing to the presence of ligands[6]. Examples of ligands are polymers, peptides, dendrimers, micelles, thiolates and biomolecules[19]. Thiolate ligands are often selected as the protecting agent for the Au core in AuNCs, as well as the stabiliser and passivating agent. This is due to the strong bonding between Au atoms and sulfur in thiolate ligands. Ligands maintain the atomic precision, well-defined molecular structure and intriguing molecular-like properties of metal NCs[6]. Therefore, ligands influence the synthesis (size, formation rate, *etc*.), physicochemical properties (geometrical structure, stability, solubility, biological properties, *etc*.) and catalytic applications (selectivity, activity, *etc*.) of AuNCs.

Biomolecules, such as proteins or deoxyribonucleic acid (DNA), are intensively used in synthesising AuNCs. Examples of proteins used are bovine serum albumin (BSA), insulin, globulins and pepsin[19]. Proteins act as a template, protecting agent and stabiliser for the formation of AuNCs[19]. Protein-templated AuNCs have gained immense attention in biomedical applications owing to the tunable amino acids, rich functional chemistry, good biocompatibility, high quantum yield (QY) in the near-infrared window, improved

physicochemical and physiological properties[18–20]. These features allow AuNCs to become multifunctional and suitable to be used as biosensing and bioimaging probes (for diagnosis).

2.2. Bovine serum albumin as a protein template

BSA is a small and dynamic globular albumin protein with a molecular weight of 66.5 kDa[6]. BSA is a single polypeptide chain with 583 amino acid residues. The secondary structure of BSA contains a high percentage (50-60 %) of α-helix[6]. It has no carbohydrates. At pH 5-7, BSA contains 17 intra-chain disulfide bridges and 1 sulfhydryl group. BSA is autofluorescent in the blue region, with the ability to affiliate five different conformations reversibly in the pH range from 2.51 to 10.21[21]. The hydrodynamic diameter of native BSA is 7.4 nm at pH 7. The isoelectric point of BSA is at pH 4.7[22]. BSA is a commonly used drug delivery nanocarrier[23], owing to its non-immunogenicity, biodegradability and water solubility[24]. BSA may attach to the O/W interface, bind, entrap or coat bioactive molecules to form complexes with medical importance[23].

BSA is the first protein that has been used as a template for synthesising protein-templated AuNCs[25], where it imparts bioactivity to the AuNCs. BSA-templated AuNCs (BSA/AuNCs) are stabilised by a combination of Au-S bond with 35 cysteine residues and steric protection from the bulkiness of a BSA[6]. BSA/AuNCs present the advantages of high chemical stability, simple synthesis, reproducibility, photoluminescent and biological selectivity[6]. Therefore, BSA/AuNCs have great potential both in *in vitro* and *in vivo* biological applications.

2.3. Bovine pancreatic ribonuclease A as a protein template

Ribonucleases (RNases) play an important role in immune response regulation during infection and cancer[26]. Particularly, RNase A is the first and best characterised enzyme in the RNase family since the early 20th century. RNase A is an endonuclease that catalyses the depolymerisation of RNA. RNase A recognises and cleaves the negatively

charged phosphate groups (pyrimidine bases) at the 3`-end of the phosphodiester bond for binding with the purine bases at the 5`-end position[27]. As shown in Figure 1.1, RNase A is composed of three α-helices and seven β-strands arranged in two "lobes", with a globular configuration of 2.2 nm x 2.8 nm x 3.2 nm[28].

With a molecular mass of 13.7 kDa and a sequence length of 124 amino acids with no carbohydrate attached to it, RNase A displays outstanding thermal stability (can sustain 100 °C without aggregation), anticancer and antimicrobial properties, and has been used as chemotherapeutics in clinical trials[26,29]. RNase A may bind to the negatively charged cell membrane, enter cells by endocytosis, translocate to the cytosol and evade mammalian protein ribonuclease inhibitor for RNA degradation[30]. Dysregulation of RNase A activity or expression level is closely related to pancreatic, ovarian, bladder and thyroid cancer[31].

Kong *et al.* reported the use of RNase A as a biological template in synthesising cadmium telluride (CdTe) quantum dots[28], AuNCs[10] and lead sulfide (PbS) quantum dots[29], respectively in 2010, 2013 and 2016. In terms of synthesis of ribonuclease A-templated AuNCs (RNase A/AuNCs), it is speculated that Au ions interact with the functional groups (amino groups) of RNase A, forming Au-S bonds[32]. These RNase A-assisted synthesised nanomaterials have shown potential in targeted drug delivery, cancer imaging and therapy after functionalisation with targeting and imaging agents such as cyclic arginine-glycine-aspartate (RGD) peptides[28] and vitamin B_{12}[10]. Interestingly, the group has recently reported the engineering of corona structure of RNase A on the AuNCs surfaces to obtain red-shifts of emission at 1050 nm in NIR-II region for enhanced gastrointestinal tract imaging[33].

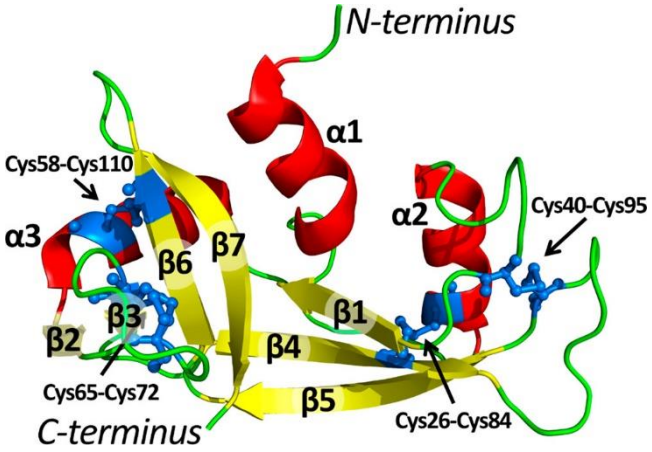

Figure 1.1 Cartoon representation of RNase A structure. Cysteine residues involved in disulfide bonds are represented by blue sticks and balls; α-helices and β-strands are indicated with symbols α and β, respectively. Reprinted with permission from ref.[34].

2.4. Folic acid for active targeting of cancer

Active targeting can potentially reduce the diagnostic time besides accelerating cancer therapy. FA is a water-soluble vitamin B_9 which is widely used in drug targeting owing to its low-cost, compatible in both organic and aqueous solvents and lack immunogenicity[35]. Folate receptor (FR) is highly expressed (more than 90%) on primary and metastatic human cancer cells[36]. FAs have a high affinity for FRs on cancer cells. Hence, FAs are commonly used as colon cancer biomarkers for precise targeting of pathologic cells, specifically without affecting the normal cells[37,38]. FAs are also found to inhibit COLO-205 colon cancer growth through anti-cancer cell proliferation and anti-angiogenesis[39].

FRs are considered as receptors for mediating selective targeting of drugs/imaging agents to cancer cells[40,41]. It can be easily conjugated to both therapeutic and diagnostic agents, acting as an ideal targeted therapeutic biomolecule[42]. Once the folate conjugate binds to FRs and subsequently internalised into endosomes, the changes in pH of the endosome (approaches pH 5) will stimulate the dissociation of FAs from the receptors, releasing the therapeutic compounds directly to cancerous sites[43], as shown in Figure

1.2. Therefore, RNase A coupled with AuNCs and FA can be employed for simultaneous targeting, imaging as well as therapy at cancer and its metastasis sites.

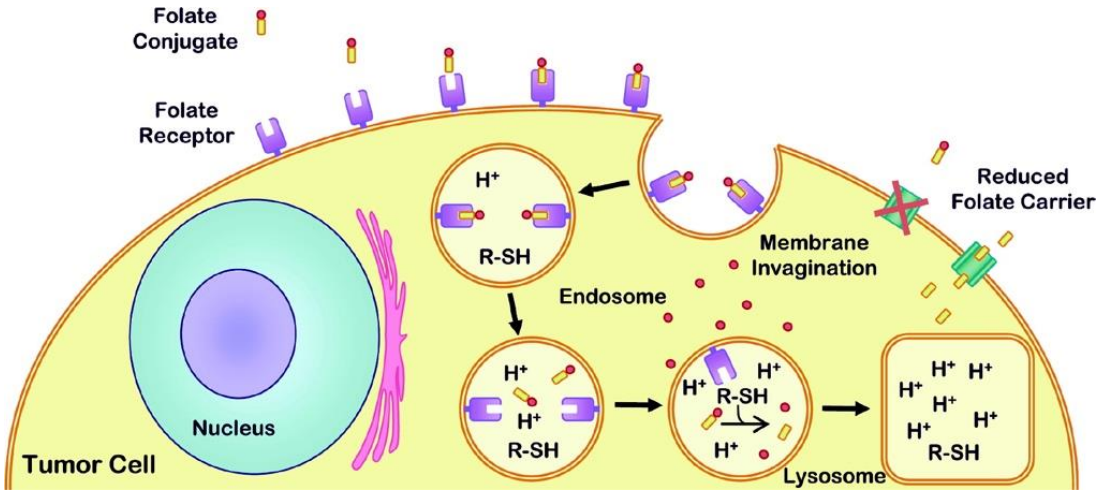

Figure 1.2 FR-mediated endocytosis of a FA drug conjugate. Folate conjugates bind to FR with high affinity and subsequently internalised into endosomes. The disulfide bonds are reduced upon internalisation. A folate-disulfide-drug conjugate is then released from the FR, and the prodrug is reduced to release the parent drug cargo. FR is a receptor for mediating selective targeting of drug/imaging agents to cancer cells. Reprinted with permission from ref.[42].

2.5. Graphene oxide and reduced graphene oxide

Graphene and its derivatives have become the spotlight of nanotheranostics since the past decade, owing to their electrically tunable surface chemistry and mechanical robustness[44–47]. The sp^2-hybridised carbon atoms in a honeycomb network provide graphene with a large surface area, enabling the compounds to adsorb/functionalise on both sides of its planar surface.

Graphene oxide (GO) is a flake-like material made up of a single atomic layer of carbon[48], functionalised with different oxygen based functional groups such as epoxy and hydroxyl groups. There are currently no internationally recognised standards for thickness of GO.

The theoretical thickness of a single GO sheet is estimated to be in the range from 0.5 to 2 nm[49].

Atomic force microscopy (AFM) in tapping mode is commonly used to measure the lateral dimensions and thickness of single and few layers graphene on mica surfaces. Different works suggested different thickness of GO. For example, AFM image analysis from Tang *et al*. (2018)[50], Stankovich *et al*. (2007)[51] and Ding *et al*. (2011)[49] each proposed that the thickness of a single well-exfoliated GO sheet was around 0.6 nm, 1 nm and 1.5 nm, respectively. The discrepancy of the AFM values and the theoretical value can be attributed to the folds and bumps occurring at the surface of GO. Besides, the types of substrate used, interactions of the cantilever with the substrate and the GO nanosheets, tip-surface interactions, image feedback settings, surface chemistry, contaminants and instrument noise[52] are some of the contributing factors for the thickness variation of GO. The presence of functional groups in GO contributes to its high hydrophilicity and solubility in different solvents. Advantages of GO include facile synthesis, adjustable moderate conductivity, high surface area, excellent biocompatibility, high mechanical strength and thermal stability, and low-cost[53]. Moreover, the large molecular weight of GO enhances the imaging contrast[54], while its electrical properties allow long-range fluorescence resonance energy transfer (FRET)[55]. Due to the presence of three different functional groups (C–O, C=O and O=C–OH), both GO and reduced graphene oxide (rGO) can absorb NIR, visible and UV light and fluoresce at a particular wavelength, highlighting its potential as a photothermal agent[56–63].

Functional GO has been proven to be a viable carrier of drugs, imaging and therapeutic agents owing to its high loading capacity, strong adsorption capacity for serum proteins, small size, intrinsic optical properties and large surface area[56,64,65]. Functional GO has two aromatic planes and is capable of adsorbing aromatic compounds *via* simple physisorption (mainly π-π stacking and hydrophobic interactions)[64]. To our knowledge,

many studies have been carried out in loading cancer drugs, such as doxorubicin and camptothecin, onto GO functionalised with targeting agents for theranostics of cancer cells[64,65].

2.6. Principles and theory of fluorescence spectroscopy

Fluorescence is a type of radiative emission[66]. As illustrated in Jablonski diagram Figure 1.3, fluorescence occurs when a molecule (also known as fluorophore) at the ground state absorbs excitation energy at a wavelength which promotes photons to an excited singlet state. The molecule will subsequently decay to the lowest vibrational energy level, relax back to the ground state while emitting photons during the process. The emission can be characterised by QY and fluorescence lifetime[66]. The most common fluorophores are organic dye molecules, usually characterised by aromatic rings or conjugated carbon chains[67].

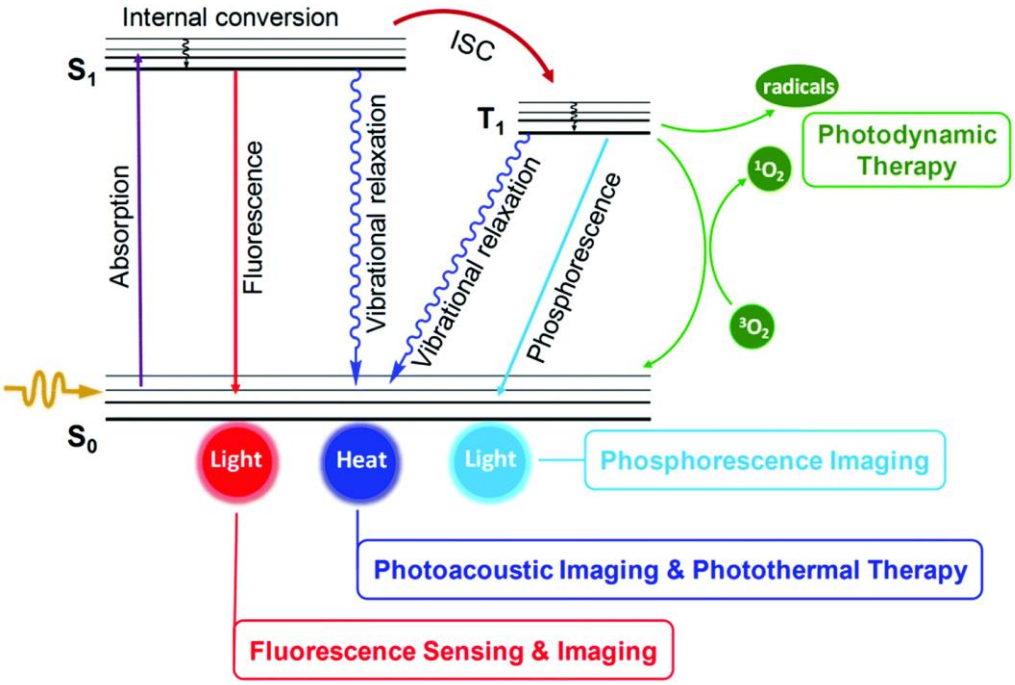

Figure 1.3 Schematic of a Jablonski diagram showing different energy transition processes and the subsequent potential in phototheranostics. Reprinted with permission from ref.[66].

Fluorescence quenching can be defined as the decrease of the QY of fluorescence from a fluorophore induced by a variety of molecular interactions with quencher molecule[68]. Fluorescence quenching is one of the ultra-high sensitive tools for the determination of the interaction of different molecules and proteins. For example, several fluorescent AuNCs-based platforms have been developed in the field of biosensing for biomarkers such as small molecules, DNA and proteins[69–72]. The fluorescence of AuNCs is affected by the charge transfer from the ligands to the Au core through Au-S bonds. Fluorescence intensity is also influenced by the direct donation of delocalised electrons of electron-rich atoms or groups of the ligands to the Au core.

Fluorescence quenching-based "turn-on" assay is widely applied in biosensing. In brief, the fluorescence of the donor can be effectively quenched by the acceptor in the absence of targets and restored upon the addition of targets. The restored fluorescence intensity is proportional to the concentration of targets. However, this method generally has limited detection sensitivity due to photobleaching of organic dyes, high auto-fluorescence background and inner filter effect caused by absorbing species[73]. Water-soluble GO is an efficient quencher and may lead to a low background and results in high sensitivity.

2.7. An overview of glutathione and its detection

GSH is a low molecular weight (307.32 $g.mol^{-1}$) tri-peptide composed of glutamate, cysteine and glycine[74–76]. As an endogenous antioxidant, GSH may scavenge reactive oxygen species, protect cells from oxidative stress and subsequently inhibit cancer progression[74,75,77–80]. GSH levels are found to be elevated in illness/cancers such as Alzheimer's disease[81] as well as ovarian[82], liver[76], lung, colorectal, breast, head and neck cancer patients[83]. Reducing intracellular GSH levels has been proposed as one of the strategies of cancer treatment[84,85]. Hence, sensing of GSH in the biological samples for diagnosis of diseases is of great interest in biomedical applications.

Although commercial kits for the detection of GSH are available, there is still a need for a detection platform with the advantages of lower cost, fast response time, more sensitivity and essentially stable[86]. The use of nanomaterials in biosensing is becoming popular in recent years due to improvements in its sensitivity and robustness[87–90]. Contrary to enzymes and other biological compounds, nanomaterials are stable in time and do not require, in most cases, special storage conditions (*i.e.* low temperature, buffered medium, *etc.*).

In the recent decade, polydopamine NPs[91], iron pyrite NPs[92], carbon dots[93] and mixed-valence-state cobalt nanomaterials[94] have been designed for GSH sensing. Particularly, manganese dioxide (MnO_2) nanosheets are usually selected as GSH biosensors, owing to their excellent colloidal stability, absorption capability, redox chemistry and biocompatibility[95–97]. However, toxicity studies of MnO_2 nanosheets in the biological environment are still in the preliminary stage[98,99]. Although previous reports on GSH sensing using fluorescence methods were claimed as cost-effective and highly sensitive, however, those methods involve complicated experimental procedures and are time-consuming[100–102].

Generally, GSH is found in the cytosol of cells where its concentration is in the range of 1-10 mM[103]. Despite with picomolar-level detection capacity, most of the current nanomaterial-based GSH biosensors (Table 1) present several drawbacks for wider biological applications, such as its potential toxicity and immunogenicity, reproducibility of the synthesised nanomaterials, *etc.*[104]. For example, quaraine dye, an organic fluorophore with advantages of lower photodamage, deeper tissue penetration and minimal fluorescence background, has been used for bioimaging and selective detection of GSH[105]. However, the dye is chemically fragile and prone to form non-fluorescent aggregates in biological media. Therefore, it is desirable to fabricate a GSH biosensor which is biocompatible and can detect at least milli-molar concentrations of GSH[106].

Table 1 Examples of GSH biosensors with their sensitivity and linear range values as reported in the literature.

Schematic Biosensor Assembly	Signal	Linear Range	Limit of Detection	Reference
2D MnO_2 nanosheets-BSA/AuNCs	Fluorescence	0-2 mM	20 μM	[78]
MnO_2-induced synthesis of polydopamine NPs	Fluorescence	0-800 μM	1.5 μM	[91]
Bis-squaraine dye SQSS	Fluorescence	0-10 μM	0.15 μM	[105]
Carbon NPs@MnO_2–AgNP nanocomposite	Fluorescence	0.8-80 μM	0.55 μM	[107]
Mesoporous silica nanoquenchers capped with anti-GSH antibody	Fluorescence	0-10 mM	52 pM	[106]
Carbon dot–MnO_2 nanosheet	Fluorescence	0.2-600 μM	22 nM	[108]
AuNCs−Hg(II) system	Fluorescence	0.04-16.0 μM	7.0 nM	[109]
MoS_2 quantum dot donor and Rhodamine 6G dye acceptor	Fluorescence	5-50 nM	2.7 nM	[110]
Self-quenched BSA/AuNCs	Fluorescence	0.1-1.5 mM	0.004 mM	[111]
BSA/AuNCs-MnO_2 nanocomposite	Fluorescence	2-200 μM	2.2 μM	[112]
RGD-modified BSA/AuNCs	Fluorescence	1-10 mM	-	[113]
Lucigenin-MnO_2 nanosheets	Fluorescence	1-150 μM	180 nM	[97]

Poly (allylamine) hydrochloride-confined BSA/AuNCs	Fluorescence	0.3-20 mM	3 mM	[114]
Mixed-valence-state cobalt nanomaterials	Colorimetric	0.5-40 μM	0.03 μM	[94]
FA-rGO-BSA/AuNCs	Fluorescence	0-1.75 μM	0.1 μM	Present work

2.8. An overview of metal ions detection in a biological fluid

Many studies have found a correlation between metal ions and biological processes such as kidney function, muscle contraction, regulation of blood pressure, nerve transmission, autophagy, apoptosis, *etc.*[115–117]. Metal ions detection in a biological fluid is a challenging task due to the obvious interference or competitive binding nature of other alkaline metals ions[118]. This restricts the sensor with limited selectivity against other alkali ions, especially in aqueous solutions[116]. Common analytical techniques employed for metal ions detection are electrochemical, fluorescence and colorimetric methods. Electrochemical methods, such as the potassium ion (K^+) electrode, give reliable data with low detection limits (as low as 2.3 nM)[119]. However, it is limited to non-invasive study in biological systems due to the complicated nature of real sample matrices. The electrochemical method is only suitable for large volumes (higher than few to tens of pico-litres) with large cell numbers. In contrast, the fluorescence method stands out as it is convenient, non-invasive, disposable, can be miniaturised and allows real-time *in situ* response[119,120]. "Turn-off" fluorescence assay is usually less sensitive than "turn-on" assay[121].

Oligonucleotide aptamers[116,122], single-layer graphene[117], valinomycin[123], 18-Crown-6 ether[124], *etc*. are some of the sensing elements used for selective and sensitive detection of K^+. Graphene-based devices can detect K^+ concentrations as low as 1 nM or even 2

pM[119]. Triazacryptand (TAC) is typically used in designing biosensor for K^+, owing to its ability as a K^+ binding ligand and selective response for K^+ over competing for sodium ion (Na^+)[115,125]. Recently, a fluorescent K^+ sensor composed of TAC and rhodamine analog (as the fluorophore) has been used for monitoring the regulation of K^+ in mitochondria during apoptosis[115]. The as-synthesised sensor exhibited the largest Stokes shifts (120 nm) and the longest emission peak wavelength (720 nm). Photo-induced intramolecular electron transfer from TAC to the rhodamine analog quenched the fluorescence. In contrast, the fluorescence is recovered upon the addition of K^+ as electron transfer will be inhibited during complexation between TAC and K^+. However, these small molecule-based sensors are significantly taken up by many cell types, and thus, their application in extracellular K^+ sensing is limited[120]. Photo-induced intramolecular electron transfer approach can be complex and difficult to optimise[126]. Also, these sensors were not reported for either intracellular or extracellular investigations. An ideal intracellular K^+ sensor should display wide dynamic K^+ detection range (100-300 mM), insensitive to Na^+ (5-15 mM in intracellular fluid) and other metal ions at physiological concentrations, insensitive to pH and give rapid response[115].

Na^+-specific DNAzyme[127,128], fluorescent organic NPs from a Biginelli-based receptor[118], *etc*. have been used in measuring Na^+ concentration in the physiological range. Supramolecular receptors based on crown ethers or cryptands have been developed with varying structural modifications to render them as strong contenders for sensing Na^+ in biomedical applications. Nevertheless, the efficiency of Na^+ sensor in aqueous media, complicated procedures, requisite for expensive setup and instrumentations, are some of the shortcomings of the developed sensors. Also, the formation of highly stable complexes from crown ethers with sodium (Na)/potassium (K) salts limits the usage and sensitivity of the sensors[129].

Despite the excellent sensitivity and selectivity, most of the current nanomaterial-based Na^+ and K^+ biosensors (Table 2) present several drawbacks for wider biological applications, such as lengthy experimental procedures, requisite for expensive instrumental setups, results are easily affected by photobleaching and light scattering, materials with limited toxicity studies, *etc*. For example, commercially available K^+ biosensor, such as K-binding benzofuranisophthalate (PBFI), has a relatively large dissociation constant (K_d) (up to 6.6 mM)[130], which is not ideal for highly concentrated intracellular K^+ sensing. Therefore, it is desirable to fabricate Na^+ and K^+ biosensors which can be constructed in a facile protocol, cost-effective, biocompatible, capability to measure quickly, the fluorescence emission wavelength of over 600 nm and do not require a reference solution.

Table 2 Examples of K^+ and Na^+ biosensors with their sensitivity and linear range values as reported in the literature.

Type of metal ion biosensor	Schematic biosensor assembly	Signal	Linear range	Limit of detection	Reference
Potassium ion	CVD-grown single-layer graphene	Electrical	1 nM-10 μM	1 nM	[117]
	AuNPs and a dye (Cationic Yellow 5GL)	Colorimetric	10 nM-50 mM	4.4 nM	[131]
	Berberine–G-quadruplex complex	Fluorescence	0.005-1.0 mM	2 μM	[121]

	TAC with a rhodamine analog		16-400 mM	-	[115]
	Dye OliGreen and ATP-binding aptamer		100-1000 nM	75 nM	[116]
	Aminated carbon dots and 18C6E-rGO hybrids		0.05-10.0 mM	10 μM	[132]
	2-dicyanomethylene-3-cyano-4,5,5-trimethyl-2,5-dihydrofuran (TCF) and TAC		0-1600 mM	-	[125]
	TAC with polymers (HEMA, AM, METAC, MESA)		0-200 mM	-	[120]
	RNase A/AuNCs		0-200 mM	74 mM	Present work
	FA-rGO-RNase A/AuNCs		0-25 mM	15.7 mM	Present work
	Solution-gated CVD graphene with hydrophilisation pretreatment	Electro chemical	0.1 pM-100 nM	0.058 pM	[119]

	Ordered mesoporous carbon sphere		$10^{-4.19}$-$10^{-0.21}$ M	5.4 μM	[133]
	Manganese oxide nanorods		2-90 μM	0.05 μM	[134]
	4-aminobenzo-18-crown-6 on a functionalised Au surface		0.1-7 mM	-	[124]
	Valinomycin doped chitosan-GO thin film	Surface plasmon resonance	0-100 ppm	0.001 ppm/ 0.02557 μM	[123]
	Silver nanoplasmon	Surface-enhanced Raman scattering	50-3000 nM	25 nM	[135]
Sodium ion	G-quadruplex formed by p25	Colorimetric	20 μM-0.8 mM	0.6 μM	[128]
	Covalently linked aminorhodamine B-calix[4]arene chromoionophore	Fluorescence	0.01-2.0 M	-	[126]
	Organic NPs (Biginelli compound 1)		0-40 μM	22 nM	[118]
	RNase A/AuNCs)		0-100 mM	49 mM	Present work

	FA-rGO-RNase A/AuNCs)		0-200 mM	110 mM	Present work
	Silver NPs/GO nanocomposite	Electro chemical	0-100 mM	9.344 mM	[136]

CHAPTER 3

3. Integrating gold nanoclusters, folic acid and reduced graphene oxide for nanosensing of glutathione based on "turn-off" fluorescence

3.1. Introduction

Sensing of FA based on the fluorescence quenching of BSA/AuNCs has been introduced by Hemmateenejad *et al.* (2014)[137]. It is speculated that FA interacts *via* hydrophilic and hydrophobic interactions with tryptophan (Trp) residues (Trp-132 on the surface and Trp-212 residue inside) of BSA. The interaction of FA and BSA alters BSA protein secondary structure, causing a partial protein unfolding and therefore results in fluorescence quenching[68]. Although the sensor previously reported can be applied in the determination of FA in pharmaceutical preparations, its application as a delivery carrier remains unexplored till date.

Conjugation of FA on graphene oxide-based nanosystem can target and induce higher cytotoxicity on FR-positive cells such as breast, ovarian, lung and colon cancers[138–140]. FA plays a dual role (as a reductant and stabiliser) in FA-modified rGO (FA-rGO). The covalent binding of FA to rGO can produce stable and biocompatible materials[141], enhance the energy accepting efficiency in long-range resonance energy transfer process than graphene[142], thereby making it suitable to be employed as a biosensor or drug delivery carrier. Therefore, conjugation of FA to rGO serves as a potential nanocarrier for controlled loading and targeted delivery of therapeutic agents[64,143].

Despite its remarkable promise, no reports have been devoted to the construction of a fluorescent sensing platform with FA-rGO and BSA/AuNCs. The effect of GSH on the FA-rGO-BSA/AuNCs has also remained largely unexplored. Few reports propose the use of BSA/AuNCs-Cu system for GSH sensing[60,61], in which Cu^{2+} is used as a fluorescence quencher for BSA/AuNCs, and the fluorescence can be recovered with the addition of GSH. However, this is the first work carried out in exploring the potential of FA-rGO not only as a carrier of BSA/AuNCs but also having the potential as a GSH nanobiosensor with significantly improved sensitivity and selectivity. The elucidation of such mechanism will enable us to design effective fluorescent sensors for targets of interest rationally. In

this investigation, we aim at understanding the quenching mechanism of FA-rGO towards BSA/AuNCs fluorescence, which in turn allows us to design effective "turn-off" fluorescent nanosensors for GSH detection. This is the first time that BSA/AuNCs, FA and rGO are combined for fluorescent sensing of GSH, with a simple experimental process that requires short incubation time of only 2 min.

3.2. Experimental

3.2.1. Reagents and materials

BSA (96 %, Sigma) was purchased in lyophilised-powder form and used without further purification. Gold (III) chloride ($HAuCl_4$) solution, FA (>97 %), reduced *L*-GSH (≥98 %), *N*-hydroxysuccinimide (NHS), *N*-(3-Dimethylaminopropyl)-*N'*-ethylcarbodiimide hydrochloride (EDC), and all other reagents were purchased from Sigma Aldrich and used as received. Ultrapure deionised water was obtained from a Milli-Q Plus system (EMD Millipore, Billerica, MA, USA). Sodium hydroxide (1 M, NaOH) was purchased from Nacalai Tesque. *L*-ascorbic acid was purchased from R&M Chemicals.

3.2.2. Analytical measurements

Fluorescence spectra were recorded using a fluorescence spectrophotometer (Hitachi F-7000). Ultraviolet-visible (UV-vis) absorbance was measured using UV-vis spectrophotometer (Lambda 35, Perkin Elmer) to ensure the absence of large NPs, which commonly show absorption at about 520 nm. UV light with the excitation of 365 nm was used. To study the protein conformation, far-UV circular dichroism (CD, J-1000 series, JASCO) was employed. The oxidation state of core Au atoms was examined by X-ray photoelectron spectroscopy (XPS, ULVAC-PHI, Inc.). The morphological characterisation of BSA/AuNCs was carried out using a high-resolution transmission electron microscope (HRTEM, FEI Tecnai G^2 F20 X-Twin). The Fourier transform infrared spectroscopy (FTIR) spectra of FA, rGO and FA-rGO were recorded on an FTIR spectrometer (PerkinElmer Frontier).

3.2.3. Synthesis of BSA/AuNCs

BSA/AuNCs were synthesised following a modified protocol of Xie *et al.* (2009)[25]. Briefly, 0.7 mL of 12 mM $HAuCl_4$ solution was added to the same amount of aqueous solution containing 20 $mg.mL^{-1}$ BSA in a thermomixer and mixed at 1200 rpm for 5 min at 40 °C. Then, 0.1 mL of 1 M NaOH solution was introduced, and the mixture was mixed in the thermomixer at 900 rpm for 6 h at 60 °C. The colour of the solution changed from light yellow to deep brown, which indicates the successful synthesis of BSA/AuNCs. The resulting solution was purified using EMD Millipore Amicon Ultra-0.5 centrifugal filter units with a membrane molecular weight cut-off (MWCO) of 10 kDa were used to remove residual ions (*i.e*. Na^+, Au^{3+} and OH^-). The products were then stored at 4 °C until further use.

3.2.4. Preparation of rGO

GO, *Ganoderma lucidum* (GL) extract and rGO were synthesised following a protocol reported by our group[144]. Briefly, GO solution (0.1 $mg.mL^{-1}$) was adjusted to pH 7 using NaOH. GL extract (50 mL) was added to a 50 mL of GO solution and transferred to a water bath which was preheated to 85°C. The solution was mixed at 120 rpm for 16 h. The resulting solution was ultracentrifuged at 10,000 rpm for 20 min and washed three times with water before re-dispersing in water.

3.2.5. Covalent conjugation of FA-rGO

FA-rGO was prepared using a modified protocol reported by Zhang *et al.* (2010)[64]. Briefly, 1 $mg.mL^{-1}$ rGO was subjected to probe sonication of 20 kHz, at 500 W for 10 min. NaOH (6.25 mmol) and chloroacetic acid (0.250 g, 11.655 mmol) was then added. The mixture was bath sonicated (40 kHz, 70 W) for 2 h. After neutralisation with HCl, the mixture was purified by repeated rinsing and centrifugation until rGO is well dispersed in deionised water. The mixture was dialysed against deionised water for 24 h. To introduce sulfonate groups to the rGO, sulfanilic acid (51.96 mg, 0.06 M) and sodium nitrite

(70.720 mg, 0.205 M) were dissolved in 20 mL of 0.25 v/v % 1 M NaOH. The solution was added dropwise to 0.1 M HCl in an ice bath. The sulfonated groups were mixed with rGO in an ice bath under stirring for 2 h, followed by dialysis against deionised water for over 24 h. The mixture was stored at 4 °C until further use. EDC and NHS were added onto rGO, with the molar ratio of rGO:EDC:NHS as 40:50:73. The mixture was subjected to probe sonication for 2 h. FA (5 $mg.mL^{-1}$, dissolved in 0.5 M $NaHCO_3$, at pH 8) was added and stirred overnight. The products were dialysed against 0.5 M $NaHCO_3$ for 24 h, followed by dialysis against deionised water for over 24 h. The products were characterised by FTIR, UV-vis spectroscopy and fluorescence spectrophotometer.

3.2.6. Fluorescence quenching of BSA/AuNCs by FA-rGO

To investigate the potential of FA-rGO to induce fluorescence quenching of BSA/AuNCs, different concentrations of FA-rGO were added to 3 $mg.mL^{-1}$ of BSA/AuNCs. The solution was mixed in a thermomixer at 1200 rpm for 5 min at room temperature. Fluorescence intensity of the solution was recorded with an excitation wavelength (λ_{ex}) of 365 nm.

3.2.7. Sensing of GSH

GSH detection was conducted as follows. The same volume of FA-rGO-BSA/AuNCs was added with various concentrations of GSH. The solution was mixed in a thermomixer at 1200 rpm for 2 min at room temperature. The fluorescence intensity was measured to quantify the concentration of GSH at λ_{ex}= 365 nm.

3.2.8. Calculation of the signal-to-noise ratio and limit of detection

Signal-to-noise ratio (SNR) was calculated using the following standard equation (3.1).

$$SNR = R_L / S_1 \quad (3.1)$$

Limit of detection (LOD) was calculated according to the following standard equations (3.2) and (3.3).

$$y = a + SX \quad (3.2)$$

Here, X is LOD.

$$y = (K \times S_1) + Blank \quad (3.3)$$

Wherein,

$$a + (S \times LOD) = (K \times S_1) + Blank$$

Therefore,

$$LOD = [(K \times S_1) + Blank - a]/S$$

where R_L is the signal response of least known concentration, K is the coefficient 3.3[145], *S* is the slope obtained from a calibration curve, while S_1 is the statistical result of the standard deviation of the blank solution and a is the blank value.

3.3. Results and Discussion

3.3.1. Synthesis and characterisation of BSA/AuNCs

Different fabrication methods of protein-templated AuNCs have been proposed since the year 2009; however, the long reaction time (up to 12 h), low QY (about 6 %) and complicated protocols are some of the existing limitations. In this work, a simple protocol for the fabrication of BSA/AuNCs with several advantages has been reported. The advantages of this protocol are shorter synthesis time (only 6 h), higher QY (10.62 %), need for lower protein amount (only 20 $mg.mL^{-1}$); and employ mild reaction conditions. The protocol is also applicable for the fabrication of AuNCs with different protein templates such as lysozyme or ribonuclease A (RNase A, as tested, data shown in Chapter 4), and not limited to BSA alone. Overall, such a synthesis protocol is more economical and eco-friendly.

HRTEM image (Figure 3.1a and Supplementary Figure S3.1) demonstrated that the sizes of the BSA/AuNCs fall within a narrow range of less than 2 nm. BSA/AuNCs are generally spherical dots demonstrating uniform size with high mono-dispersity. As shown in the optical absorption of the as-prepared BSA/AuNCs (Figure 3.1b), no apparent SPR absorption peak could be observed in the range between 400 and 600 nm[13]. The absorption of BSA/AuNCs monotonously increases towards the shorter wavelength over

the range of 220-850 nm. The absence of the plasmon absorption at about 520 nm indicates that the ultra-small size of AuNCs can no longer support LSPR[10]. These confirm the encapsulation of AuNCs in BSA protein, and most importantly, no large NPs (>2 nm in diameter) were formed[146].

AuNCs display optical confinement and photocatalytic properties[13]. As shown in Figure 3.1b), the as-synthesised BSA/AuNCs exhibited bright red fluorescence under UV irradiation, with the emission band at 630 nm when excited at 365 nm[25]. The red emission from BSA/AuNCs was attributed to the Au clusters. The AuNCs bind to hydrophobic pockets on the BSA protein's surface and trap the AuNCs close to cysteine residues for subsequent chemical interactions[14]. The photoluminescence QY was about 10.62 % when calibrated with rhodamine B, which demonstrates a QY value of 31 % in water when excited at 514 nm. The obtained QY is higher than the previously reported value of around 6 %[25]. The earlier study has shown that BSA starts to unfold at 65 °C[147]; therefore, a temperature of 60 °C was chosen for the synthesis, instead of the physiological temperature (37 °C). This is because, upon heating, the compact native form of BSA becomes more flexible and reactive, exposing the Tyr and Trp residues from the hydrophobic core of BSA molecule to a more polar solvent environment[147,148]. A higher interaction between BSA and Au ions fastens the formation of BSA/AuNCs.

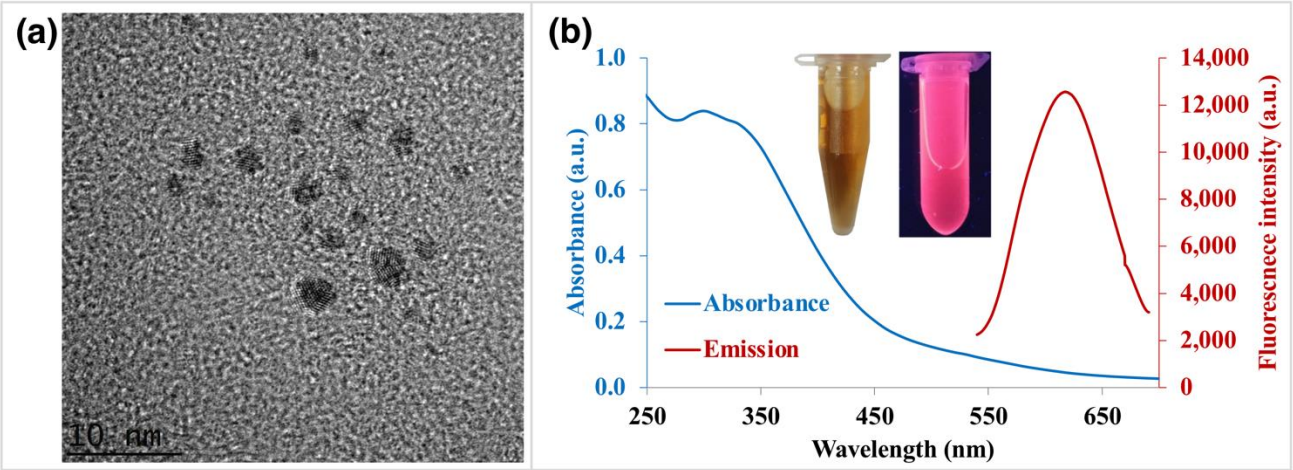

Figure 3.1 Characterisation of BSA/AuNCs. (a) HRTEM image of the diluted fluorescent BSA/AuNCs. (b) UV-vis absorption (blue line) and fluorescence emission spectra (red line) of the as-prepared BSA/AuNCs with λ_{ex} at 365 nm. Inset: Optical photographs of the BSA/AuNCs under visible (left) and UV light (right).

XPS has been employed to investigate the protein-AuNCs interactions and to prove the reducibility of the protein against Au(III) ions in alkaline pH (Figure 3.2). As shown in Figure 3.3a, the Au 4f of XPS and the binding energies at 83.628 eV (Au $4f_{7/2}$) and 86.628 eV (Au $4f_{5/2}$) confirm the formation of stable BSA/AuNCs, with most of the Au atoms close to the oxidation state of Au(0). The two S 2p bands with the binding energies of about 163 (S $2p_{1/2}$) and 168 eV (S $2p_{3/2}$) were observed (Figure 3.3b), corresponding to the gold-bound (Au-S) and oxidised sulfur species, respectively. Their relevant abundances were estimated as 48.5 and 51.5 %, respectively, from the XPS curve fit of BSA/AuNCs.

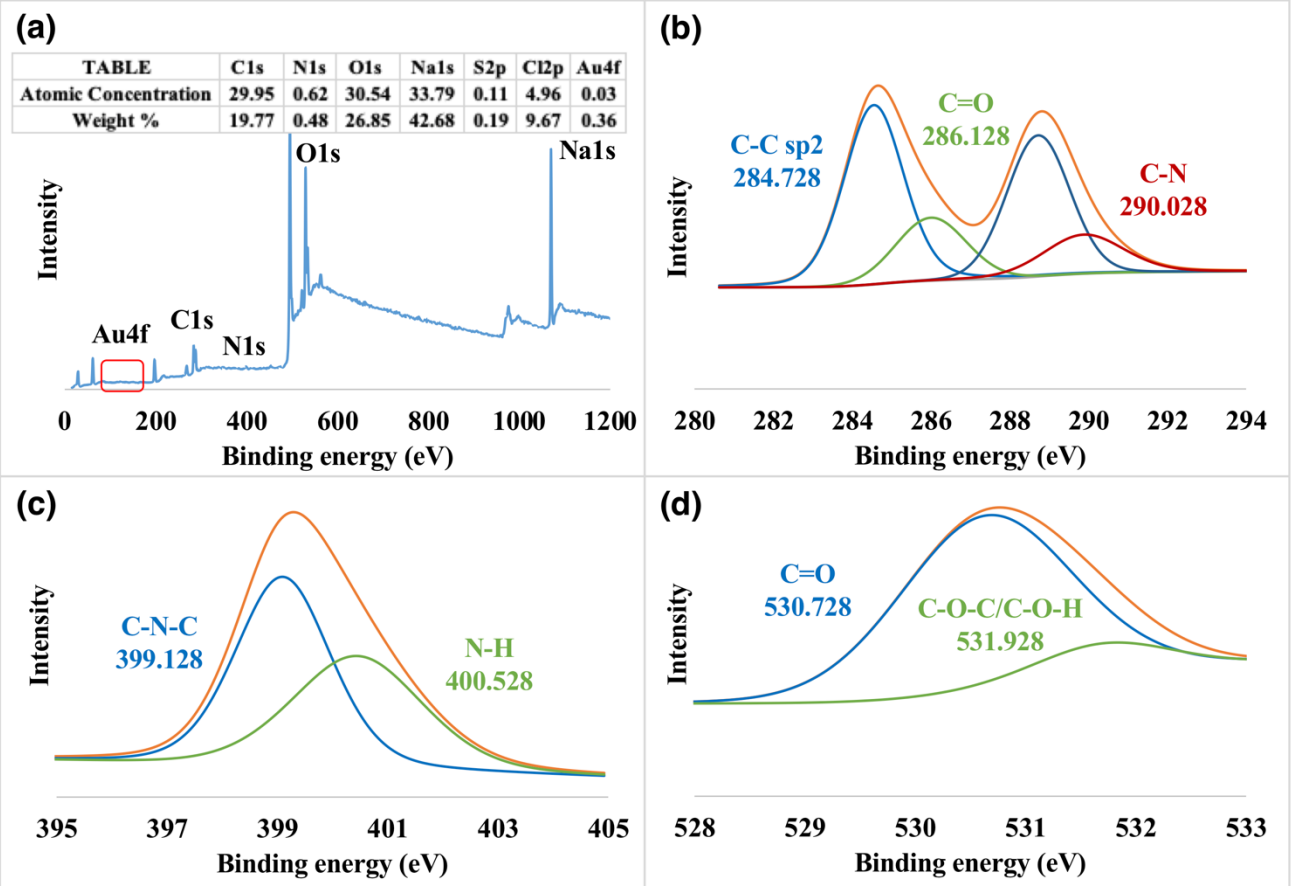

Figure 3.2 Representative XPS spectra of (a) full range, (b) C 1s, (c) N 1s and (d) O 1s of BSA/AuNCs.

CD spectroscopy was employed further to investigate the conformational evolution of native and AuNCs-bound proteins. From the CD spectra of BSA/AuNCs (Figure 3.3c), the characteristics of the two negative bands of the typical α-helix at 208 and 220 nm were observed. This corresponds to π to π* and n to π* transitions, due to the peptide bond of an α-helix. Attributed to the nucleation of AuNCs, the intensity of α-helix peaks shows a gradual declination with the addition of Au. It shows 85 % reduction in the α-helix with a 30 % increase in the β-sheet after the synthesis of BSA/AuNCs. Therefore, it can be deduced that the interaction between these molecules are complex and cause multidirectional alterations in the structure of the protein. The minimum observed at 220

nm shifts towards lower wavelength, indicating a steady increase in the content of disordered structures in the BSA of AuNCs[149].

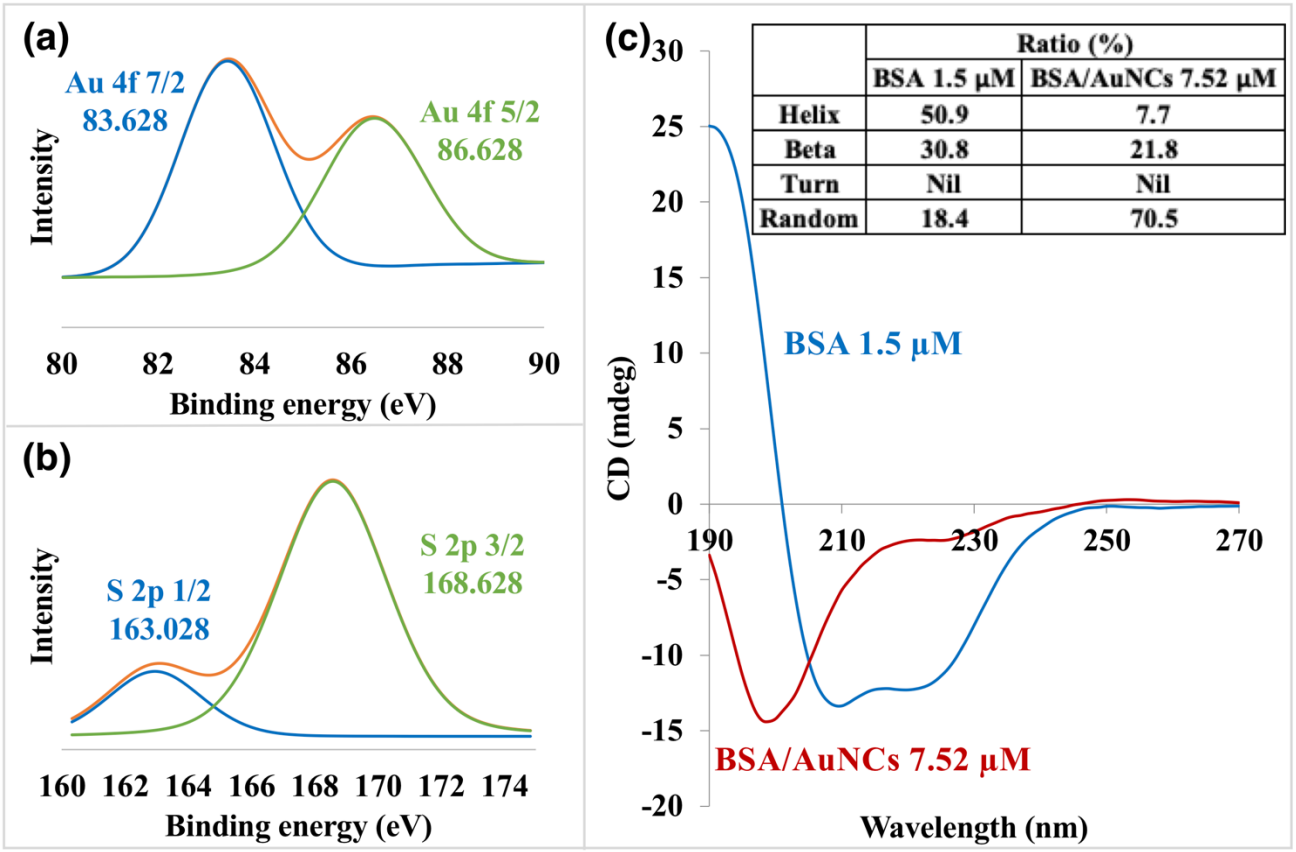

Figure 3.3 Characterisation of BSA/AuNCs. Representative XPS spectra of (a) Au 4f, (b) S 2p and (c) CD spectra of BSA/AuNCs.

3.3.2. Characterisation of FA-rGO

In the UV-vis spectra (Figure 3.4a), the π-π* transition of pterin ring at 282 nm and saddle point at 360 nm of FA were observed in FA-rGO, suggesting the conjugation of FA to rGO[140]. The FA-rGO exhibited characteristic absorption peaks of both FA and rGO. It can be observed that there is no fluorescence peak of FA in the FA-rGO complex between 420 and 630 nm (Figure 3.4b). In the FTIR spectrum of FA-rGO, the original peaks of FA at 3321 and 910 cm^{-1} belonging to O–H (stretching) disappeared. The peak at 1066 cm^{-1} corresponds to the carbonyl group (C–O) of rGO. The new peaks at 3210

(N–H stretching), 1659 (C=O stretching) and 1606 cm^{-1} (N–H bending) in the spectrum indicate the presence of CONH (amide) groups in the FA-rGO (Figure 3.4c).

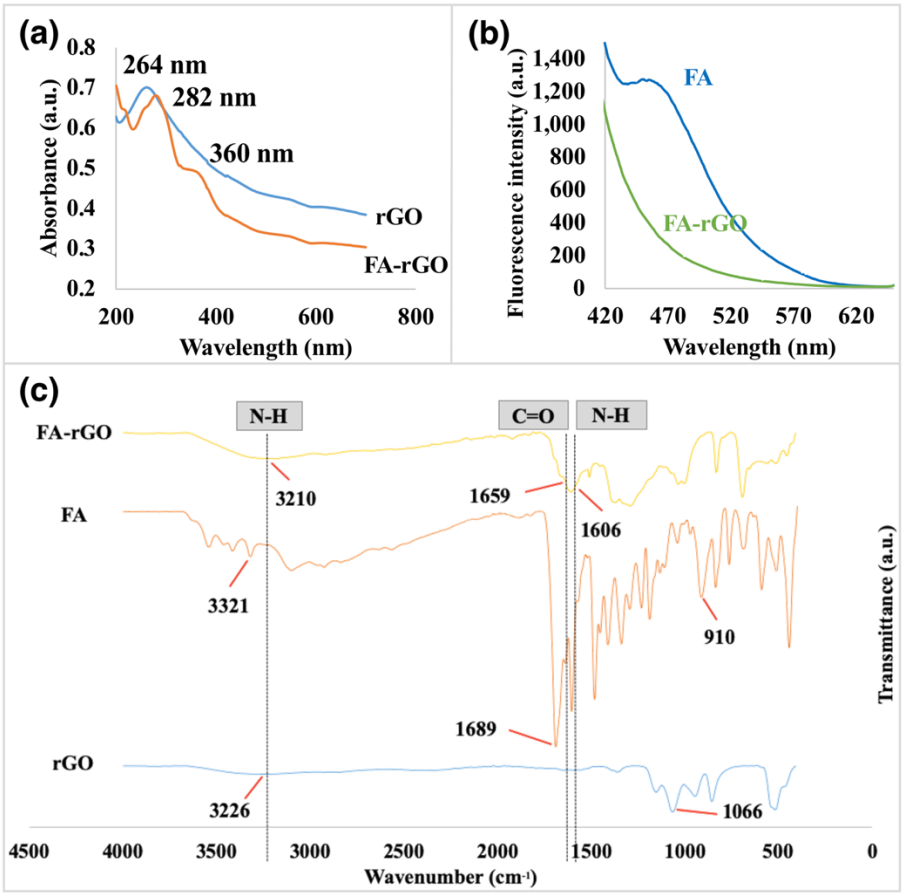

Figure 3.4 Characterisation of FA-rGO. (a) UV-vis spectra of rGO and FA-rGO in aqueous solution. (b) Fluorescence intensity of FA and FA-rGO at λ_{ex}= 365 nm. (c) FTIR spectra of FA, rGO and FA-rGO measured in lyophilised form.

3.3.3. Loading of BSA/AuNCs onto FA-rGO

Conversion of ester, hydroxyl and epoxide groups in the rGO to carboxylic acid groups under strongly basic conditions may improve the aqueous stability of the reduced graphene sheets and facilitate chemical conjugation of biomolecules *via* covalent bonding[64]. FA-rGO acts as a biocompatible biosensor for the detection of FR-positive cancer cells. It is proposed that the binding of BSA/AuNCs onto FA-rGO was non-covalent, driven by hydrophobic interactions and π-π stacking between BSA/AuNCs and aromatic

regions of the rGO sheets[150]. Interaction of BSA/AuNCs with either the metallic core, the stabiliser or the linkage between these two, might interfere with the fluorescence properties[151]. The charge transfer from BSA/AuNCs to FA-rGO weakens the Au-S bond between cysteine residues and the Au core, which in turn reduces charge transfer from BSA ligands to AuNCs, leading to fluorescence quenching of the AuNCs. As displayed in Figure 3.5, the higher the concentration of FA-rGO, the higher the fluorescence quenching of BSA/AuNCs. A relative concentration of 50 $\mu g.mL^{-1}$ of FA-rGO was chosen since the fluorescence of BSA/AuNCs was quenched by about 61 %.

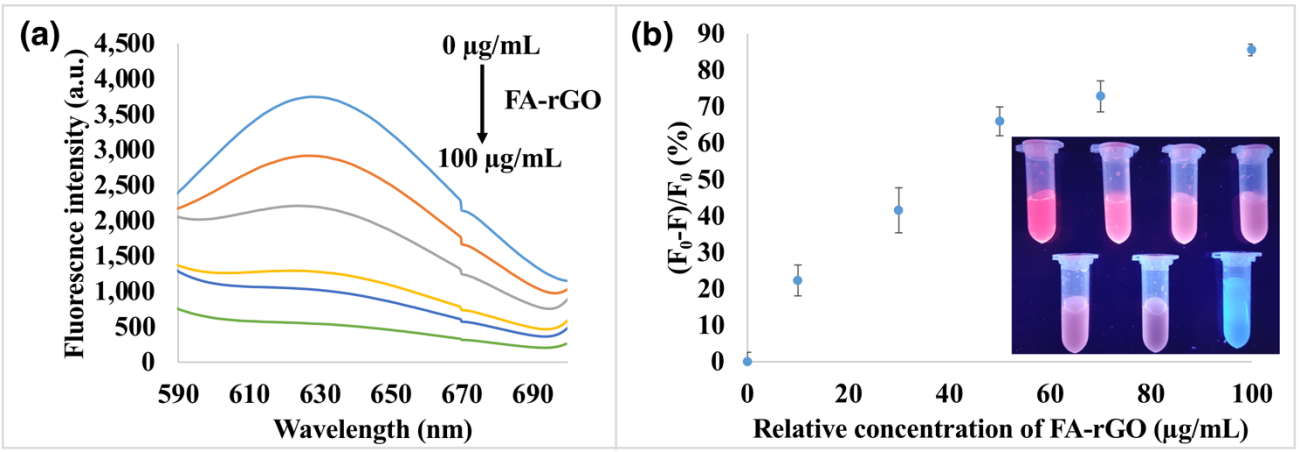

Figure 3.5 Effect of the addition of FA-rGO onto BSA/AuNCs. (a) Fluorescence intensity of 3 $mg.mL^{-1}$ of BSA/AuNCs at λ_{ex}= 365 nm, by varying the concentrations of FA-rGO. The relative concentrations of FA-rGO were 0, 10, 30, 50, 70 and 100 $\mu g.mL^{-1}$. (b) Fluorescence quenching values of 3 $mg.mL^{-1}$ of BSA/AuNCs by varying the concentrations of FA-rGO. Inset: Optical photographs of BSA/AuNCs upon increasing the concentration of FA-rGO under UV light with λ_{ex} at 365 nm (from top left to down right). The last tube is the sample with FA-rGO only. Error bars indicate standard deviation of three independent measurements.

3.3.4. Effect of addition of GSH on the fluorescence intensity of FA-rGO-BSA/AuNCs

As depicted in Figure 3.6, the addition of GSH into the mixture of FA-rGO and BSA/AuNCs gradually quenched its fluorescence. The fluorescence quenching values, $(F_0\text{-}F)/F_0$, showed a linear dynamic range for the concentrations of GSH from 0.25 to 16 µM, which is sensitive to detect the milli-molar concentrations of endogenous GSH in most mammalian cells. As shown in the inset of Figure 3.6c, a linear range from 0 to 1.75 µM as well as a LOD of 0.1 µM and an SNR of 7.68 towards GSH under the physiological pH conditions (pH 7.4) were obtained.

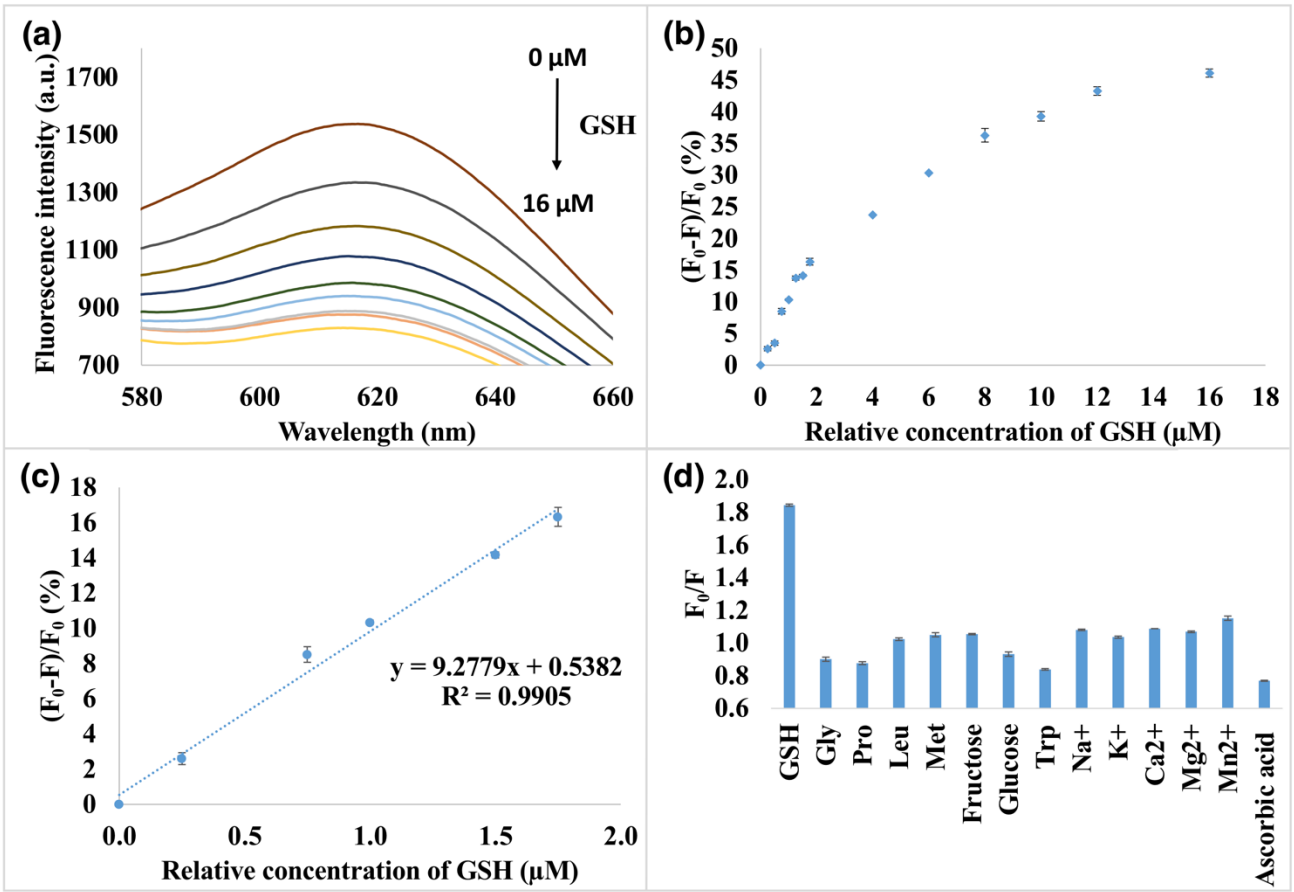

Figure 3.6 Sensitive and selective detection of GSH using FA-rGO-BSA/AuNCs. (a) Fluorescence intensity of FA-rGO-BSA/AuNCs by varying the concentrations of GSH. The relative concentrations of GSH were 0, 2, 4, 6, 8, 10, 12, 14 and 16 µg.mL^{-1} at λ_{ex}= 365 nm. (b) Relationship between the fluorescence quenching values $(F_0\text{-}F)/F_0$ and the target

concentrations. (c) Linear response of the fluorescence quenching values $(F_0\text{-}F)/F_0$ to the concentration of GSH. Error bars are the standard deviation of three repetitive experiments. (d) Selective detection of 0.5 mM GSH in the presence of potentially interfering components. The concentrations of glycine, proline, leucine, methionine, fructose, glucose, Trp, NaCl, KCl, $CaCl_2$, $MgSO_4$ and $MnCl_2{\cdot}4H_2O$ were 5 mM. The concentration of ascorbic acid was 50 mM. F_0 and F are the fluorescence intensities of the sensing system in the absence and presence of GSH (or other potentially interfering chemicals), respectively. Error bars indicate the standard deviation of three independent measurements.

GSH has a sulfhydryl group and a glutamyl linkage in its structure[79], making it a powerful reducing agent and a strong nucleophile that can react with cellular toxicants[152]. GSH plays the role of an antioxidant by scavenging electrophilic and oxidant species[74]. The possible mechanism contributing to the fluorescence quenching of FA-rGO-BSA/AuNCs could be due to the strong interaction (mainly by hydrogen bonding and van der Waals forces) between GSH and BSA on BSA/AuNCs. As a water-soluble biomolecule, BSA provides steric protection and shielding effect to AuNCs when used as a fluorescent probe[153,154]. However, upon addition of GSH, driven by favourable enthalpy and unfavourable entrophy[79], GSH binds within the sub-domain IIA pocket in domain II of BSA (as shown in Supplementary Fig. S3.2)[79]. This changes the conformation of BSA on BSA/AuNCs and forms a GSH-BSA complex[79]. The formation of GSH-BSA complex further destabilises the structure of FA-rGO-BSA/AuNCs and subsequently quenches the fluorescence intensity of BSA/AuNCs.

Sensing strategies based on direct analyte-induced BSA/AuNCs fluorescence change can be simple but comes with the disadvantage of high sample matrix interference, especially in the detection of real samples[155]. This is because the analyte (in this case GSH) tends

to interact with the Au core and ligands of BSA/AuNCs. The interaction may affect the valence state of Au core and form complexes, cluster aggregations or electron flow changes, which will eventually interfere with the fluorescence of BSA/AuNCs[156–158]. Therefore, special functionalisation or modification of BSA/AuNCs are often needed for enhanced biosensing performances. Since covalent binding of FA to rGO can produce stable and biocompatible materials with potential as a nanocarrier in the drug delivery system[159], this is the first study that explores using FA-rGO as a carrier for BSA/AuNCs in the detection of GSH.

To the best of our knowledge, there are no reports on the addition of GSH directly onto BSA/AuNCs. BSA/AuNCs are normally coupled with MnO_2 nanosheets[112], peptide[113], polymer or subjected to growth process[114] before using as an activatable fluorescence probe for GSH sensing. A possible justification for the modification of BSA/AuNCs was to enhance aurophilic interactions of Au(I)-thiolate complexes on the surface of Au(0) core and rigidify the ligand shell. This allows AuNCs to undergo aggregation-induced emission mechanism with enhanced fluorescence intensity[114] while retaining the intrinsic structure of BSA/AuNCs and biological functions of BSA[112,113]. In addition, the surface modification of BSA/AuNCs reduces unwanted intramolecular vibration and rotation[114], enhances biocompatibility and stability, as well as diversifies the potential of BSA/AuNCs in biological applications[113].

A self-quenched BSA/AuNCs for "turn-on" fluorescence imaging of intracellular GSH was reported in 2017[111]. The self-quenched BSA/AuNCs were prepared *via* disulfide bond-induced aggregation of AuNCs. AuNCs act as both energy donor and acceptor. However, compared with the self-quenched AuNCs, the present work is much simpler and straightforward, exhibits higher QY, a lower LOD (up to 40 times) and better selectivity over other interfering species. This study also eliminates ultrasonication and multi covalent coupling procedures.

Another possible reason for fluorescence quenching of FA-rGO-BSA/AuNCs could be ascribed to the formation of GSH-Au^{+} complexes *via* the specific etching reaction of the thiol group of GSH with the core of Au[160]. A similar observation has been reported in AgNCs, in which the biological thiols penetrate the BSA protective layer and chemisorb onto the surface of AgNCs, resulting in the fluorescence quenching of AgNCs[161].

In the present study, the GSH nanobiosensor was designed based on the fluorescence "turn-off" strategy, in which fluorescence quenching occurred when GSH was added to the FA-rGO-BSA/AuNCs. Literature suggested that "turn-on" fluorescence strategy may provide more sensitive results with lower background signal and LOD[162,163]. Therefore, this work serves as a preliminary study for the design of "turn-on" fluorescence strategy with improved selectivity and sensitivity performance. In future work, the effect of the addition of FR, a promising cancer biomarker, on the FA-rGO-BSA/AuNCs can be investigated, which will lay the foundation for concurrent diagnosis and therapy of cancer cells.

3.3.5. Selectivity of the sensing system

Selectivity is an essential parameter for probes in practical applications. The selectivity of the sensing system towards GSH detection over other amino acids and common components of metal ions was evaluated. As shown in Figure 3.6d, the potential interfering compounds (glycine, proline, leucine, methionine, fructose, glucose, Trp, NaCl, KCl, $CaCl_2$, $MgSO_4$, and $MnCl_2{\cdot}4H_2O$) with a concentration of ten times higher than the amount of GSH (5 mM *vs.* 0.5 mM of GSH) did not significantly affect the detection. Notably, the fluorescence intensity of FA-rGO-BSA/AuNCs can be recovered in the presence of ascorbic acid with a concentration of 100 times higher than the amount of GSH (50 mM *vs.* 0.5 mM of GSH). However, the interference of ascorbic acid could be eliminated by pretreatment with *N*-ethylmaleimide (NEM, a thiol blocking agent)[164,165]. Despite the limitation of this approach towards antioxidant such as ascorbic acid,

considering the concentration of GSH in cancer cells which is around 1-10 mM, the proposed sensing strategy exhibited good sensitivity and selectivity towards GSH detection.

3.4. Conclusions

In this study, we have reported a novel nanobiosensor composed of BSA/AuNCs, rGO and FA. It is a new, fast, and facile fabrication method of BSA/AuNCs, with high QY under mild, economical, and eco-friendly synthesis conditions. FA-rGO serving as an effective quencher towards the fluorescence of BSA/AuNCs has been demonstrated successfully, with the quenching intensity of about 61 %. This is due to the effective charge transfer from BSA/AuNCs to FA-rGO, which weakens the Au-S bond between cysteine residues and the Au core of the initially fluorescent BSA/AuNCs complex. Furthermore, a sensitive and selective fluorescent sensing system for GSH detection was demonstrated based on the strong interaction between GSH and BSA on BSA/AuNCs. Our proposed method does not require antibody (more stable in time), biocompatible and uses a simpler and straightforward system that can be further developed into a visual/colorimetric sensor. This study assists in understanding the mechanisms of nanomaterial-mediated fluorescence quenching. It also paves the way to fabricate a “turn-on” or “turn-off” fluorescent nanobiosensor for relevant biomarkers in cancer cells, presenting potential nanotheranostic applications in biological detection and clinical diagnosis.

CHAPTER 4

4. Fluorescence "turn-off/turn-on" biosensing of metal ions by gold nanoclusters, folic acid and reduced graphene oxide

4.1. Introduction

Monovalent cations such as Na^+ and K^+ bind to protein surfaces due to the local cation-specific interactions with the anionic carboxylate group in Glu and Asp side chains on the protein backbone[166]. Inspired by the interesting fact that RNase A can be activated by K and Na salts, our group has designed an effective "turn-off/turn-on" fluorescent sensor for the detection of these two ions using RNase A/AuNCs. RNase A/AuNCs are firstly loaded onto FA-rGO for a fluorescence "turn-off", followed by the fluorescence "turn-on" after the addition of Na^+ and K^+. To the best of our knowledge, this is the first work done on determining the RNase A protein activity in RNase A/AuNCs and exploring the potential application of RNase A/AuNCs towards sensing metal ions. Although the work is preliminary, the current design combines the potential of drug delivery, active targeting, and therapy of cancer cells as well as biosensing of metal ions in a single platform.

In brief, a novel metal ions sensor for the determination of Na^+ and K^+ based on "turn-off/turn-on" fluorescence has been constructed. The sensor possesses the following advantages: (1) composed of entirely biocompatible materials such as RNase A/AuNCs, FA and rGO (2) its excitation (365 nm) and emission (627 nm) wavelengths can minimise the effects of background fluorescence of biological fluids (3) the sensing model can be readily extended to the sensing of other cations by simply using other specific proteins on metal nanoclusters and even to the sensing of other biomolecules. This can be accomplished by the rational design employed, in which different interactions bring metal ions and functional groups on protein to close proximity. Hence, this investigation provides a new type of green nanomaterials for metal ions biosensing with potential in drug delivery[56], active targeting and therapy on cancer cells and biosensing of metal ions.

4.2. Experimental

4.2.1. Reagents and materials

RNase A from bovine pancreas (≥60 %, Sigma) was purchased in lyophilised-powder form and used without further purification. RNase A detection kit and all other reagents were purchased from Sigma Aldrich and used as received. Potassium chloride (KCl) was purchased from Systerm. Sodium chloride (NaCl) and tris-hydrochloride (Tris-HCl) were purchased from Merck.

4.2.2. Synthesis of RNase A/AuNCs

RNase A/AuNCs was synthesised following a modified protocol of Xie *et al.* (2009)[25]. Briefly, 0.7 mL of 12 mM $HAuCl_4$ solution was added to the same amount of aqueous solution containing 20 $mg.mL^{-1}$ RNase A in a thermomixer and mixed at 1200 rpm for 5 min at 40 °C. Then, 0.1 mL of 1 M NaOH solution was introduced, and the mixture was subjected to thermomixer at 900 rpm for 6 h at 60 °C. The colour change of the solution from light yellow to deep brown indicates the successful synthesis of RNase A/AuNCs. The resulting solution was purified using EMD Millipore Amicon Ultra-0.5 centrifugal filter unit with a membrane having a MWCO of 10 kDa to remove residual ions (*i.e*. Na^+, Au^{3+} and OH^-). The products were then stored at 4 °C until further use.

4.2.3. RNase A protein activity assay

The detection of RNase A activity was performed by referring to the technical bulletin of RNase A detection kit. The assay was performed using microplates with a reaction volume of 200 µL. Briefly, control was prepared by mixing 100 µL of RNA solution and 100 µL of water. The blank was prepared by mixing 100 µL of reaction buffer and an equal amount of water. The absorbance of the control and blank were read by UV-vis spectroscopy at A_{300nm} of the control *vs.* blank. The absorbance must be 0.73±0.03 before beginning the assay. Total hydrolysis (E_f) was determined by preparing a triplicate of the mixture of 100 µL of RNA solution and 100 µL of 6 µg/mL RNase A. The

spectrophotometer was calibrated against blank. The absorbance of the triplicate was read at 25 °C for about 120 min at 1-min intervals or until the ΔA_{300nm}/min is <0.002. To measure the rate determination (E_0), the spectrophotometer was calibrated against the blank. A mixture of 100 µL of RNA solution and 92 µL of water was prepared and equilibrated to 25 °C until A_{300nm} remained constant. 8 µL of 2.4 µg/mL RNase A was added to the mixture and immediately mixed by inversion. The decrease in A_{300nm} was recorded for about 10 min. The slope of the line (ΔA_{300nm}/min) was then determined. Rate determination was repeated with 2.4 µg/mL RNase A/AuNCs samples (E_s). The slope of the line was determined using the following equation (4.1).

$$Slope = \Delta \ln\left(E_0 - E_f\right)/\Delta t \quad (4.1)$$

Kunitz units/mL enzyme was calculated based on the following equation (4.2).

$$[(slope)(df)(V_F)]/(V_E) \quad (4.2)$$

Where d*f* is the dilution factor, V_F is the total volume of the assay (in millimetres), and V_E is the volume (in millimetres) of the enzyme used.

4.2.4. Covalent conjugation of FA-rGO

FA-rGO was prepared using a modified protocol reported by Zhang *et al.* (2010)[64]. Briefly, 1 mg.mL^{-1} rGO was subjected to probe sonication (20 kHz, 500 W) for 10 min. NaOH (6.25 mmol) and chloroacetic acid (0.250 g, 11.655 mmol) were then added. The mixture was bath sonicated (40 kHz, 70 W) for 2 h. After neutralisation with HCl, the mixture was purified by repeated rinsing and centrifugation until rGO is well dispersed in deionised water. The mixture was dialysed against deionised water for 24 h. To introduce sulfonate groups to the rGO, sulfanilic acid (51.96 mg, 0.06 M) and sodium nitrite (70.720 mg, 0.205 M) were dissolved in 20 mL of 0.25 v/v % 1 M NaOH. The solution was added dropwise to 0.1 M HCl in an ice bath. The sulfonated groups were mixed with rGO in an ice bath under stirring for 2 h, followed by dialysis against deionised water for over 24 h. The mixture was stored at 4 °C until further use. EDC and NHS were added

onto rGO, with the molar ratio of rGO:EDC:NHS as 40:50:73. The mixture was subjected to probe sonication for 2 h. FA (5 mg mL^{-1}, dissolved in 0.5 M $NaHCO_3$, at pH 8) was added and stirred overnight. The products were dialysed against 0.5 M $NaHCO_3$ for 24 h, followed by dialysis against deionised water for over 24 h. The products were characterised by FTIR, UV-vis spectroscopy and fluorescence spectrophotometer.

4.2.5. Fluorescence quenching of RNase A/AuNCs by FA-rGO

To investigate the potential of FA-rGO to induce fluorescence quenching of RNase A/AuNCs, different concentrations of FA-rGO were added to 8 $mg.mL^{-1}$ of RNase A /AuNCs. The solution was mixed in a thermomixer at 900 rpm for 10 min at room temperature. The fluorescence intensity of the solution was recorded at an λ_{ex} of 365 nm.

4.2.6. Sensing of potassium and sodium ions

The detection of K^+ and Na^+ ions were conducted as follows. The same volume of FA-rGO-RNase A/AuNCs was added with various concentrations of K^+. The solution was mixed in a thermomixer at 900 rpm for 20 min at room temperature. The fluorescence intensity was measured to quantify the concentration of K^+ at λ_{ex}= 365 nm. The steps were repeated for the detection of Na^+. The experiments were repeated with RNase A/AuNCs only, without FA-rGO.

4.3. Results and Discussion

4.3.1. Synthesis and characterisation of RNase A/AuNCs

To the best of our knowledge, the only study on the fabrication and application of RNase A/AuNCs was conducted by Kong *et al.* (2013)[10]. The group presented a nanoplatform composed of vitamin B_{12}-coupled RNase A/AuNCs for simultaneous targeting and imaging of tumour sites. The group synthesised RNase A/AuNCs using a typical modified protocol introduced by Xie *et al.* (2009)[25]. The fabrication method, however, requires long incubation time (up to 12 h) and needs high protein concentration (50 mg mL^{-1}). In this

work, RNase A/AuNCs was prepared using the protocol introduced by our group Wong *et al.* (2021)[167]. The method is facile, convenient and takes shorter synthesis time of only 6 h.

HRTEM image (Figure 4.1A) demonstrates that the sizes of RNase A/AuNCs fall within a narrow range of less than 2 nm. RNase A/AuNCs are generally spherical dots demonstrating uniform size with high monodispersity. As shown in the optical absorption of the as-prepared RNase A /AuNCs (Figure 4.1B), no apparent SPR absorption peak could be observed in the range between 400 and 600 nm. This confirms the encapsulation of AuNCs in RNase A protein, and most importantly, no large NPs (>2 nm in diameter) were formed[146].

Besides, the as-synthesised RNase A/AuNCs exhibited bright red fluorescence under UV irradiation (Figure 4.1B), with the emission band at 645 nm when excited at 365 nm. Most of the fluorophores used for metal ions sensing have emission wavelength below 600 nm, which might lead to light-induced toxicity, weak tissue penetration, low resolution, auto-fluorescence and light absorption of biomolecules[115]. It is preferable to design low-energy NIR fluorescent sensors with long-wavelength to overcome the shortcomings mentioned above. The photoluminescence QY was about 7.46 % when calibrated with rhodamine B, which has a QY value of 31 % in water when excited at 514 nm.

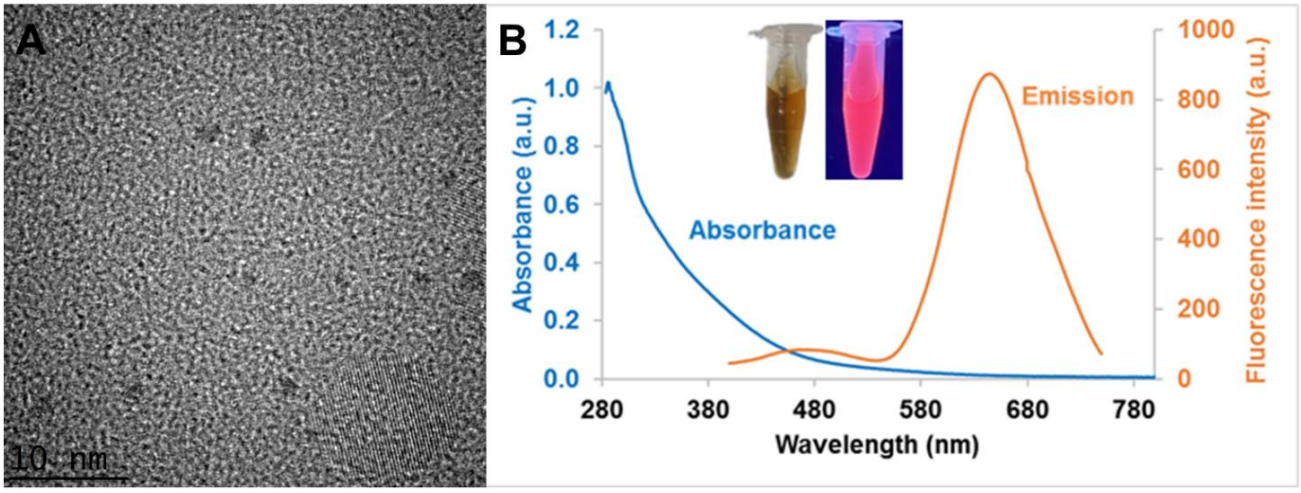

Figure 4.1 Characterisation of RNase A/AuNCs. (A) HRTEM image of the diluted fluorescent RNase A/AuNCs. (B) UV-vis absorption (blue line) and fluorescence emission spectra (orange line) of the as-prepared RNase A/AuNCs with λ_{ex} at 365 nm. Inset: Optical photographs of the RNase A/AuNCs under visible (left) and UV light (right).

RNase A is a single domain protein with two-subdomain portions which contain 124 amino acid residues comprising of 3 α-helices, 7 short β-strands and loops connecting them. As shown in Figure 4.2, the native RNase A is stabilised by four disulfide bonds (Cys26-Cys84, Cys40-Cys95, Cys58-Cys110 and Cys65-Cys72) and two *cis*-peptide bonds before prolines (Pro93 and Pro114)[34]. At a temperature higher than 50 °C, the protein becomes unstable as the high kinetic energy of the chain disrupts the protein structure. The protein is in a reversible transition state between unfolded and compact state. RNase A protein becomes completely denatured, compact and biologically inactive above 67 °C[168,169]. Therefore, a temperature of 60 °C was chosen for the synthesis, instead of the physiological temperature (37 °C). This is because, upon heating, the Phe46 residues located in the hydrophobic core of RNase A will be replaced with other hydrophobic amino acid residues. This will result in a marked decrease in the thermal stability and unfolding of RNase A, making the compact native form of RNase A to

become flexible and reactive[170]. A higher interaction between RNase A and Au ions fastens the formation of RNase A/AuNCs.

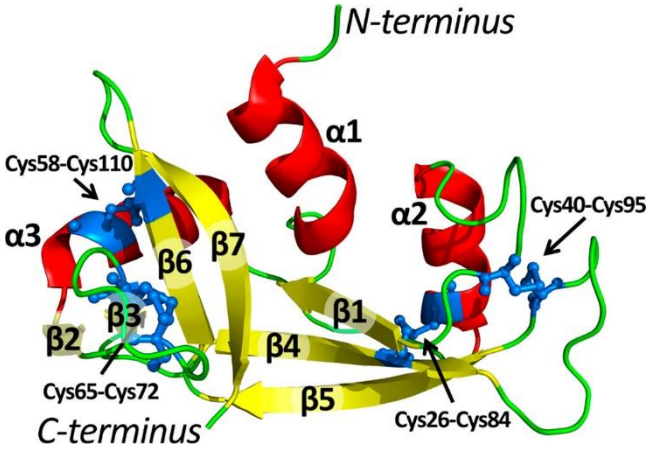

Figure 4.2 Characterisation of RNase A/AuNCs. Cartoon representation of RNase A. Reprinted with permission from ref.[34], ACS Publications, 2017.

XPS was employed to investigate the protein-AuNCs interactions and to prove the reducibility of the protein against Au(III) ions in alkaline pH (Figure 4.3). As shown in Figure 4.3A, the XPS of Au 4f and the binding energies at 83.811 eV (Au $4f_{7/2}$) and 87.311 eV (Au $4f_{5/2}$) confirm the formation of stable RNase A/AuNCs, with most of the Au atoms close to the oxidation state of Au(0). The two S 2p bands with the binding energies of about 163 (S $2p_{1/2}$) and 169 eV (S $2p_{3/2}$) were observed (Figure 4.3B), corresponding to the gold-bound (Au-S) and oxidised sulfur species, respectively.

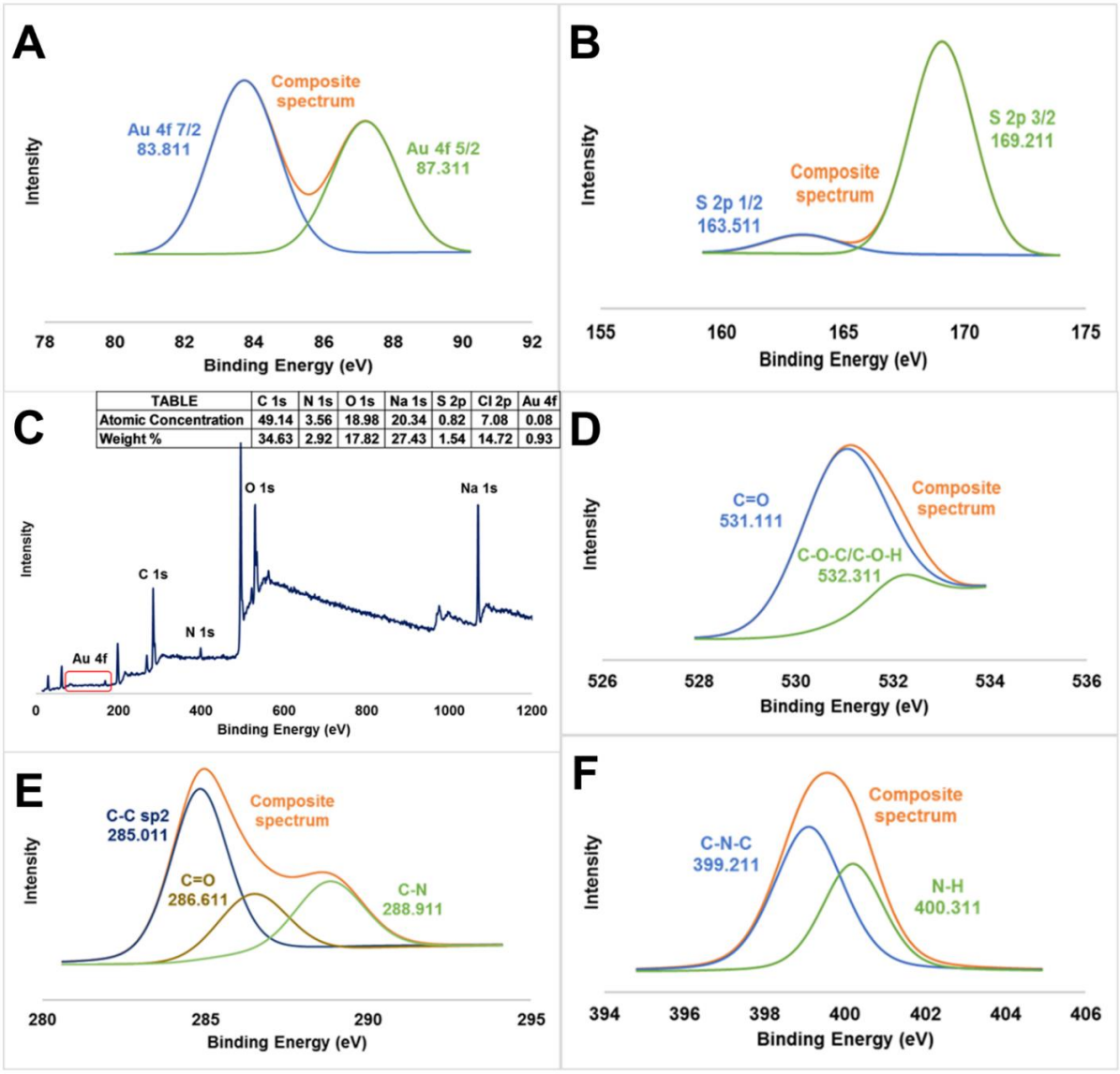

Figure 4.3 Characterisation of RNase A/AuNCs. Representative XPS spectra of (A) Au 4f, (B) S 2p, (C) full range, (D) O 1s, (E) C 1s and (F) N 1s of RNase A/AuNCs.

CD spectroscopy was employed further to investigate the conformational evolution of native and AuNCs-bound proteins. From the CD spectra, as shown in Figure 4.4, a broad negative band with protrusions at 209 nm for α-helix and 218 nm for β-sheet was observed for RNase A. Attributed to the nucleation of AuNCs, the intensity of α-helix peaks declines with the addition of Au. It shows a 100 % reduction in the α-helix and a 31 % decrease in the β-sheet after the synthesis of RNase A/AuNCs. The valley at 218 nm becomes markedly shallower and blue shifts to about 198 nm after the cluster

formation, indicating an increase in the disordered and random coil structures in the RNase A/AuNCs (due to protein unfolding). Therefore, it can be deduced that the interaction between these molecules are complex and cause multidirectional alterations in the structure of the protein.

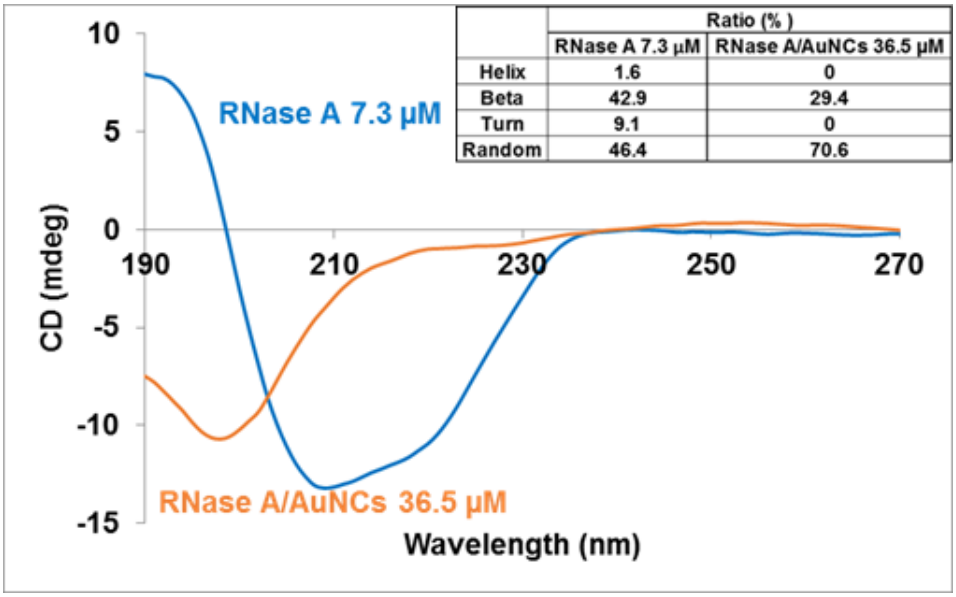

Figure 4.4 Characterisation of RNase A/AuNCs. CD spectra of RNase A/AuNCs.

4.3.2. RNase A protein activity assay

Depending on the reaction conditions, protein templated AuNCs are formed either under protein-denatured or native condition[171]. The encapsulation of the AuNCs inside the protein template might interfere with the protein structure and activity. Since RNase A is a therapeutic protein, it is important to preserve the native protein structure to retain its biological activity after the formation of AuNCs.

Although advanced analytical methods are available to investigate the protein activity, most depend on expert operators and capital equipment that are often low throughput and prohibitively expensive[172]. None of the work has been conducted on studying the activity of the protein RNase A in the bioconjugate, RNase A/AuNCs. UV spectroscopy is

a fast, simple, and inexpensive method to determine protein activity or structure, protein-protein, and protein-ligand interactions[172].

In general, RNase A converts RNA to oligonucleotides in the presence of water. RNase A primarily absorbs UV light with absorbance maxima at 300 nm. Hence, RNase A activity was calculated after monitoring the decrease in absorbance at 300 nm upon hydrolysis at 25 °C. The E_f value was determined by plotting a graph of absorbance *vs.* time (Figure S4.1A). The slope of the line was observed as 0.6417. Rate determination of RNase A and RNase A/AuNCs *vs.* blank were plotted (Figure S4.1B). The graphs of $\ln(E_0-E_f)$ and $\ln(E_s-E_f)$ *vs.* time were plotted (Figure S4.1C). The final activity of RNase A samples was calculated using equation (4.2). The RNase A in RNase A/AuNCs sample was found to be 50.8% active and can exert ribonucleolytic activity against RNA[173,174].

4.3.3. Loading of RNase A/AuNCs onto FA-rGO

Functionalisation of biomolecules on the surface of GO-based nanosystem enhances the catalytic activity, leading to increase in electrode surface area and active sites for electron capture in solution. The GO-based nanosystem owns π-π stacking interaction which induces facile electron transfer between the nanosystem, and target analytes[136]. FA-rGO targets the FR-positive cancer cells, as well as acts as a novel nanocarrier for the co-delivery of genes and drugs for enhanced cancer therapy[175]. The loading of RNase A/AuNCs onto FA-rGO was driven by hydrophobic interactions and π-π stacking between RNase A/AuNCs and aromatic regions of the rGO sheets[150]. Graphene-based oxides are known to decrease the photo-emission of the fluorescent molecule *via* the photo-induced charge transfer from the fluorophore to the oxide surface[176]. The interaction of RNase A/AuNCs with either the metallic core, the stabiliser or the linkage between these two, might interfere with the fluorescence properties[151]. The charge transfer from RNase A/AuNCs to FA-rGO weakens the Au-S bond between cysteine residues and the Au core, which in turn reduces charge transfer from RNase A ligands to AuNCs, leading to

fluorescence quenching of AuNCs. As displayed in Figure 4.5, the higher the concentrations of FA-rGO, the higher the fluorescence quenching of RNase A/AuNCs. A relative concentration of 50 μg.mL^{-1} of FA-rGO was chosen since the fluorescence of RNase A/AuNCs was quenched by about 15 %.

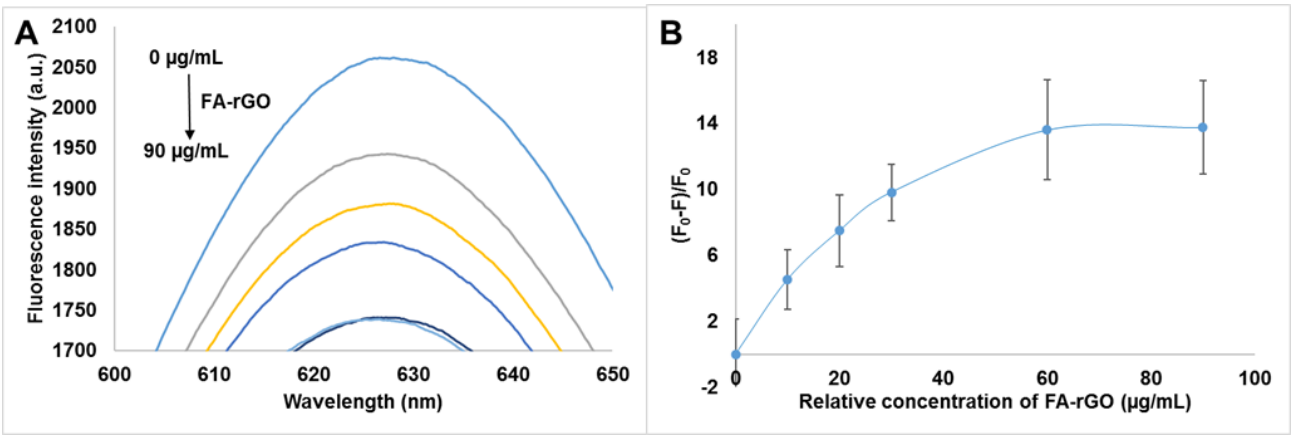

Figure 4.5 Effect of addition of FA-rGO onto RNase A/AuNCs. (A) Fluorescence intensity of 8 mg.mL^{-1} of RNase A/AuNCs at λ_{ex}= 365 nm, by varying the concentration of FA-rGO. The relative concentrations of FA-rGO were 0, 10, 20, 30, 60 and 90 μg.mL^{-1}. (B) Fluorescence quenching values of 8 mg.mL^{-1} of RNase A/AuNCs by varying the concentration of FA-rGO. Inset: Error bars indicate the standard deviation of three independent measurements.

4.3.4. Effect of addition of potassium and sodium ions on the fluorescence intensity of RNase A/AuNCs and FA-rGO-RNase A/AuNCs.

K^+ is one of the predominant ions in living cells with extracellular concentration (in serum) of around 3.5-5.3 mM[115,120,121]. The normal concentrations of K^+ are about 40-120 mM in urine, 5-10 mM in sweat and about 30 mM in saliva[131]. Erythrocytes and epidermal cells have higher intracellular K^+ with homeostasis concentrations of 200 and 475 mM, respectively, while the intracellular K^+ concentration for myocytes is even higher (at mole levels)[125].

In this study, the effect of the addition of Na^+ and K^+ ions on the fluorescence intensity of RNase A/AuNCs and FA-rGO-RNase A/AuNCs is investigated. As depicted in Figure S4.2, the addition of K^+ into RNase A/AuNCs increased its fluorescence, with a linear dynamic range from 0 to 800 mM as well as a LOD of 74 mM. On the other hand, Figure 4.6 show that the addition of K^+ into FA-rGO-RNase A/AuNCs recovered its fluorescence, with a linear dynamic range from 0 to 125 mM as well as a LOD of 15.7 mM under physiological conditions (pH 7.4). It is observed that the nanoplatform which initially quenched by FA-rGO can achieve 4.7-fold lower LOD than the nanoplatform composed of RNase A/AuNCs only. Both these nanoplatforms exhibit "turn-on" fluorescence of about 14-15 % and are sufficiently sensitive to detect the intracellular concentrations of K^+ which is typically about 150 mM.

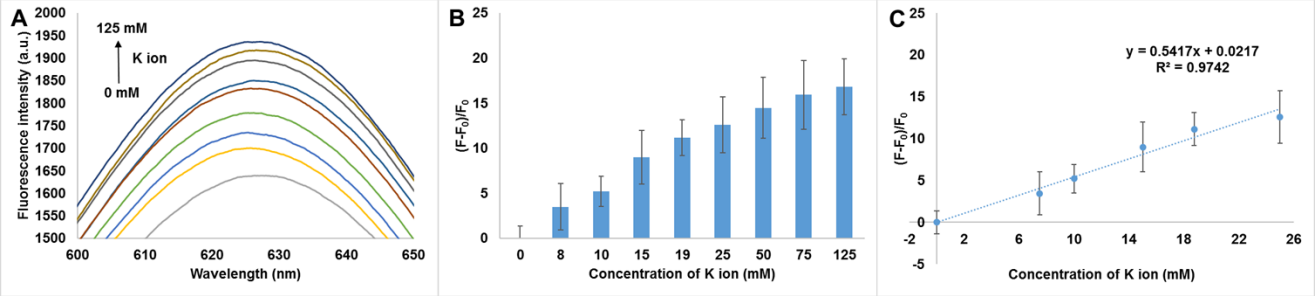

Figure 4.6 Sensitive detection of K^+ using FA-rGO-RNase A/AuNCs. (A) Fluorescence intensity of FA-rGO-RNase A/AuNCs by varying the concentration of K^+. The relative concentrations of K^+ were 0, 7.5, 10, 15, 8.75, 25, 50, 75 and 125 mM at λ_{ex}= 365 nm. (B) Relationship between the fluorescence recovery values $(F-F_0)/F_0$ and the target concentrations. (C) Linear response of the fluorescence recovery values $(F-F_0)/F_0$ to the concentration of K^+. Error bars are the standard deviation of three repetitive experiments.

Clinical trials showed that the recommended Na^+ intake in adults should be below 100 mmol (about 2.3 g of Na^+ or 5.8 g of salt per day)[136]. Any deviation in the blood ionic equilibrium may increase the risk of stroke, heart failure, diabetes, and kidney problems[118,128,136]. As shown in Figure S4.3, the addition of Na^+ into the RNase A/AuNCs enhanced its fluorescence, with a linear dynamic range from 0 to 700 mM and a LOD of 49 mM. Meanwhile, Figure 4.7 demonstrates that the addition of Na^+ into FA-rGO-RNase A/AuNCs recovered its fluorescence, with a linear dynamic range from 0 to 1000 mM as well as a LOD of 110 mM of Na^+ under a pH of 7.4. The nanoplatform with RNase A/AuNCs achieved only 2.2-fold lower LOD than the nanoplatform that was initially quenched with FA-rGO. Both nanoplatforms displayed a "turn-on" fluorescence of about 19-20 % and are satisfactory to detect the normal concentration of Na^+ in serum which is around 135-148 mM under physiological conditions[118,121].

It is speculated that the fluorescence "turn-on" mechanism after the addition of Na^+ and K^+ is due to photo-induced intramolecular electron transfer, a method for the sensitive detection of cations in solution based on a host-guest (ion) recognition site that is covalently linked to a chromophore[126]. Na^+ and K^+ binding to the protein RNase A surface is due to the local cation-specific interactions with the anionic carboxylate group in Glu and Asp side chains on the protein backbone[166].

In addition, Na^+ and K^+ possess the same charge and are closely similar in ionic radius (116 and 152 pm, respectively) as well as spatial orbital design[131]. Even though Na^+ has a smaller ionic radius, but it possesses a higher charge density and larger hydrated radius than K^+[177]. Based on the simple electrostatic arguments, a cation and an anion with similar hydration energies tend to form contact ion pairs in aqueous solutions. Na^+ tends to bind stronger and has a higher affinity (at least twice) to the anionic groups on the protein surface than K^+[166]. For example, RNase A protein effectively binds to 1-2 Na^+ and fewer than half the number of K^+[166]. At the same time, Na^+ becomes more strongly

hydrated than K^+ as the free energy barrier increases. The removal of one water molecule from the first hydration shell (in order to facilitate a direct contact) becomes increasingly difficult[178]. Eventually, the ion binding kinetics of Na^+ gets slower. Therefore, it can be observed that the fluorescence recovery of RNase A/AuNCs after the addition of Na^+ was higher with higher LOD than K^+.

Another possible mechanism of the fluorescence "turn-on" after the addition of Na^+ and K^+ could be due to the oxidation/reduction reactions. In an aqueous solution, water molecules dissociate to form hydrogen and hydroxyl ions that can be adsorbed onto the majority of the metal oxide. The metal ions diffuse into RNase A/AuNCs, interact *via* ion-exchange reactions with both positive and negative sweeps on the protein and FA-rGO surfaces. They donate/accept a proton from the solution to form a negative and positive surface group, respectively[136]. Therefore, the fluorescence intensity of RNase A/AuNCs is recovered upon binding to Na^+ and K^+.

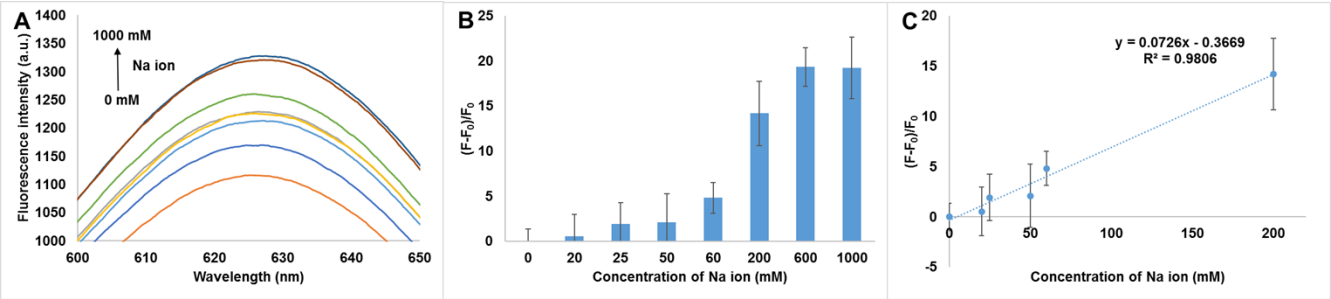

Figure 4.7 Sensitive detection of Na^+ using FA-rGO-RNase A/AuNCs. (A) Fluorescence intensity of FA-rGO-RNase A/AuNCs by varying the concentration of Na^+. The relative concentrations of Na^+ were 0, 20, 25, 50, 60, 200, 600 and 1000 mM at λ_{ex}= 365 nm. (B) Relationship between the fluorescence recovery values $(F-F_0)/F_0$ and the target concentrations. (C) Linear response of the fluorescence recovery values $(F-F_0)/F_0$ to the concentration of Na^+. Error bars are the standard deviation of three repetitive experiments.

4.4. Conclusions

In this study, a novel nanobiosensor for the detection of metal ions using RNase A/AuNCs-based platform has been reported. RNase A/AuNCs is synthesised using a facile and optimised protocol. The activity of RNase A protein after the formation of RNase A/AuNCs is investigated using RNA detection, in which 50.8 % of RNase A was found to be active in RNase A/AuNCs. RNase A/AuNCs is then loaded onto FA-rGO. FA-rGO is used as a potential carrier and fluorescence quencher for RNase A/AuNCs. Finally, a fluorescence "turn-on" sensing strategy is developed using the as-synthesised FA-rGO-RNase A/AuNCs for the detection of Na^+ and K^+ ions. The developed nanobiosensor reveals an excellent sensing performance and meets the sensitivity required for the detection of both intracellular Na^+ and K^+ ions. Although the selectivity data for the nanobiosensor have not been investigated, the selectivity is expected to increase following pretreatment with blocking agents such as NEM. To the best of our knowledge, this is the first work done on exploring the potential application of RNase A/AuNCs as a metal ion sensor. This work serves as a proof-of-concept for combining the potential of drug delivery, active targeting, and therapy on cancer cells and biosensing of metal ions in a single platform.

CHAPTER 5

5. Development of an electrochemical sensing platform for determination of folate receptor using laser scribed graphene electrodes

5.1. Introduction

High resolution printed electrodes/chips on plastic or paper substrates are emerging technologies in the sensors and electronics field[179]. Examples of printed devices are LEDs, solar cells, RFID tags, energy harvesters and capacitors[180]. With the advantages of lower fabrication cost, larger surface area, increased flexibility, transparency and conductivity[181], printed sensors, and electronics have shown diverse potential in diagnostics[182].

Graphene is well known for its high electrical conductivity, mechanical flexibility and strength, chemical stability, and biocompatibility. As a graphene precursor, GO can transform into rGO *via* chemical and photo-reduction process[179]. rGO is a conductive material with semi-metallic-like behaviour. The reduced oxygen-carbon ratio of rGO makes it suitable for various chemical and biosensing applications. Recently, highly conductive graphene-based thin films on flexible substrates were fabricated using a facile 3-step process[179]. The three steps include filtering of GO *via* nitrocellulose membranes; laser reduction of GO surface; and lastly transferring of the resulting rGO pattern onto new substrates *via* stamping method.

FA is an electroactive compound of biological origin[35,36,183]. Since electroanalytical methods are fast, simple, sensitive, and cost-effective, it will be advantageous to use electrochemical approaches, as a proof-of-concept, to demonstrate the sensing of FR using an FA-functionalised GO platform.

In this work, different high-resolution printing techniques were tested for direct patterning and rGO transfer to several substrates such as photographic paper, nitrocellulose membrane and plastic. The working and counter electrodes were laser scribed directly on the membrane filter (MF) containing a uniform layer of GO and FA. The MF was subjected to laser reduction, and only the reduced part was transferred onto the substrate. This was to prepare functional laser scribed GO and GO-FA electrodes.

Different electrochemical approaches (cyclic voltammetry, differential pulse voltammetry, chronoamperometry, *etc*.) were employed to investigate the interaction between FR and FA using laser scribed GO-FA electrodes. All the activities carried out were clearly reported and summarised in the following flow chart.

This fundamental research can be progressively employed to design laser scribed GO-FA electrodes functionalised with RNase A/AuNCs. Such an excellent sensing platform paves the way for rapid tumour diagnosis in future clinical application.

5.2. Flow chart of the experimental methodology

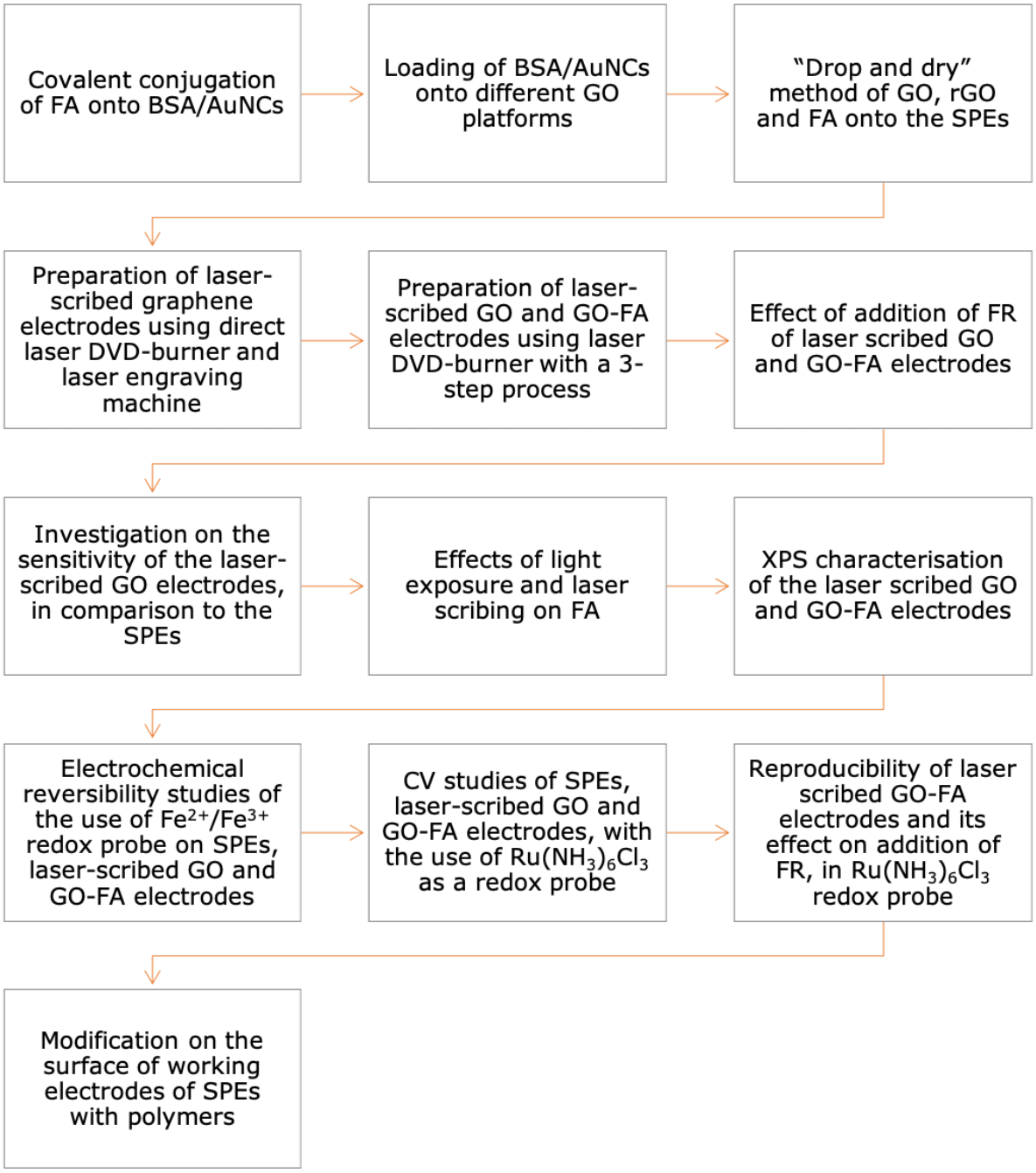

5.3. Experimental

5.3.1. Reagents and materials

BSA (96 %, Sigma Aldrich) was purchased in lyophilised powder form and used without further purification. $HAuCl_4$ solution, FA, human FR beta (≥95 %), EDC, NHS, poly(vinyl alcohol) (PVA), poly(ethylene glycol) (PEG), hexaammineruthenium (III) chloride $[Ru(NH_3)_6Cl_3]$ redox probe, ferrocyanide/ferricyanide $[Fe(CN)_6]^{3-/4-}$ (or Fe^{2+}/Fe^{3+}) redox probe, and all other reagents were purchased from Sigma Aldrich and used as received. Ultrapure deionised water was obtained from a Milli-Q system (Purelab Option-Q). NaOH (1 M) and phosphate-buffered saline (10x, PBS) were purchased from Nacalai Tesque.

5.3.2. Graphene oxide filtering, reduction, and transfer

GO (10 mg/mL) was purchased from Angstrom Materials (solution N002-PS-1.0) and Graphenea. The hydrophilic MF (Millipore) used had a pore size of 0.025 μm and 47 mm of diameter. Aqueous suspensions at various concentrations were filtered through the membrane using a 1 L vacuum-filtering flask, 300 mL glass filter holder and 47 mm SS screen. The reduction process was made *via* DVD-burner enabled with lightscribe technology, and the drawings were made with Corel Draw software. The lightscribe laser works at 780 nm length with a resolution of 600 dots per inch[184]. The reduced pattern was transferred on new substrates using a laboratory hydraulic press machine with a pressure of 12 ton. The new substrates were subjected to plasma cleaning using a plasma cleaner (Harrick Plasma, USA).

5.3.3. Surface characterisation

The reduction efficiency was assessed *via* XPS measurements, using a Phoibos 150 hemispherical energy analyzer (SPECS GmbH, Berlin, Germany).

5.3.4. Electrochemical characterisation

All the electrochemical measurements were performed using a potentiostat/galvanostat (Metrohm PGStat302) connected to a computer equipped with the software General Purpose Electrochemical System (GPES, version 4.9.007).

5.3.5. Analytical measurements

Fluorescence spectra and UV-vis absorbance were recorded using a multi-mode microplate reader (SpectraMax M3). Hydrophobic channel/wells were created on nitrocellulose paper strips using a wax printer (Xerox ColorQube 8580). For laser scribing, laser engraving machine (Developower) was operated with Benbox laser engraver software.

5.3.6. Covalent conjugation of FA onto BSA/AuNCs

FA was conjugated to amino groups on the surface of AuNCs to form FA-conjugated BSA/AuNCs (FA-BSA/AuNCs) nanoprobes. First, FA was reacted with EDC/NHS, with the molar ratio of FA:EDC:NHS as 2:3:4, in 1 mL of PBS solution at pH 7.4. The relative concentrations of FA were 0.1, 0.2, 0.5, 0.7 and 1.0 mg/mL. The mixture was bath sonicated in the dark for 2 h at 50 °C. Then, the same amount of BSA/AuNCs was added onto the mixture. The final mixture was mixed overnight using thermomixer at 650 rpm. All the samples were subjected to fluorescence and absorbance measurements.

The experiment was repeated with the molar ratio of FA:EDC:NHS as 1:3:4. As a control, a sample of 1 mg/mL of FA was prepared and added with BSA/AuNCs, without the addition of EDC/NHS. In addition, another control was prepared, where EDC/NHS was added to the BSA/AuNCs, without FA. Few samples were selected and subjected to purification by EMD Millipore Amicon Ultra-0.5 centrifugal filter units with a membrane MWCO of 30 kDa, at 14 000 g for 10 min. This was done to compare the effect of purification on the fluorescence intensity of FA-BSA/AuNCs and to ensure all the FA was conjugated onto BSA/AuNCs.

To investigate the interaction of FR with FA-BSA/AuNCs, an experiment was conducted to determine if FR could recover the fluorescence quenching of FA-BSA/AuNCs. A 75 µL of 1 µg/mL FR was added to the selected FA-BSA/AuNCs samples. The fluorescence intensity of each sample was measured using a multi-mode microplate reader. The experiment was repeated with 2 µg/mL FR. BSA was used as a control.

5.3.7. Loading of BSA/AuNCs onto different GO platforms

Hydrophobic channel/wells were created on nitrocellulose paper strips using a wax printer. The diameter of each well was about 5±0.25 mm. Different concentrations of GO, ranging from 0-2 mg/mL, were subsequently loaded onto the wells. Each well required 20 µL of GO solution. The nitrocellulose paper strips were air-dried overnight. Subsequently, 5 µL of BSA/AuNCs were loaded onto each well. The fluorescence intensity of the BSA/AuNCs was observed under a UV lamp. To quantify the fluorescence intensity of BSA/AuNCs, pictures of the hydrophobic wells were taken with a smartphone, immediately and after 3 h. Evaluation of the fluorescence quenching of the BSA/AuNCs was performed using ImageJ.

5.3.8. "Drop and dry" method of GO, rGO and FA on the screen-printed electrodes (SPEs)

SPEs were prepared and initially tested with PBS supporting electrolyte. This was to ensure that SPEs were functional and displayed CV response. Different concentrations of GO and rGO were prepared. The relative concentrations of GO were 0.2, 1.0 and 5.0 mg/mL while the concentration of rGO was 0.1 mg/mL. rGO selected was synthesised using the protocol reported by Muthoosamy *et al.* (2015)[144]. rGO was subjected to probe sonication of 20 kHz at 500 W for 1 h before use. The concentrations of FA were 0.2, 1.0 and 5.0 mg/mL. A 3 µL of each solution (GO, rGO and FA) was drop-casted onto the working electrode of the SPEs by ensuring the surface area of the working electrode was fully covered. Three replicates were prepared for each solution at each concentration.

The SPEs were air-dried before subjecting to cyclic voltammetry (CV) and differential pulse voltammetry (DPV), with PBS and Fe^{2+}/Fe^{3+} redox probe. The final concentration of Fe^{2+}/Fe^{3+} redox probe was 1.57 mM.

5.3.9. Preparation of laser-scribed graphene electrodes using direct laser DVD-burner and laser engraving machine

For laser scribing, two different laser machines were used. First, the laser engraving machine (as shown in Figure 5.1A) was operated with Benbox laser engraver software. The machine was operated with the settings: low light intensity (2^{16}), intensity (2^{255}), speed (800 mm/s), time (200 ms), 1-step with a scan by line carve mode and a continuous engraving. For direct laser reduction on the DVD drive, CDBurnerXP and LightScribe software were used. The design of the electrodes for laser scribing using DVD drive is shown in Figure 5.1B. For each electrode, only the working electrode and counter electrode were reduced by laser. The reference electrode was hand-drawn with silver inks after the laser reduction was completed.

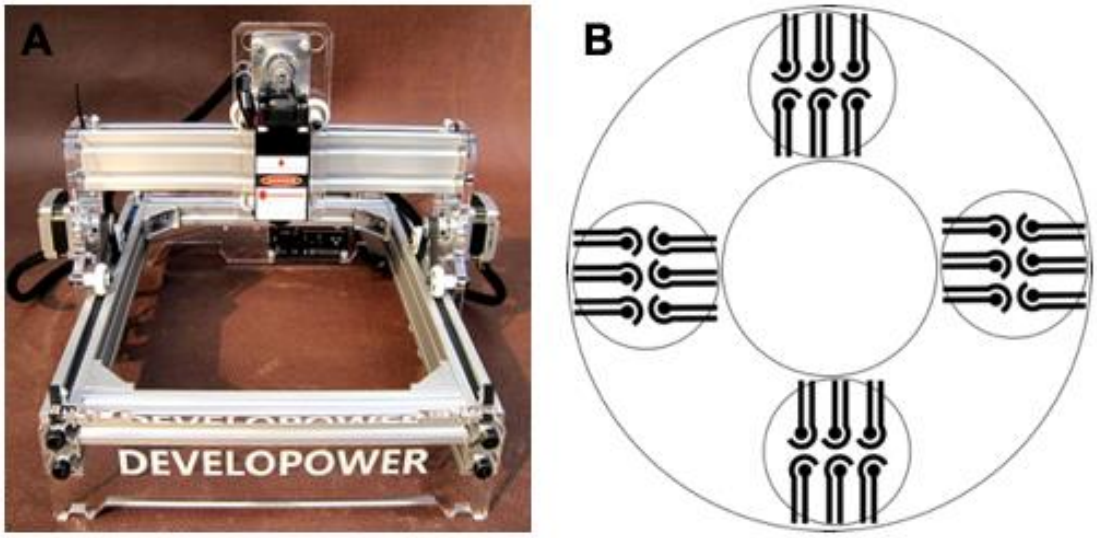

Figure 5.1. Preparation of laser-scribed electrodes. (A) Laser engraving machine. (B) Design of the electrodes for laser scribing on a DVD drive.

The electrochemical measurements of the laser scribed electrodes were performed with Autolab GPES software. The scan rate was 100 $mV.s^{-1}$. CV and chronoamperometry (CA) were used to study the parameters such as anodic and cathodic peak potential and current density. CV was recorded at the start potential from -0.8 V to first vertex potential at 1.2 V, followed by second vertex potential at -0.8 V, with a scan rate of 100 $mV.s^{-1}$ with a step potential of 5 mV. DPV was recorded within the potential range from -0.8 to 0.8 V under modulation amplitude of 25 mV with a step potential of 10 mV. Four different approaches were attempted to determine the most suitable method and substrate for the fabrication of laser-scribed graphene electrodes.

5.3.9.1. Laser scribing of MF loaded with the mixture of GO and FA on the DVD drive

A 70 mL of 1 mg/mL GO was sonicated using ultrasonic probe at 125 W for 2 h to form NGO (nano-GO). A 20 mL of 1 mg/mL NGO was mixed with 3.5 mL of 2.5 mg/mL FA. The mixture was subjected to magnetic stirring overnight. A 5 mL of the mixture was filtered using MF with a pore size of 0.025 µm. The bottom of the MF was dried using nitrogen gas. Then, the MF was attached on DVD drive using double-sided tape. Laser scribing was done on the working electrode only, with 3-reduction steps.

5.3.9.2. Laser scribing of PET drop-casted with the mixture of GO and FA on the DVD drive

A 30 mL of 10 mg/mL NGO was mixed with 15 mL of 10 mg/mL FA. At the same time, polyethylene terephthalate (PET) was treated with a plasma cleaner for 8-10 min. Then, about 8-10 mL of the mixture was drop-casted onto the PET and allowed for homogenous deposition. The PET was dried on the hotplate before cutting into shapes of a CD and attached on a DVD drive using double-sided tape. Laser scribing was done at different reduction steps (from 1 to 5) to compare the efficiency of the reduction.

5.3.9.3. Laser scribing of PET drop-casted with GO

A 10 mg/mL GO was prepared. About 8-10 mL of GO was drop-casted onto the PET. The PET was dried on the hotplate. Laser scribing was done at different reduction steps (from 3 to 5) using a laser engraving machine to compare the efficiency of the reduction. Meanwhile, the functionality of the electrodes was compared between the reduction of all the three electrodes (working, counter and reference electrodes) and the reduction of working and counter electrodes only. The experiment was repeated with 5 mg/mL GO. When the reduction was completed, silver inks and dielectric inks were hand-drawn on the laser-scribed electrodes. The electrodes were dried in the drying oven for 20-30 min at 125 °C before subjecting to CV analysis.

5.3.9.4. Laser scribing of photographic paper and PET containing GO transferred from MF

A 5 mL of 0.5 mg/mL GO was filtered using MF with a pore size of 0.025 µm. The PET was treated with plasma cleaner for 8-10 min. GO on the MF was transferred onto photographic paper by a stamping method. The photographic paper was subjected to laser scribing using a laser engraving machine at 5-reduction steps. When the reduction was completed, silver inks and dielectric inks were hand-drawn on the laser-scribed electrodes. The electrodes were dried in the oven for 20-30 min at about 125 °C before subjecting to CV analysis with PBS supporting electrolyte and different concentrations of Fe^{2+}/Fe^{3+} redox probe. The experiment was repeated with 0.1 mg/mL GO. Lastly, the same experiment was repeated with the use of PET as the substrate instead of photographic paper.

5.3.10. Preparation of laser-scribed GO and GO-FA electrodes using laser DVD-burner with a 3-step process

Both the laser scribed GO and GO-FA electrodes were prepared using a DVD-burner laser with a 3-step process, following a modified protocol of Giacomelli *et al.* (2020)[179]. The

objectives of this work were to test the reproducibility of the as-prepared laser scribed GO and GO-FA electrodes and to determine the effect of the addition of FA on the electrodes, using CV, CA and DPV. For the preparation of the laser scribed GO electrodes, 10 mL of 0.1 mg/mL GO was filtered using MF with a pore size of 0.025 μm. Four different MFs were prepared. The MFs were attached on the DVD drive using double-sided tape. It was important to ensure no bubbles on the surface of the DVD drive, and the surface must be flat. The DVD drive was subjected to laser scribing at 5-reduction steps. When the reduction was completed, the reduced GO (rGO) was transferred from the MF onto PET using a hydraulic press. Next, silver inks and dielectric inks were added on the laser-scribed GO electrodes. The electrodes were dried in the drying oven for 20-30 min at 125 °C before subjecting to CV analysis with PBS and Fe^{2+}/Fe^{3+} redox probe. A 5 μL of 10 mg/mL FA was added onto the surface of the working electrodes and allowed to dry overnight. The same electrodes were subjected to CV with PBS. The excess or unattached FA on the working electrodes were washed with PBS, before subjecting to another CV analysis with PBS. This serves as a proof-of-concept of the effects of addition of FA onto the GO platform.

5.3.10.1. Optimisation of preparation of laser-scribed GO and GO-FA electrodes

For optimisation of the preparation of laser-scribed GO-FA electrodes, four pieces of MFs were filtered with 10 mL solution containing 1 mg of GO and 10 mg of FA. The MFs were attached on the DVD drive using double-sided tape. The DVD was subjected to laser scribing at 5-reduction steps. When the reduction was completed, the rGO and (reduced) FA were transferred from the MF onto PET using a hydraulic press. Next, the silver inks and dielectric inks were hand-drawn on the laser-scribed electrodes. The electrodes were dried in the drying oven before subjecting to CV analysis with PBS.

In this work, the reproducibility of the GO electrodes (10 mL, 0.1 mg/mL) was studied, followed by preparation of laser scribed GO-FA electrodes (1 mg/mL of GO and 10 mg of FA in 10 mL).

5.3.10.2. Preparation of laser-scribed GO-FA electrodes using filtration by layers

The mixture used in the preparation of laser scribed GO-FA electrodes was composed of GO and FA. With this, four pieces of FMs were filtered by layers with different ratios of GO:FA. The final mixture of each MF contained 1 mg of GO with 10 mg of FA in 10 mL. The design of each filtration by layers is as follows.

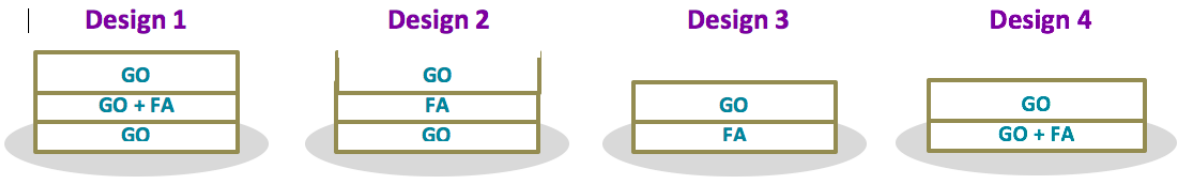

5.3.10.3. Preparation of laser-scribed GO-FA electrodes using different concentration ratios of GO:FA

Laser scribed GO-FA electrodes were prepared using different concentration ratios of GO:FA. PET was used as the substrate. Different concentration ratios of GA:FA were tested, including 1:5, 1:1, 2:1 and 8:1. The concentration of GO used was fixed at 0.1 mg/mL in 10 mL. After confirming the reproducibility of each batch of electrodes, the electrochemical behaviours of the electrodes were studied using CV and DPV. The laser scribed GO-FA electrodes with ratio GO:FA of 1:1 and 8:1 were selected for further electrochemical studies with the use of FR as analyte.

5.3.10.4. Effect of addition of FR of laser scribed GO and GO-FA electrodes

Functional laser scribed GO electrodes and GO-FA electrodes from the previous experiments (with ratio GO:FA of 1:1 and 8:1) were prepared. DPV of all the selected

electrodes were measured and recorded. The working electrode of each electrode was modified with 3 µL of 2 µg/mL FR. The electrodes were air-dried before washing the un-bound FR on working electrodes with PBS. The electrodes were air-dried before CV and DPV analysis. The final concentration of Fe^{2+}/Fe^{3+} redox probe was 1.57 mM, which composed of 50 µL of PBS at pH 7.4 and 20 µL of 5.5 mM Fe^{2+}/Fe^{3+} in 0.01 M KCl. The results were recorded and analysed.

The experiments were repeated with different concentrations of FR (7.6, 38 and 190 ng/mL). Functional laser scribed GO electrodes and GO-FA electrodes (with ratio GO:FA of 1:1) were prepared. The concentration of GO and FA used in preparing the GO-FA mixture were both 0.1 mg/mL, with the final volume of 10 mL prepared for each MF. The working electrode was modified with 3 µL of different concentrations of FR. Five replicates were prepared for each concentration of FR. The un-bound FR was removed from working electrodes after 5 min by washing the working electrodes twice with 20 µL of PBS before air-drying and subjecting to CV and DPV analysis.

The experiments were repeated with extra precaution steps such as all the selected electrodes have almost similar area of the working electrode and net basal current, human and pipetting errors were reduced to a minimum, the location of the electrode on MF during laser scribing was recorded, *etc*.

In addition, laser scribed GO, and GO-FA electrodes were prepared for modification with 3 µL of 7.6 ng/mL FR. The electrodes were subjected to electrochemical impedance spectroscopy (EIS) study to confirm the interaction between FR and FA on the laser scribed GO-FA electrodes. As displayed in Figure 5.1B, one complete laser reduction using DVD burner produced 24 electrodes. The laser reduction was incomplete sometimes, with only 58 % or about 14 electrodes were completely reduced per DVD, per reduction. Therefore, the reproducibility of functional laser scribed GO, and GO-FA electrodes required optimisation. Hence, an experiment to study the correlation between

the position of the electrodes on the DVD during laser scribing and net basal current of the electrodes was conducted. The positions of the electrodes on the DVD during laser scribing were recorded. CV and DPV analysis were carried out. The final concentration of Fe^{2+}/Fe^{3+} redox probe was recorded as 1.57 mM. The functionality, reproducibility and basal current of the as-synthesised electrodes were checked and evaluated. Only the electrodes that gave CV/DPV signal were chosen for the next stage of the investigation. An experiment to investigate the interaction between FR and Fe^{2+}/Fe^{3+} redox probe was conducted using SPEs. The functionality of SPEs was confirmed with PBS and Fe^{2+}/Fe^{3+} redox probe. The surface of the SPEs was cleaned with deionised water and allowed to dry before use. DPV was conducted with PBS and Fe^{2+}/Fe^{3+} redox probe with the final concentration of 1.57 mM. Then, 3 µL of 7.6 ng/mL FR was added onto the SPEs. In this case, the final concentration of Fe^{2+}/Fe^{3+} redox probe was 1.51 mM. DPV of the SPEs was checked and recorded.

5.3.11. Investigation on the sensitivity of the laser-scribed GO electrodes, in comparison to SPEs

SPEs and laser-scribed GO electrodes were prepared. All the electrodes were subjected to analysis in PBS buffer. This was to ensure the electrodes were functional and gave a response to CV analysis. The selected electrodes were subjected to electrochemical studies, using CV and DPV, with the concentrations of Fe^{2+}/Fe^{3+} redox probe as 0, 0.50, 0.92, 1.27, 1.57 and 1.83 mM. Three replicates of electrodes were prepared for testing with each concentration of the redox probe.

5.3.12. Effects of light exposure and laser scribing on FA

In preparation of laser-scribed GO-FA electrodes, it was important to ensure that the functionality of FA in the GO-FA mixture was not affected by exposure to light and laser scribing. Two preliminary experiments were conducted to investigate the effects of light exposure and laser scribing on FA. Briefly, 1 and 5 mg/mL FA were prepared in triplicates

and subjected to absorbance measurements using a microplate reader. Then, FA was exposed to DC regulated illuminator for 5 min before subjecting to absorbance measurements using a microplate reader.

In addition, two pieces of MFs were prepared, filtered with 10 mL of FA (1 mg/mL), and attached to a DVD. The DVD was then laser scribed at 5-reduction steps. The surface of the MFs was observed after each reduction.

5.3.13. XPS characterisation of the laser scribed GO and GO-FA electrodes

To analyse the surface chemistry of the laser scribed GO and GO-FA electrodes, the following samples were prepared and characterised using XPS.

i. Working electrode of laser scribed GO electrode
ii. Working electrode of laser scribed GO-FA electrode
iii. MF filtered with a mixture of GO-FA dissolved in PBS
iv. MF filtered with a mixture of GO-FA dissolved in deionised water

5.3.14. Electrochemical reversibility studies of Fe^{2+}/Fe^{3+} redox probe on SPEs, laser-scribed GO and GO-FA electrodes

The functionality of the electrodes was initially determined in PBS. Only the electrodes that gave CV response were selected. An SPE, laser-scribed GO and GO-FA electrode were chosen. Measurement of the CV signal was conducted in PBS and Fe^{2+}/Fe^{3+} redox probe, at the scan rate of 100 $mV.s^{-1}$. The final concentration of Fe^{2+}/Fe^{3+} redox probe was 1.57 mM. The measurement was repeated for 10 times, with an intermittent pause in between each scan. The anodic peak potential and peak current for each CV scans were recorded and compared. The CV measurement was repeated for another 10 continuous scans. This was to confirm if the differences in the peak potential and peak current between each scan were significant. Next, the CV measurement was repeated with three continuous scans for each electrode, at five different scan rates (20, 80, 150,

230 and 300 $mV.s^{-1}$). Only the anodic peak potential and peak current at the 3rd CV scan were recorded.

5.3.15. CV studies of SPEs, laser-scribed GO and GO-FA electrodes with the use of $Ru(NH_3)_6Cl_3$ as a redox probe

Three SPEs, six laser-scribed GO electrodes and six laser-scribed GO-FA electrodes were chosen. The functionality, cathodic peak potential and peak current of the electrodes were checked and recorded. The surface of the working electrodes was modified with 3 µL of 7.6 ng/mL FR. After 5 min, FR was removed from the surface of working electrodes and washed with 20 µL of PBS, twice. The electrochemical performance was determined using CV analysis once the surface was fully dried. A 50 µL of 1 mM $Ru(NH_3)_6Cl_3$ was used as a redox probe. As a control, 3 µL of 7.6 ng/mL FR was added directly onto the drop of 50 µL of 1 mM of $Ru(NH_3)_6Cl_3$ on the SPEs. The CV signal was checked and recorded.

5.3.16. Reproducibility of laser scribed GO-FA electrodes and its effect on the addition of FR in $Ru(NH_3)_6Cl_3$ redox probe

A 50 µL of 1 mM $Ru(NH_3)_6Cl_3$ was used as a redox probe in the electrochemical measurements. The functionality of the electrodes was first checked with PBS. Only the laser scribed GO-FA electrodes that gave CV response were selected. The initial CV, DPV and EIS signals of the electrodes were checked and recorded. All the electrodes were divided into four groups, with five electrodes in each group. Each group of electrodes were subjected to modification with different concentrations of FR, which were 0.1, 1.0, 10.0 and 40.0 ng/mL, respectively. The CV, DPV and EIS signals of the electrodes were checked and recorded after the surface of the electrodes has dried.

5.3.17. Modification on the surface of working electrodes of SPEs with polymers

Biocompatible conducting polymers, such as polyaniline, chitosan, PEG, *etc*., have a flexible chemical structure. These conducting polymers can be used as a matrix for entrapment of enzymes, where they can efficiently transfer electric charge produced in a biochemical reaction to an electronic circuit. Moreover, they can be deposited over definite areas of electrodes[185].

In this study, two different conducting polymers, PVA and PEG, were selected. The study aimed to investigate if the conducting polymers aid in the immobilisation and stabilisation of FA on the working electrodes of SPEs.

Before the experiments, the functionality of the SPEs was first checked in PBS. Only the SPEs that gave CV response were selected. The basal current for CV and DPV of the SPEs were measured and recorded. The SPEs with a relativity stable basal CV and DPV current were grouped and selected.

5.3.17.1. Modification on the surface of working electrodes of SPEs with PVA

A 3 % of PVA (30 mg/mL) was dissolved in deionised water at 90 °C for 2 h. Five different solutions, each with a final volume of 200 µL, were prepared as follows:

i. PVA only
ii. The ratio of PVA:FA as 1:1 in PBS
iii. The ratio of PVA:FA as 1:1 in deionised water
iv. FA dissolved in PBS
v. FA dissolved in deionised water

Briefly, 3 µL of each solution was loaded onto the working electrode of the SPE. Two replicates of the SPEs were prepared for each solution. Then, the SPEs were air-dried. The surface of the SPEs was washed gently with deionised water and dried using N_2 gas.

CV and DPV of the SPEs were measured and recorded, with the use of $Ru(NH_3)_6Cl_3$ as a redox probe.

5.3.17.2. Modification on the surface of working electrodes of SPEs with PEG

The modification was done following a modified protocol of Xu *et al*. (2012)[186]. A 2 mg/mL PEG was prepared using deionised water. Three different groups of SPEs were labelled, as follows:

i. PEG only
ii. The ratio of PEG:FA as 20:1 in PBS
iii. The ratio of PEG:FA as 20:1 in deionised water

Briefly, 5 µL of 2 mg/mL PEG was loaded onto the working electrode of the SPEs. Triplicates of the SPEs were prepared for each group. The SPEs were incubated at 4 °C overnight to allow passive adsorption of the PEG onto the surface of the SPEs. The surface of the SPEs was washed gently using deionised water and dried using N_2 gas. Then, 3 µL of FA was added. The SPEs were air-dried. The surface of the SPEs was washed gently with deionised water and dried using N_2 gas. DPV of the SPEs was measured and recorded, with the use of $Ru(NH_3)_6Cl_3$ as a redox probe.

5.4. Results and Discussion

5.4.1. Covalent conjugation of FA onto BSA/AuNCs

Hemmateenajad *et al.* (2014)[137] reported the effect of the addition of FA onto BSA/AuNCs using a titration method. It was found that FA quenched the fluorescence of BSA/AuNCs with a linear range of 0.12-33.12 µg/mL and detection limit of 18.3 ng/mL. It was speculated that the fluorescence quenching was due to cross-linking of the BSA molecules, as BSA acts as a stabiliser in BSA/AuNCs. The interaction of BSA and Au atoms was disrupted upon addition of FA.

As displayed in Figure 5.2, the higher the concentrations of FA, the higher the fluorescence quenching of BSA/AuNCs. It was also found that direct addition of FA onto

BSA/AuNCs, without covalent bonding, using EDC/NHS linker, resulted in 87 % fluorescence quenching of BSA/AuNCs. On the other hand, the mixture of the linker EDC/NHS and BSA/AuNCs, without the addition of FA, led to 91-94 % fluorescence quenching of BSA/AuNCs. This showed that the use of EDC/NHS linker affected the fluorescence intensity of BSA/AuNCs. Thus, it was misleading to claim that the fluorescence quenching of BSA/AuNCs was due to successful conjugation of FA onto BSA/AuNCs.

It was suspected that the surface chemistry of BSA/AuNCs made it more susceptible to any functionalisation. The Au oxidation state could affect the QY and fluorescence stability of BSA/AuNCs. Another possible mechanism contributing to the fluorescence quenching of BSA/AuNCs could be due to protein unfolding or alterations in the protein secondary structures upon FA complexation. FA interacts with BSA *via* both hydrophobic and hydrophilic contacts. BSA might act as a carrier protein for FA[68]. The present work also emphasised the importance of purification from the excess of FA, while purification has little effect (1.6 %) on pure BSA/AuNCs. This further confirmed the synthesis protocol since most of the BSA reacted with AuNCs.

In addition, it was found that the addition of FR could not recover the fluorescence intensity of the quenched FA-BSA/AuNCs. This could be due to low concentrations of FR (1 and 2 µg/mL) were selected, which is not sufficient to perturb the interaction of FA with BSA/AuNCs.

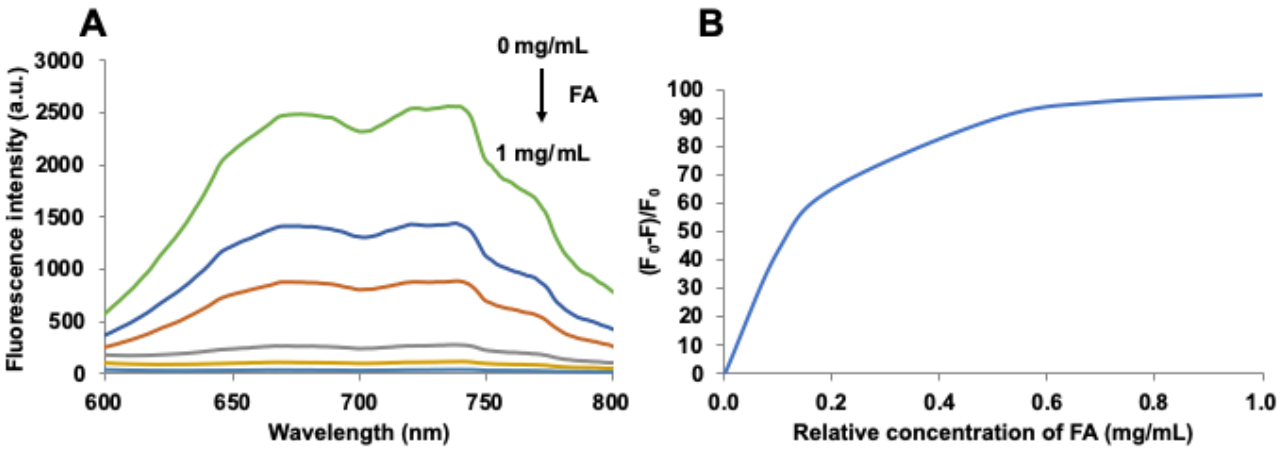

Figure 5.2 Effect of addition of FA onto BSA/AuNCs. (A) Fluorescence intensity of BSA/AuNCs at λ_{em}= 365 nm. The relative concentrations of FA were 0.1, 0.2, 0.5, 0.7 and 1.0 mg/mL. (B) Fluorescence quenching values of BSA/AuNCs by varying the concentrations of FA.

5.4.2. Loading of BSA/AuNCs onto different GO platforms

The wells were successfully wax-printed on nitrocellulose paper strip (as shown in Figure 5.3A). As a proof-of-concept, Figure 5.3B and 5.3C confirmed the reproducibility of the GO platform, with immediate fluorescence quenching observed when the BSA/AuNCs interacted with GO. The fluorescence intensity of BSA/AuNCs was higher when the images were taken immediately, than after 3 h. This property is promising for biosensor applications changes are revealed in the shortest amount of time, after detection. In addition, the response was amount dependent as increased fluorescence quenching was observed with increased concentration of GO. From Figure 5.3C, 1 mg/mL GO appeared to be the optimal concentration for fluorescence quenching of BSA/AuNCs.

However, the deposition of different concentrations of GO on paper strips was not homogeneous, as shown in Figure 5.3A. Uneven white spots and coffee ring effects were clearly observed in the wells. Different concentrations of GO were also deposited on different substrates, such as glass fibre, photographic paper, plastic (Figure 5.4A and

5.4B) and nitrocellulose membrane (Figure 5.4C), to create a homogeneous and functional GO platform.

Different methods were devised to allow more homogeneous loading of GO onto the paper-based platforms, including sonication of GO before use, resuspension of GO upon loading onto paper-strip, placed the paper strip on top of thermomixer for gentle deposition, *etc*. However, it was observed that the deposition of GO remained non-homogeneous in most of the substrates. It was suggested that pretreatment of the nitrocellulose paper strip using plasma cleaner and addition of surfactant might reduce the coffee ring effects. In short, more efforts were needed to create a homogeneous GO platform.

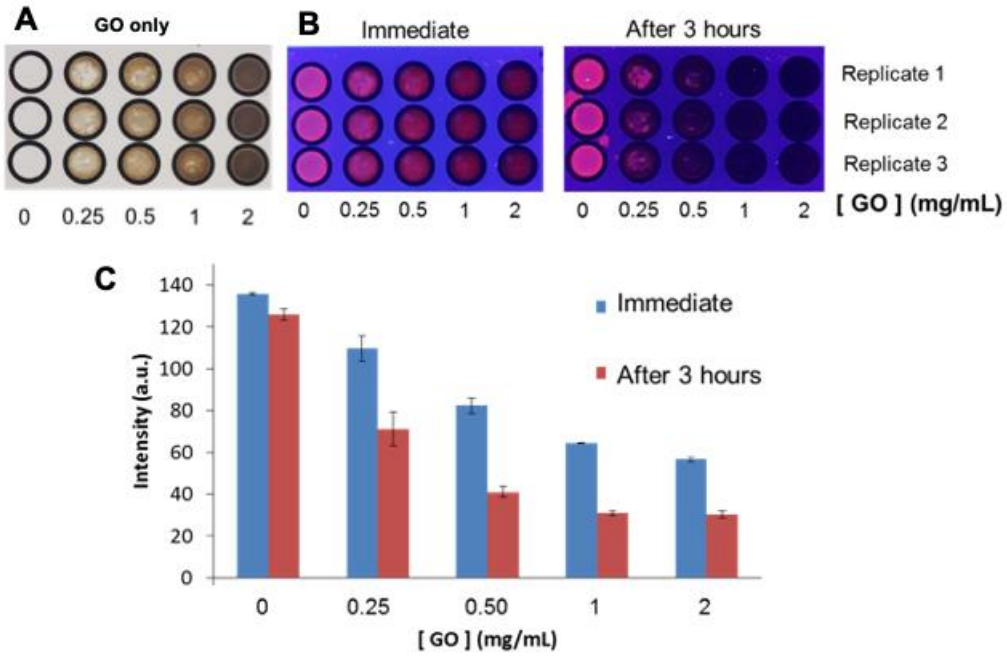

Figure 5.3 Loading of BSA/AuNCs onto nitrocellulose paper strip. (A) Paper strip loaded with different concentrations of GO. (B) Paper strip loaded with different concentrations of GO, immediately (left) and after 3 h (right) loaded with the same concentration of BSA/AuNCs, when exposed under UV light. (C) Fluorescence intensity of the BSA/AuNCs after loading onto different concentrations of GO on a paper strip.

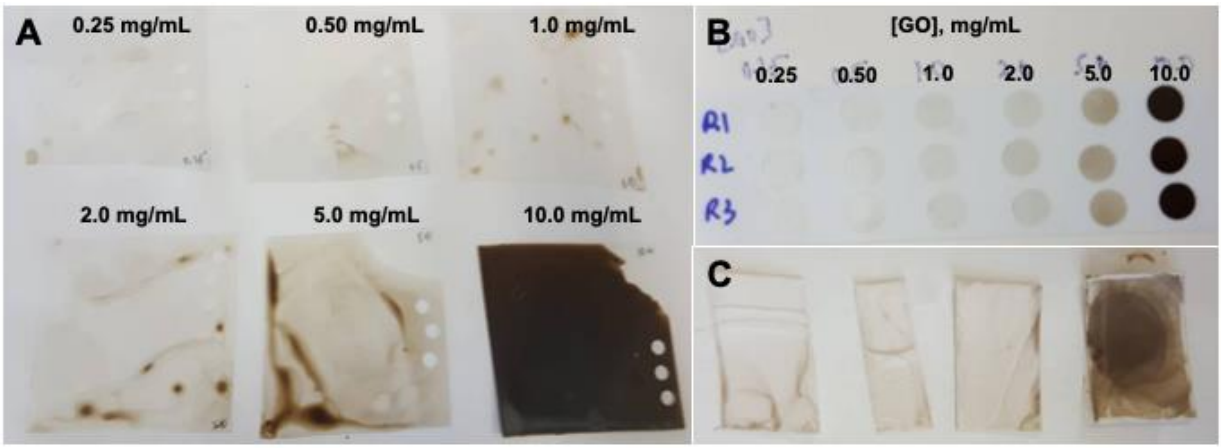

Figure 5.4 Different concentrations of GO loaded onto different platforms. (A) Plastic sheets loaded with different concentrations of GO. (B) Paper-strip designed with different concentrations of GO loaded on plastic-based wells, from 0.25-10.0 mg/mL GO, with three replicates. (C) Different concentrations of GO loaded onto a nitrocellulose-based platform.

5.4.3. "Drop and dry" method of GO, rGO and FA on the SPEs

Depending on the degree of oxidation, GO shows low electrical conductivity causing an insulating or semi-conducting behaviour while rGO shows excellent electrical conductivity. The repulsion of ferri/ferrocyanide ions with negatively charged functional groups of GO sheets could be another possible factor for the decrease in the DPV signals. The electrical properties of GO can be tuned by changing the concentrations of oxygen containing compounds.

In Figure 5.5, DPV analysis showed that after modification of working electrodes of the SPEs with GO or rGO, the current obtained for all the electrodes were higher than the un-modified surface (bare SPEs). In addition, the higher the concentration of GO loaded onto the working electrodes, the higher the current and basal DPV signals obtained. This could be due to improved kinetics of the Fe^{2+}/Fe^{3+} redox probe at the SPEs at higher concentrations of GO, which decreased the charge transfer resistance, accelerated

electron transfer, lower phase shift and smaller impedance of the system[187]. This suggested that the mechanism of the Fe^{2+}/Fe^{3+} redox probe required further studies.

On the other hand, the current obtained with 0.1 mg/mL rGO was lower than 0.2 mg/mL GO but higher than bare SPEs. This could be due to the lower concentration of rGO used. Another possible reason is that the reduction of the GO flakes was incomplete and not able to restore the π-conjugation in the graphitic structure of rGO[188,189]. Moreover, the presence of stacked graphene flakes resulted in significant flake-to-flake resistance in the rGO used[190].

As shown in Figure 5.6A and 5.6B, CV and DPV response were observed for the SPEs modified with FA, except for the SPEs modified with 5.0 mg/mL FA. It was suspected that 5.0 mg/mL was too concentrated for modification on the electrodes. It was tricky to prepare a homogeneous mixture of FA on the surface of working electrodes. FA was found to detach easily from the working electrodes after the washing step. The current obtained before and after modification of FA on SPEs were almost similar (about 3×10^6 A). This further substantiated that FA attached on the working electrodes was dissolved by PBS supporting electrolyte during electrochemical measurements.

Therefore, it can be concluded that "drop & dry" method is not ideal to be employed in studying the electrochemical properties of the materials. This is mainly because the materials on the surface of the electrodes will easily dissolve in supporting electrolytes and be washed away. For future work, the modification of SPEs can be done *via* electrospinning of GO with the hydrophilic polymers, such as PVA, to explore its potential application in biosensing.

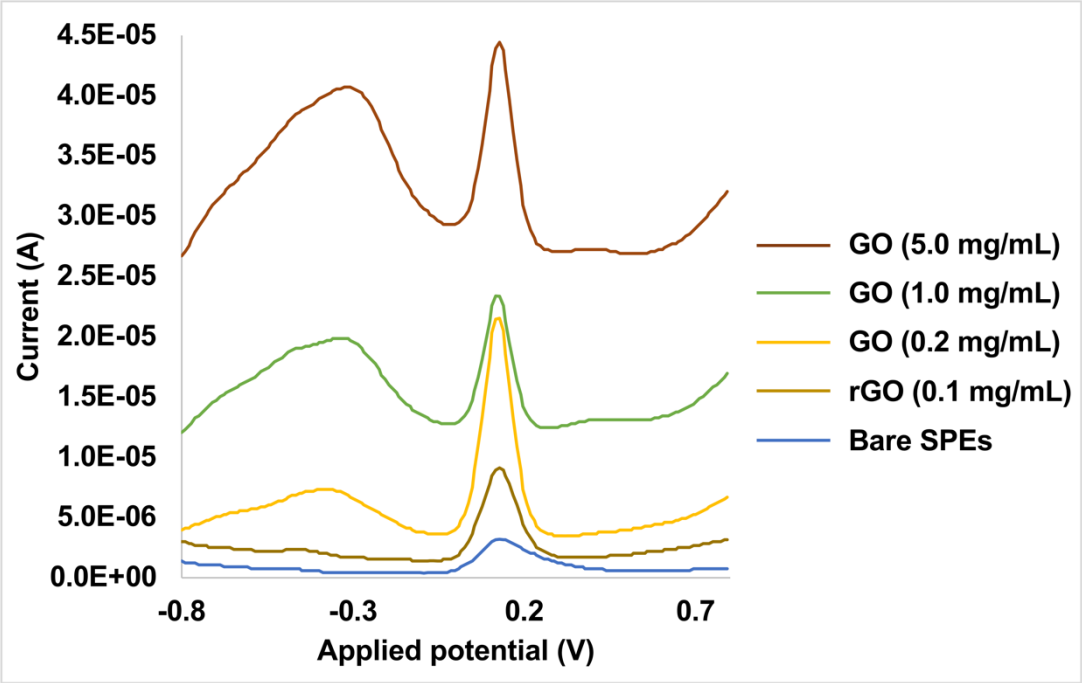

Figure 5.5 "Drop and dry" method of GO and rGO onto the SPEs. DPV recorded after addition of GO or rGO onto the working electrodes of SPEs, in PBS and Fe^{2+}/Fe^{3+} redox probe. Each data shown is an average of two replicates of SPEs.

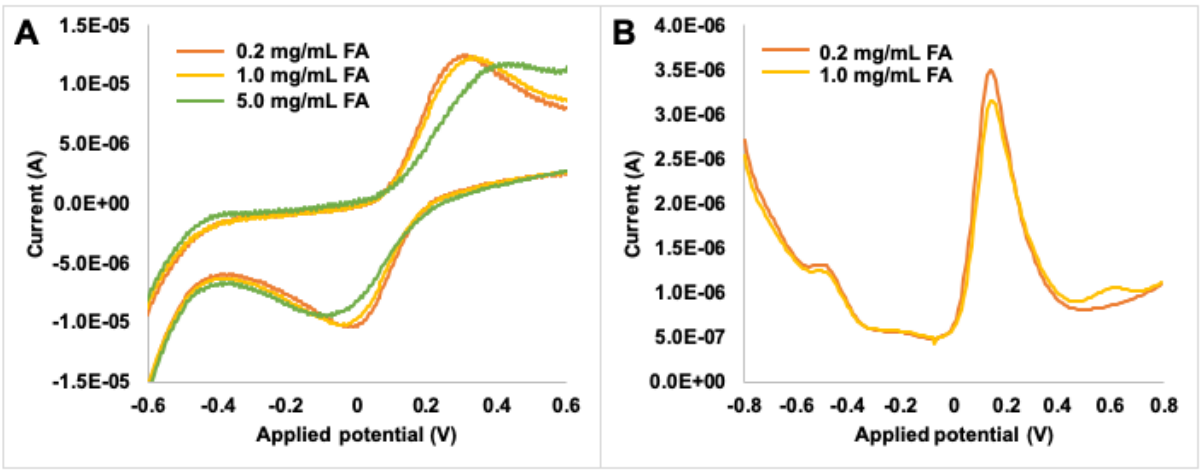

Figure 5.6 Effects of the addition of FA onto SPEs. (A) CV and (B) DPV of the SPEs, after modification with FA at 0.2, 1.0 and 5.0 mg/mL, in Fe^{2+}/Fe^{3+} redox probe. The data shown is an average of two replicates of SPEs.

5.4.4. Preparation of laser-scribed graphene electrodes using direct laser DVD-burner and laser engraving machine

Four different approaches were taken to determine the ideal method and substrate for the fabrication of laser-scribed graphene electrodes.

5.4.4.1. Laser scribing of MF loaded with the mixture of GO and FA on the DVD drive

As shown in Figure 5.7A, it was observed that the working electrodes on the MF were not fully reduced. Besides, some sections of the GO layer was detached from the MF. This could be due to the uneven surface of the MF upon attaching on the DVD drive, which affected the laser focus of the lens on the DVD drive.

5.4.4.2. Laser scribing of PET drop-casted with the mixture of GO and FA on the DVD drive

As displayed in Figure 5.7B, it was challenging to achieve a homogeneous distribution of the mixture using the drop-casting method. The reduction (even by 5 steps) cannot fully reduce the GO. The reproducibility of electrodes using this approach was very low; it was difficult to recover any electrodes after laser scribing.

5.4.4.3. Laser scribing of PET drop-casted with GO

As highlighted in the previous approach, it was hard to achieve a homogeneous distribution of the mixture using the drop-casting method. It was found that reduction by 5 steps was suitable for complete reduction of GO. The electrodes prepared with 5 reduction steps had the lowest resistance, as compared to the electrodes prepared with 3-4 reduction steps. However, no oxidation/reduction peak was observed from all the as-prepared laser-scribed electrodes (as shown in Figure 5.7C), during CV analysis with Fe^{2+}/Fe^{3+} redox probe. No obvious differences were observed between the reduction of all the three electrodes (working, counter and reference electrodes) and the reduction of working and counter electrodes only, during CV analysis

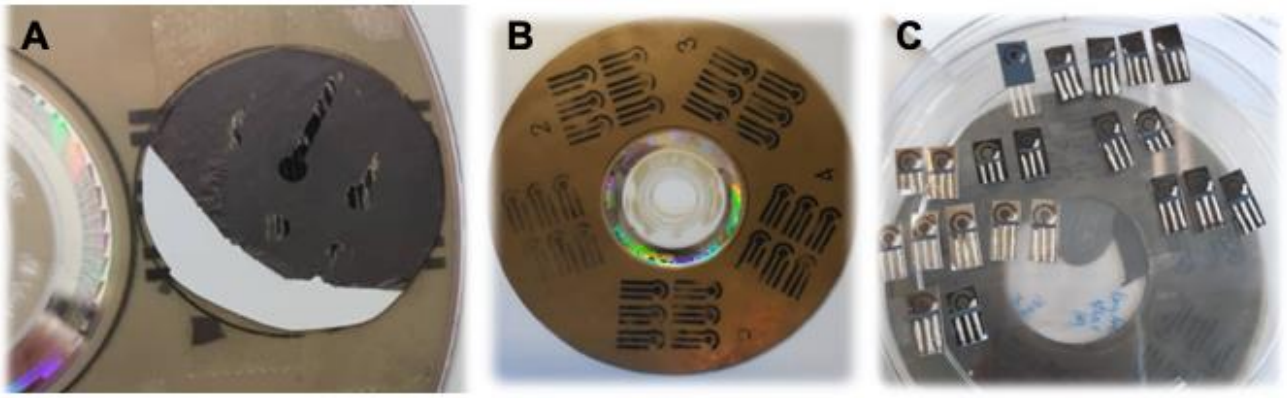

Figure 5.7 Laser-scribed GO electrodes prepared using direct laser DVD-burner and laser engraving machine. (A) Laser scribing of MF loaded with GO and FA on the DVD drive. (B) Laser scribing of PET drop-casted with GO and FA on the DVD drive. (C) Laser scribing of PET drop-casted with GO.

5.4.4.4. Laser scribing of photographic paper and PET containing GO transferred from MF

For this approach, no oxidation/reduction peak was observed during CV measurement with Fe^{2+}/Fe^{3+} redox probe, from all the as-prepared laser-scribed electrodes, regardless of the use of photographic paper or PET as substrate. The current obtained during the measurements was low, with background noise observed as well. The transfer of GO from MF to the substrate was easier without pretreatment of the substrate with a plasma cleaner. GO from two different companies (Angstrom Materials and Graphenea) were compared, but still, no oxidation/reduction peak was observed during CV analysis. In conclusion, it was confirmed to be problems with the as-prepared laser scribed electrodes since obvious peaks were observed when tested with SPEs. This technique warrants further investigations.

5.4.5. Preparation of laser-scribed GO and GO-FA electrodes using laser DVD-burner with a 3-step process

Laser DVD-burner with a 3-step process was used for the preparation of laser scribed GO and GO-FA electrodes. From Figure 5.8A-C, it was observed that both the laser scribed FA and GO-FA electrodes showed an oxidation peak near the potential window. The reproducibility of the electrodes can be further improved as currently, the reproducibility of functional electrodes in a batch was around 50 %. As shown in Figure 5.8B-C, the signal/current was reduced after the addition of FA, as well as after washing the excess or unattached FA on the working electrodes with PBS. It can be deduced that some FA remained on the surface of the working electrodes even after washing the excess FA with PBS. The shoulders observed in the CV curve in Figure 5.8B could be due to the catalytic oxidation of water, or the PBS was contaminated. For future work, it is important to fabricate more electrodes to confirm the reproducibility and to determine the influence of FA on electrochemical signals in the Fe^{2+}/Fe^{3+} redox probe.

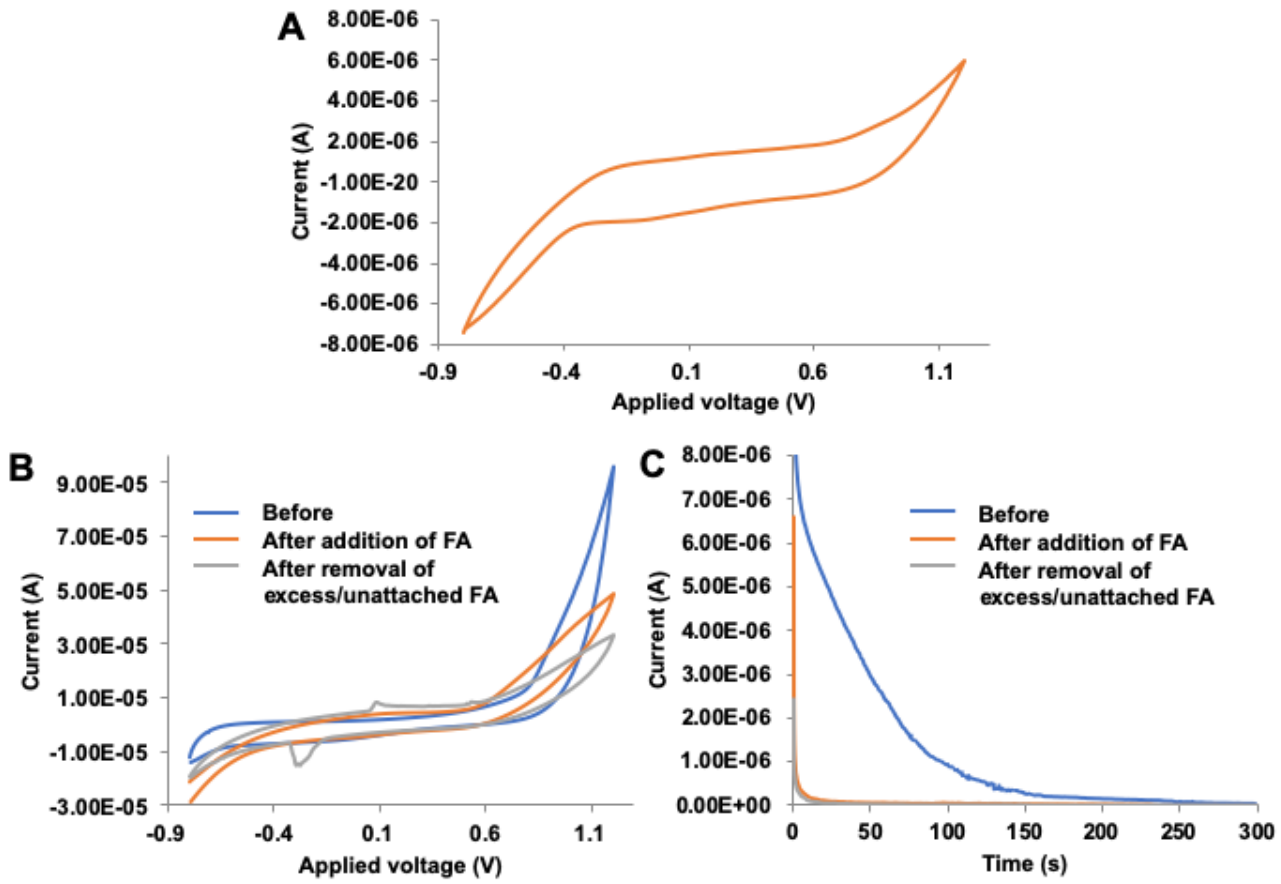

Figure 5.8 Laser-scribed GO and GO-FA electrodes prepared using laser DVD-burner with a 3-step process. (A) CV recorded with laser-scribed GO-FA electrode in 50 µL of PBS. (B) CV and (C) CA recorded with laser-scribed GO electrode before (blue line), after addition of FA (orange line) and after removal of excess/unattached FA, in 50 µL of PBS.

5.4.5.1. Optimisation of preparation of laser-scribed GO and GO-FA electrodes

In this work, 1 mg of GO and 10 mg of FA were dissolved in 10 mL of deionised water. The mixture was subjected to 15 min bath sonication to ensure GO and FA were mixed well. However, it was observed that the rGO surface layers were brittle when removing the MF from the DVD drive after laser scribing, as displayed in Figure 5.9A-B. This could be due to the low concentration of GO, which resulted in thin layers and susceptible to damage.

The experiment was repeated with 4 mg of GO with 10 mg of FA in 10 mL of deionised water. The filtration took nearly 2 h to complete, suspected because of bath sonication. The effects of sonication were compared (samples with and without sonication) with the use of laser scribed GO-FA electrodes prepared using 1 mg of GO with 10 mg of FA in 10 mL.

Although bath sonication helped in the mixing of GO and FA, it greatly slowed the rate of filtration. This was because some of the water molecules evaporated during sonication, making the mixture more concentrated or less volatile. Most importantly, no acceptable CV peaks were observed from the as-prepared laser scribed GO-FA electrodes. Meanwhile, the reproducibility rate of functional laser scribed GO electrodes (with acceptable CV response peaks, as shown in Figure 5.9C) was about 66.7 %.

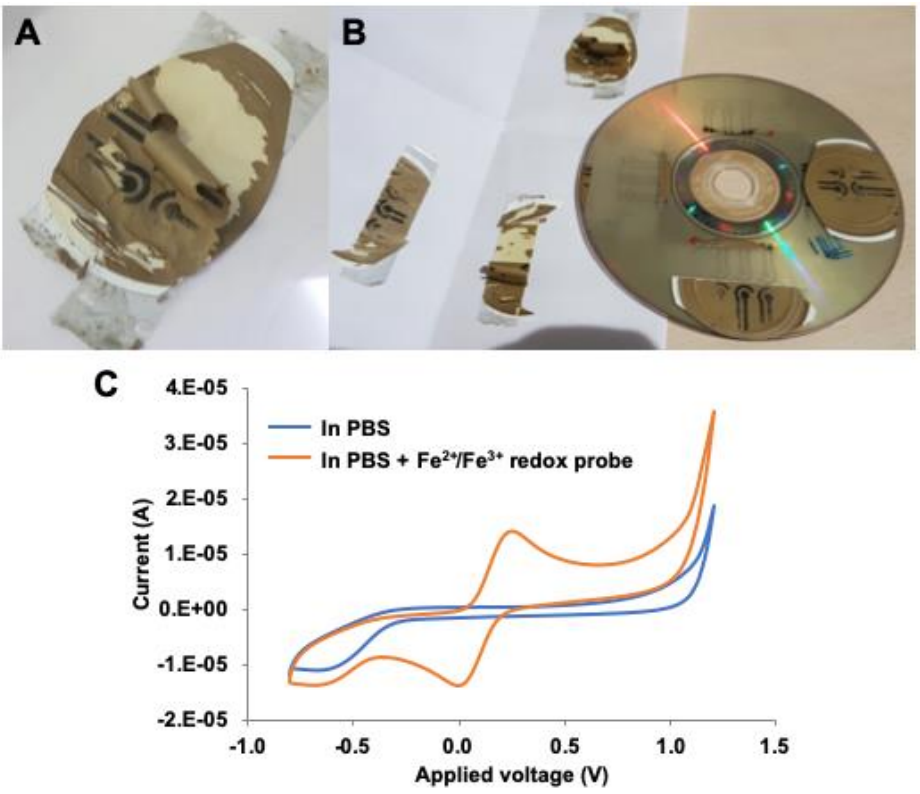

Figure 5.9 Laser-scribed GO and GO-FA electrodes preparation using laser DVD-burner with a 3-step process. (A, B) The rGO surface layers were brittle when trying to remove the MF from the DVD drive after laser scribing. (C) CV recorded with laser scribed GO

electrode (prepared with 10 mL of 0.4 mg/mL GO) in PBS (blue curve) and 1.57 mM Fe^{2+}/Fe^{3+} redox probe (orange curve).

5.4.5.2. Preparation of laser-scribed GO-FA electrodes using filtration by layers

The laser scribed GO-FA electrodes were prepared using filtration of the GO-FA mixture by layers. The designs were as described in the methodology section. For the laser scribed GO-FA electrodes prepared with Design 1, the bottom layer was too thin; therefore, the surface layers on the MF were easily broken when removed from the DVD drive. Each filtration took about 18 min. For the laser scribed GO-FA electrodes prepared with Design 2, each filtration took about 30 min. For the laser scribed GO-FA electrodes prepared with Design 3, it was hard to achieve a homogeneous surface layer. Each filtration took about 13 min. Whereas for the laser scribed GO-FA electrodes prepared with Design 4, at first, it was hard to achieve a homogeneous surface area during the filtration. However, the surface homogeneity was improved with the addition of more layers before the previous layer was fully dried up.

Generally, Design 4 was the most preferred. Each filtration took about 13 min. Nevertheless, it was found that the reduction was not completely penetrating to the bottom layer of the MF (incomplete reduction) for most of the as-prepared laser scribed GO-FA electrodes, as shown in Figure 5.10. No obvious CV peaks were observed for most of the as-prepared laser scribed GO-FA electrodes.

Figure 5.10 MF made up of different filtration layers using Design 4. (A) Bottom layer was composed of 4 mL of GO and 2 mL of FA mixture, while the top layer was composed of 4 mL of GO. (B) Bottom layer was composed of 2 mL of GO and 2 mL of FA mixture, while the top layer was composed of 6 mL of GO. The final concentration is 1 mg/mL FA and 0.1 mg/mL GO.

In conclusion, it can be deduced that the preparation of laser scribed GO-FA electrodes using filtration by layers was not helpful in getting an electrochemical signal. This can be justified by the following reasons: hard to achieve homogeneity on the MF's surface, incomplete laser reduction, MF surface was broken easily during removal from the DVD drive, only the top layer of the rGO and (reduced) FA were transferred onto PET substrate, low reproducibility of the functional electrodes, long hours of filtration for some samples and sometimes the DVD laser has a problem in precise focusing and laser reduction.

For future work, different concentration ratios of GO:FA can be tested on both PET and nitrocellulose membrane. The direct filtration method for GO-FA mixture and filtration by layers method can be studied with the use of nitrocellulose membrane as the substrate instead of using PET. It is also important to use SPEs to compare the results obtained from PET and nitrocellulose membrane. The reproducibility of the laser scribed GO electrodes on the nitrocellulose membrane is important for the preparation of

functional electrodes. The thickness of the transferred GO with FA layer can be determined using atomic force microscopy.

5.4.5.3. Preparation of laser-scribed GO-FA electrodes using different concentration ratios of GO:FA

Laser scribed GO-FA electrodes prepared using different concentration ratios of GO:FA were electrochemically studied. The results were presented in Figure 5.11. The reproducibility of the functional laser scribed GO-FA electrodes (getting CV response in PBS) was determined and as follows:

- Ratio of GO:FA = 1:5 = 25.0 %
- Ratio of GO:FA = 1:1 = 75.0 %
- Ratio of GO:FA = 2:1 = 58.3 %
- Ratio of GO:FA = 8:1 = 91.7 %

The reproducibility of the laser scribed GO-FA electrodes with the concentration ratio of GO:FA as 8:1 was better than electrodes with the concentration ratio of GO:FA as 1:1. Generally, from CV (Figure 5.11A, Figure 5.11C) and DPV (Figure 5.11B, Figure 5.11D), the current obtained for electrodes with the concentration ratio of GO:FA as 8:1 was higher than the current obtained for electrodes with the concentration ratio of GO:FA as 1:1.

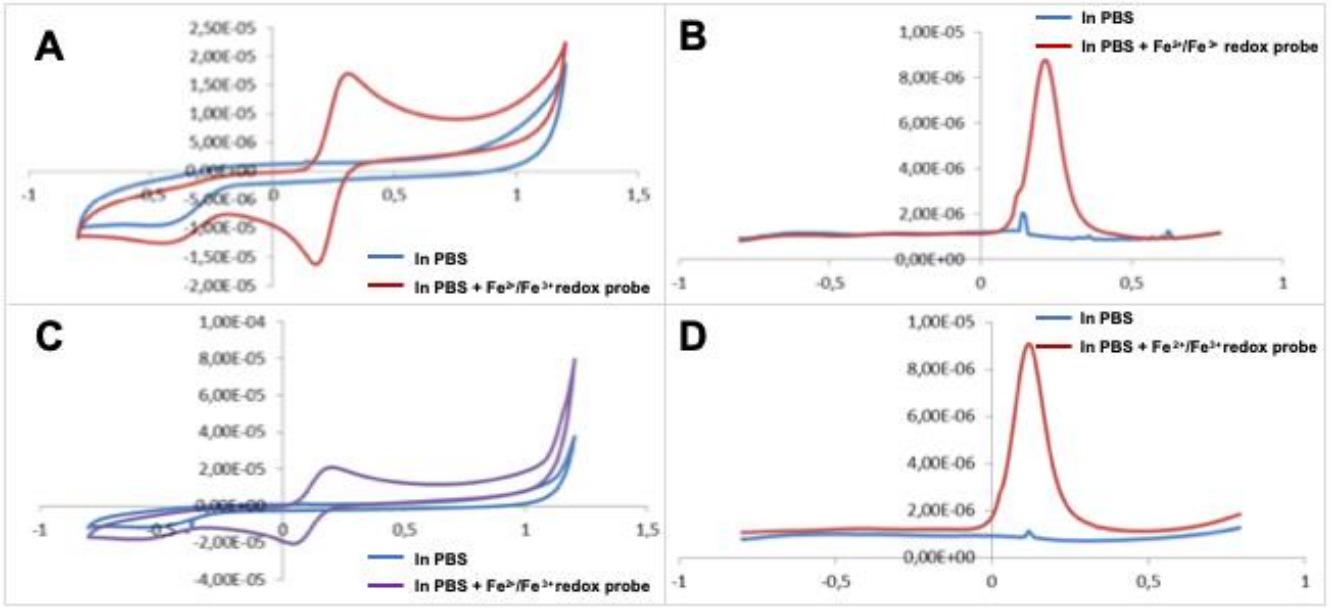

Figure 5.11 Electrochemical studies of laser scribed GO-FA electrodes prepared using different concentration ratios of GO:FA. (A) CV and (B) DPV recorded for electrodes with a concentration ratio of GO:FA as 1:1. (C) CV and (D) DPV recorded for electrodes with a concentration ratio of GO:FA as 8:1. For all the graphs, y-axis= current (A); x-axis= applied voltage (V).

5.4.6. Effect of addition of FR of laser scribed GO and GO-FA electrodes

The results obtained after modification of laser scribed GO and GO-FA electrodes with 3 µL of 2 µg/mL FR were recorded and analysed. The current in all the electrodes decreased after modification with FR. The basal net current in laser-scribed GO-FA electrodes was higher than laser-scribed GO electrodes.

After addition of FR, the decrease in current in laser-scribed GO electrodes was more obvious than laser-scribed GO-FA electrodes with a concentration ratio of GO:FA as 1:1 (as shown in Table 3B). The higher sensitivity and conductivity of laser-scribed GO electrodes could be due to the presence of a higher concentration of rGO (as laser scribing reduces GO to rGO) as compared to the concentration of rGO in laser-scribed GO-FA electrodes.

As shown in Table 3B, the decrease in the current of laser-scribed GO-FA electrodes with a concentration ratio of GO:FA as 8:1 was higher than electrodes with a concentration ratio of GO:FA as 1:1. This was due to the higher proportion of rGO in laser-scribed GO-FA electrodes with a concentration ratio of GO:FA= 8:1, which made the electrodes more conductive and sensitive. However, considering the potential application of laser-scribed GO-FA electrodes for sensing of FR, laser-scribed GO-FA electrodes with a concentration ratio of GO:FA as 1:1 were selected for a future experiment. This was mainly due to the higher proportion of FA in GO-FA mixture with a concentration ratio of GO:FA as 1:1 (50 %), which will be necessary for sensitive and selective sensing of FR.

The changes in the current response of the electrodes before and after washing the un-bound FR were compared. A decrease in current signal was observed after washing the un-bound FR with PBS. It was possible that FR (that was deposited on the electrodes) dissolved in PBS and was removed/washed after the electrochemical measurements. It was deduced that not all FR was attached on the surface of working electrodes, perhaps the concentration of FR used was too high or had reached the signal saturation point. Future work can focus on the determination of the detection range of FR by trying different concentrations of FR (lower than 2 µg/mL).

The experiment was repeated with different concentrations of FR (7.6, 38 and 190 ng/mL). It was found that the basal net current of laser scribed GO and GO-FA electrodes measured using DPV before any modification were almost similar, which was 10.0±3.4 µA and 12.0±5.2 µA, respectively.

The current response in the laser scribed GO, and GO-FA electrodes decreased after modification with different concentrations of FR. The average values of decrease in current in laser scribed GO, and GO-FA electrodes after modification with 7.6, 38 and 190 ng/mL FR were presented in Table 3A. It was hard to interpret the data since the results showed a high standard deviation (STD), even after the same experiment was

repeated with extra precaution steps. Generally, laser-scribed GO-FA electrodes showed a higher sensitivity towards FR than laser-scribed GO electrodes, especially at the lower range of concentration of FRs. Future work can be carried out on using a lower concentration of FR (less than 7.6 ng/mL) for modification on the electrodes.

Table 3 DPV results obtained after modification of laser scribed GO and GO-FA electrodes with FR.

A

	Concentrations of FRs (ng/mL)		
	7.6	38	190
Types of electrodes	Percentage of decrease in current (%)		
Laser-scribed GO Electrodes	35.4±18.6	54.1±31.4	47.7±13.8
Laser-scribed GO-FA Electrodes	48.1±28.5	27.5±4.9	34.9±18.3

B

After modification with 3 µL of 2 µg/mL FR		
Types of electrodes	Concentration ratio of GO:FA	Percentage of decrease in current (%)
Laser-scribed GO Electrodes	Nil	52.4±8.2
Laser-scribed GO-FA Electrodes	1:1	28.1±16.4
	8:1	57.1±11.5

EIS study was conducted on laser scribed GO and GO-FA electrodes after modification with 3 µL of 7.6 ng/mL FR. A few deductions were made following the EIS data shown in Figure 5.12. For laser scribed GO electrode, at least one chemical reaction occurred before any modification. This suggested the interaction between rGO and Fe^{2+}/Fe^{3+} redox probe. It was observed that the resistance of laser scribed GO electrode increased after modification with FR. It was suspected due to the interaction between FR and Fe^{2+}/Fe^{3+} redox probe. Another possibility was FR interacted with the rGO on laser scribed GO electrode.

For laser scribed GO-FA electrode, at least two chemical reactions occurred before modification with FR; while at least three chemical reactions occurred after modification with FR. The chemical reactions could be due to the interaction between rGO and reduced

FA with Fe^{2+}/Fe^{3+} redox probe, the interaction between reduced FA and FR, or the interaction of FR with Fe^{2+}/Fe^{3+} redox probe.

The resistance of the laser scribed GO-FA electrode was lower than the laser scribed GO electrode before modification with FR. In other words, FA may improve the electrical conductivity of the electrode.

As aforementioned, after modification with FR, one chemical reaction happened in laser scribed GO electrode; and at least three chemical reactions were happening in laser scribed GO-FA electrode. It was deduced that there was an interaction between rGO and Fe^{2+}/Fe^{3+} redox probe. However, it can be confirmed that there was no interaction between FR with rGO and Fe^{2+}/Fe^{3+} redox probe. This was because if there was any interaction, more than one chemical reaction would be observed. Meanwhile, the interaction of reduced FA and FR, as well as the interaction between rGO and reduced FA with the Fe^{2+}/Fe^{3+} redox probe were confirmed. Interaction between FR and Fe^{2+}/Fe^{3+} redox probe, which was initially suspected, now can be omitted.

In short, FA improved the electrical conductivity of the electrodes. Interaction of the FR with the reduced FA in the laser scribed GO-FA electrode was confirmed. The mechanism of the Fe^{2+}/Fe^{3+} redox probe required further studies. For example, it was important to identify if there was any interaction between the Fe^{2+}/Fe^{3+} redox probe with rGO, rGO and reduced FA as well as FR. It was also suspected that the Fe^{2+}/Fe^{3+} redox probe interacted with FA on the working electrodes *via* non-specific interaction or adsorption and affected the electrochemical response.

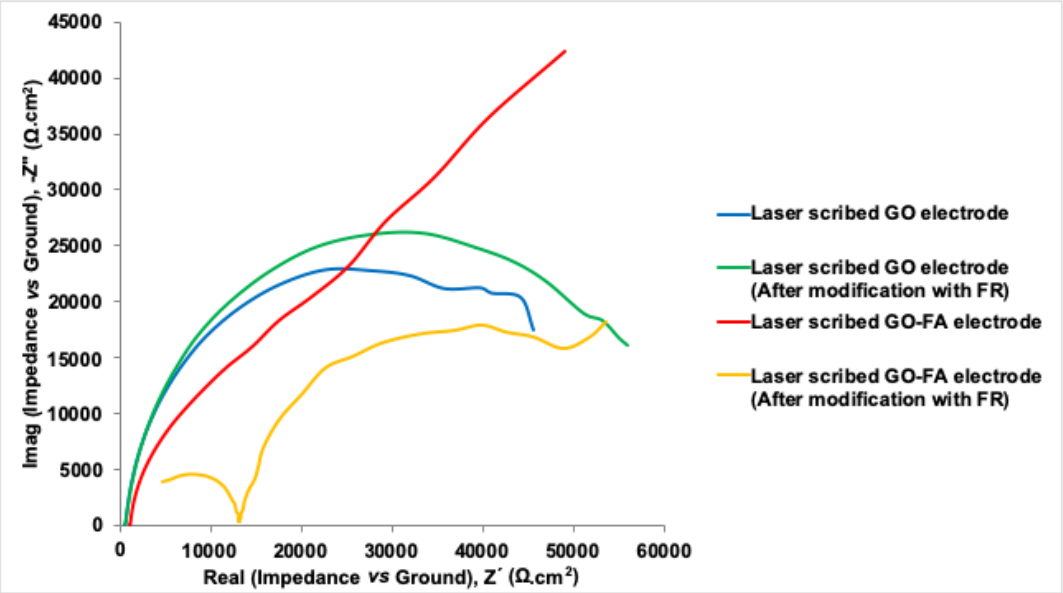

Figure 5.12 The EIS plots obtained in PBS, in the presence of 1.57 mM Fe^{2+}/Fe^{3+} redox probe, on laser scribed GO and GO-FA electrode, before and after modification with 3 µL of 7.6 ng/mL FR.

It was suspected that the position of the electrodes on the DVD during laser scribing might affect the net basal current of the electrodes. It was challenging to achieve a homogeneous laser reduction. Reproducibility of laser scribed GO and GO-FA electrodes with same basal currents was also another challenge. Because of these, an experiment to determine the effect of the position of the electrodes on the DVD and net basal current of the electrodes was carried out.

Two sets of complete laser reduction were performed to prepare laser scribed GO and GO-FA electrodes, respectively. From Figure 5.13A, only 13 electrodes out of 48 laser-scribed GO electrodes were functional (shows CV response, gave DPV signal of >2.00 x 10^{-6} A). In contrast, only 23 electrodes out of 48 laser-scribed GO-FA electrodes were functional (showed CV response, gave DPV signal of >2.00 x 10^{-6} A) (Figure 5.13B). The reproducibility of functional laser scribed GO, and GO-FA electrodes was 27 % and 48 %, respectively.

It was observed that the surface layers on the MF were brittle when removed from the DVD drive. The layers were detached from the MF. Treating the MF with plasma cleaner for 3-5 min before filtration did not help prevent the detachment of the reduced surface layers.

It was deduced that the laser reduction efficiency and resultant basal current were not dependant on the position of the electrodes on the DVD during each round of laser reduction. The electrochemical performances of the electrodes from the fixed position on the DVD during laser scribing were not consistent. However, the variation in laser-scribed electrodes was reduced to a minimum by grouping the functional electrodes (in batches) with almost similar basal signals for modification with FR.

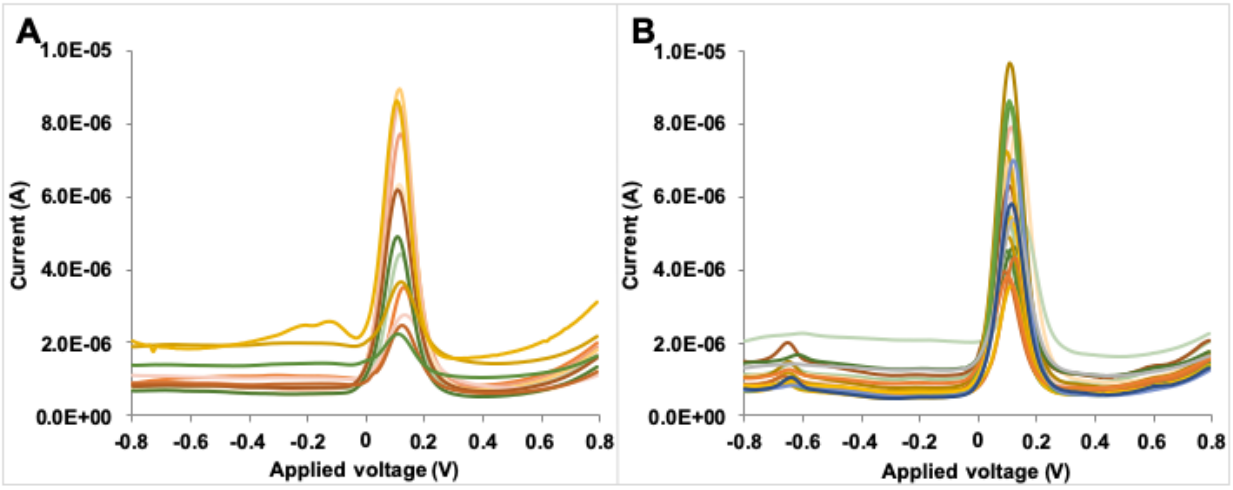

Figure 5.13 Reproducibility of laser scribed GO and GO-FA electrodes. DPV curve of (A) 13 laser scribed GO electrodes and (B) 23 laser scribed GO-FA electrodes in 1.57 mM Fe^{2+}/Fe^{3+} redox probe.

DPV obtained after modification of SPEs with 3 µL of 7.6 ng/mL FR is presented in Figure 5.14. An increase in current of about 17.9±8.4 % was observed in SPEs after modification with FR. It was deduced that FR interacted with Fe^{2+}/Fe^{3+} redox probe and increased the charge transfer. However, ideally, no change in current should be observed since there was no presence of FA for interaction with FR. This preliminary investigation

showed that FR could interact with Fe^{2+}/Fe^{3+} redox probe, although the mechanism/principle behind requires further explanation.

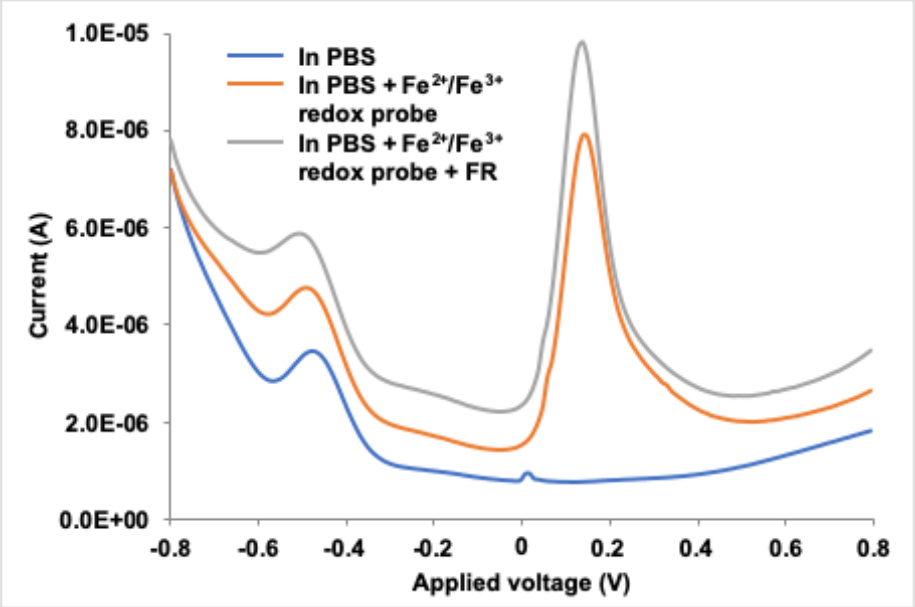

Figure 5.14 DPV curves of SPEs in PBS, Fe^{2+}/Fe^{3+} redox probe and after addition of 3 µL of 7.6 ng/mL FR.

5.4.7. Investigation on the sensitivity of the laser-scribed GO electrodes, in comparison to SPEs

From Figure 5.15, the sensitivity of the SPEs and laser-scribed GO electrodes towards Fe^{2+}/Fe^{3+} redox probe, when applied at a constant voltage, were about 0.0024 $A.M^{-1}$ and 0.0016 $A.M^{-1}$, respectively. The peaks observed when the applied potential is 0-0.5 V in DPV of laser-scribed GO electrodes (as shown in Figure 5.15C), could be due to oxidation of silver inks. Generally, the average sensitivity of the laser-scribed GO electrodes was good with a sensitivity range between 0.0006-0.0016 $A.M^{-1}$. At increasing the concentrations of the redox probe, the maximum peak current obtained for all electrodes were observed to respond to the increasing trend.

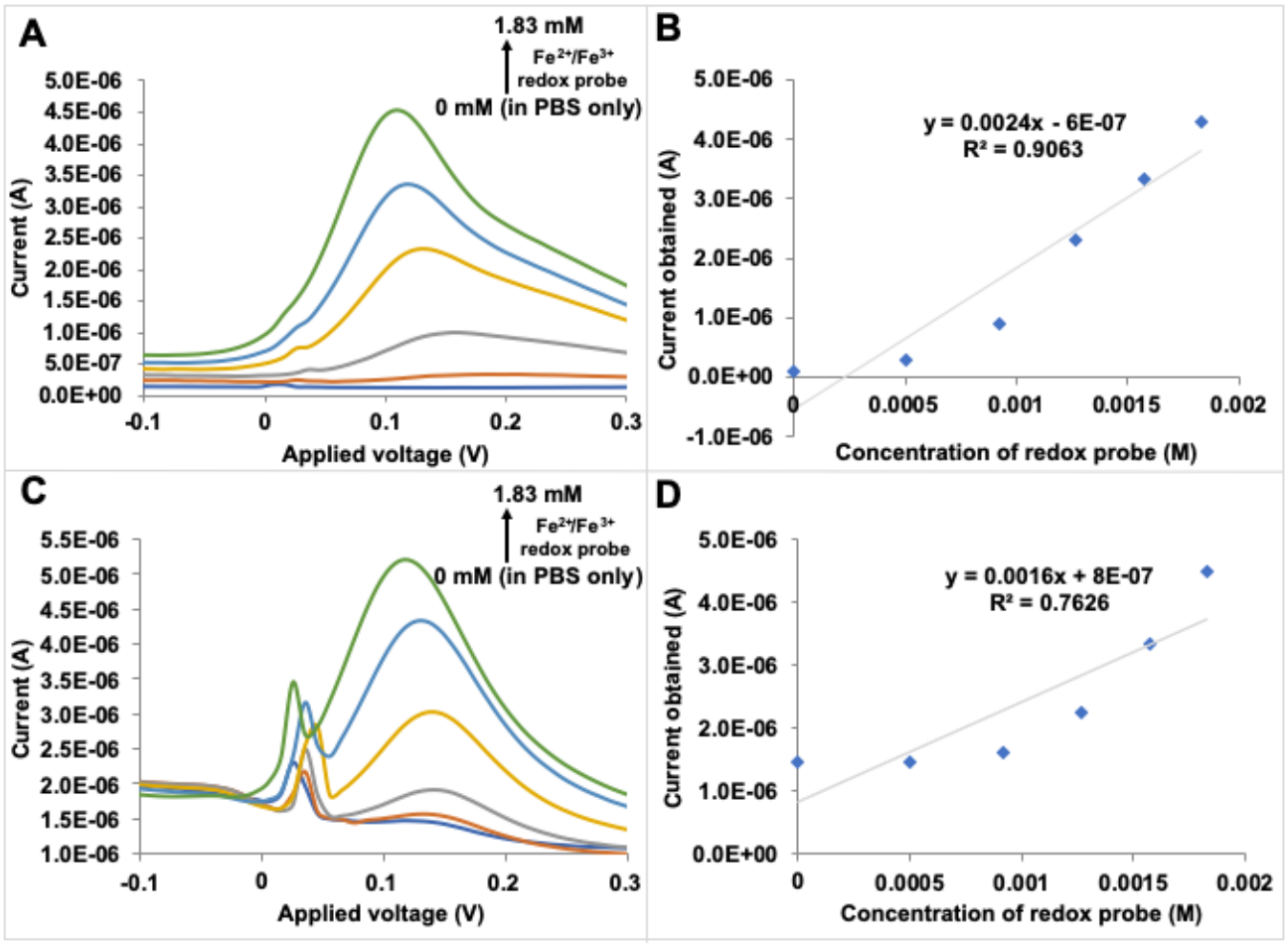

Figure 5.15 Sensitivity of the laser-scribed GO electrodes in comparison to the SPEs. (A) DPV and (B) The current of SPEs, when applied at the voltage of 0.12 V, after addition of redox probe at different concentrations. (C) DPV and (D) The current of laser-scribed GO electrodes, when applied at the voltage of 0.0862 V, after addition of redox probe at different concentrations. The relative concentrations of Fe^{2+}/Fe^{3+} redox probe were 0, 0.50, 0.92, 1.27, 1.57 and 1.83 mM.

5.4.8. Effects of light exposure and laser scribing on FA

From Figure 5.16A, no differences were observed in the absorbance of the FA before and after illumination. FA is usually inactivated by UV light (10-380 nm) while the laser diodes in DVDs is about 650 nm. It was unnecessary to protect the specimens from light before conducting vitamin B_{12} and folate analysis[191]. As shown in Figure 5.16B, no scribe marks

or any burnt areas were observed on the MFs after the laser scribing. This was because the power from the laser diodes used in DVD burner is weak, which was only 5 mW. Therefore, the preliminary tests further supported that the laser from DVD drive will not destroy the structure of FA.

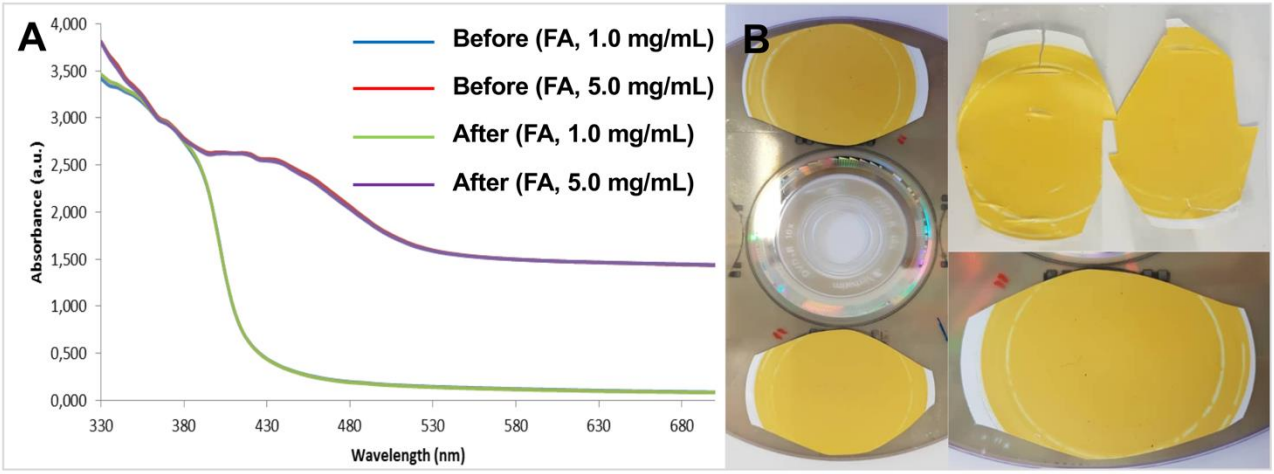

Figure 5.16 Effects of light exposure on FA. (A) Absorbance spectrum of the 1 and 5 mg/mL FA before and after illumination. (B) MFs loaded with FA, after subjecting to 5-reduction steps of laser scribing using DVD drive.

5.4.9. XPS characterisation of the laser scribed GO and GO-FA electrodes

The results obtained for XPS of the laser scribed GO and GO-FA electrodes were presented in Table 4. C peak for laser scribed GO-FA electrode was broader than the laser scribed GO electrode. This could be due to the presence of C-O and C-N bond. Laser scribed GO electrode could have undergone reduction more than laser scribed GO-FA electrode.

O peak for laser scribed GO-FA electrode was higher than the laser scribed GO electrode. It was suspected due to the presence of the C-O bond, as the shoulder O peaks were observed. Laser scribed GO-FA electrode was more oxidised than the laser scribed GO electrode.

N peak was observed in the laser scribed GO-FA electrode, but not in the laser scribed GO electrode. The presence of N peak can be attributed to the glutamic acid in the FA[192]. The presence of Na peak was observed in the laser scribed GO-FA electrode too. This could be due to the solvent (PBS) of FA which contained 0.01 M phosphate buffer, 0.0027 M KCl, 0.137 M NaCl at pH 7.4, 25 °C.

The results obtained for XPS of the MF were as shown in Table 4. The O content on both samples (a mixture of GO-FA dissolved in PBS and deionised water, respectively) were higher than the laser scribed GO electrode, since the GO on the MFs were not subjected to laser reduction.

Charging was observed in both samples as GO was less conductive than rGO. Some artefacts were observed in the C1s peak of the mixture of GO-FA dissolved in deionised water. The elemental peaks of O1s and N1s appeared to be symmetry in both the mixture of GO-FA dissolved in PBS and deionised water.

Overall, both the laser scribed GO, and GO-FA electrodes were reduced with mostly sp2 peak. The efficiency of laser reduction was confirmed. In addition, the presence of FA in the laser scribed GO-FA electrode was confirmed by XPS. However, doubts remain if FA has any chemical interaction with GO, or it was simply present on the electrode. XPS characterisation provided a positive interpretation. The elemental compositions present on the two pieces of MFs were almost similar. Since XPS could only detect the surface of the membrane up to 6-7 nm, more detailed analysis, such as SEM/EDX, can be performed to understand the interactions between FA and GO.

Table 4 XPS results obtained for working electrodes of laser scribed GO, and GO-FA electrodes, as well as MF filtered with a mixture of GO-FA, dissolved in PBS and deionised water.

Samples	Primary XPS region	Binding energy (eV)	Peak area results, % [ ]
Working electrode of the laser scribed GO electrode	C1s	284.34	87.405
	O1s	533.09	11.724
	N1s	399.74	0.870
Working electrode of the laser scribed GO-FA electrode	C1s	284.6	84.792
	O1s	532.6	13.222
	N1s	400.6	1.986
MF filtered with a mixture of GO-FA dissolved in PBS	C1s	284.85	68.221
	O1s	531.75	30.927
	N1s	398.80	0.852
MF filtered with a mixture of GO-FA dissolved in deionised water	C1s	284.84	67.519
	O1s	530.84	31.595
	N1s	399.34	0.885

5.4.10. Electrochemical reversibility studies of Fe^{2+}/Fe^{3+} redox probe on SPEs, laser-scribed GO and GO-FA electrodes

From Figure 5.17A, a good linear fit graph was obtained for the plot of peak currents against the square root of scan rates for all the electrodes. This proved that the electron transfer was homogeneous, and the system has freely diffusing redox species. In other words, it was less likely that the analyte (in this case is redox species) adsorbed onto the electrodes before charge transfer.

For a complete reversible electron transfer, the peak potential will not change with scan rates. It was observed that when the scan rate was increased, the oxidative peak potential shifted to a more positive potential; in contrast, the reductive peak potential shifted to a more negative potential, as presented in Figure 5.17B. As shown in Figure 5.17C, the anodic and cathodic peak-peak separation seemed to drift to higher potentials

with increased scan rates. This indicates that a slower redox reaction is taking place on the electrode's surface.

For successive scans, the reduction of wave potential was observed. This could be due to the concentration of the analyte, which was not completely replenished in the short time duration; hence equilibrium on the electrode's surface was not rapidly established. Therefore, it took a longer time and higher potential for a scan to cycle.

The electron transfer kinetics of the Fe^{2+}/Fe^{3+} redox probe can be influenced by the presence and charge state of surface carboxylate groups on the electrodes[193]. Therefore, it was also possible that the surface of the electrode interacts with the redox probe.

In Figure 5.17D, the oxidation peak current obtained for all the electrodes varied with the number of CV scan cycles. In general, the current obtained at the 3rd round of CV cycles seemed to be more stable. The number of CV cycles also depends on the reversibility of the electron transfer. Moreover, in all the previous experiment, only the results obtained for DPV (not CV) were taken into consideration. Therefore, it is hard to conclude that the number of CV cycles was contributing to a higher deviation.

In short, the study of surface sensitivity of electrochemical responses using Fe^{2+}/Fe^{3+} as redox probe was tricky. The kinetics of the redox reaction could affect the peak current/potential of the electrodes. Future work can be conducted by repeating the experiment with the use of $Ru(NH_3)_6Cl_3$ as the redox probe.

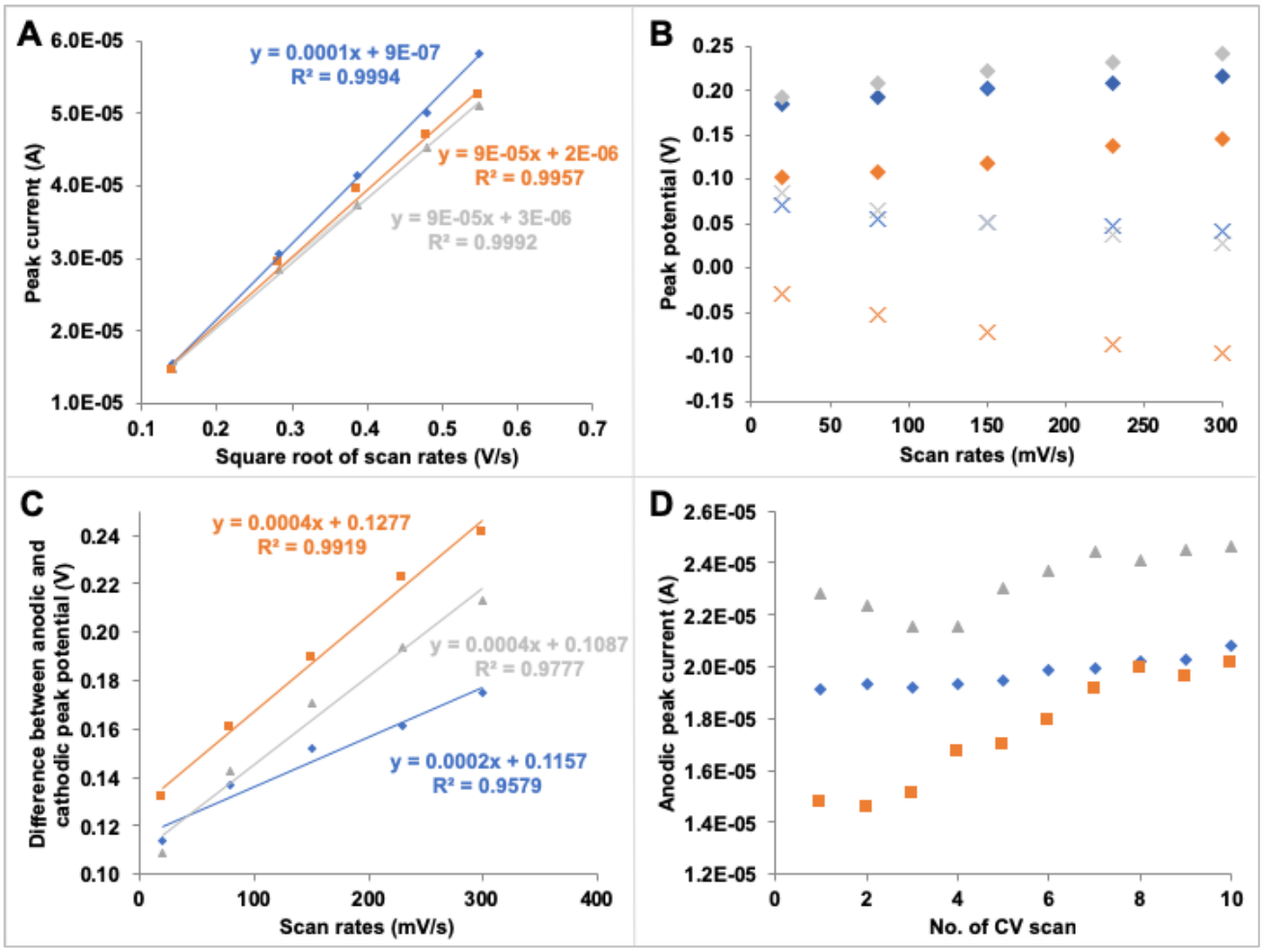

Figure 5.17 Electrochemical reversibility studies of the use of Fe^{2+}/Fe^{3+} redox probe on SPEs, laser-scribed GO and GO-FA electrodes. (A) Peak current against the square root of different scan rates of the SPEs (blue line), laser-scribed GO (orange line) and GO-FA electrodes (grey line). (B) Anodic (represented in diamond-shaped) and cathodic peak (represented in the cross) current of the SPEs (blue), laser-scribed GO (orange) and GO-FA electrodes (grey) at different scan rates. (C) Peak-to-peak separation (anodic and cathodic peak potential) against different scan rates of the SPEs (blue line), laser-scribed GO (orange line) and GO-FA electrodes (grey line). (D) Signal stability test: Anodic peak current of the SPEs (blue), laser-scribed GO (orange) and GO-FA electrodes (grey) at 10 different CV scan cycles.

5.4.11. CV studies of SPEs, laser-scribed GO and GO-FA electrodes with the use of $Ru(NH_3)_6Cl_3$ as a redox probe

A few deductions were made from the results obtained from CV. It was found that with the use of $Ru(NH_3)_6Cl_3$ as a redox probe, the decrease in the cathodic current of both laser-scribed GO and GO-FA electrodes were much lower and consistent than Fe^{2+}/Fe^{3+} redox probe. The current reduction for both laser-scribed GO and GO-FA electrodes were almost similar, which was about 8.1±3.1 % and 8.8±1.1 %, respectively. However, the results obtained for all the SPEs show a slightly bigger STD than the average.

The results obtained for both types of laser-scribed GO and GO-FA electrodes were better than SPEs. This was because $Ru(NH_3)_6Cl_3$ redox probe is an outer-sphere probe with fast electron transfer. Such redox probes are influenced by the electronic structure (density of states and the Fermi level) of the electrode surface only[189]. On the other hand, Fe^{2+}/Fe^{3+} redox probe is an inner-sphere probe. Inner-sphere probes are influenced by both the electronic structure and the electrode's surface. The electron transfer rates also change with the surface functional groups (adsorption sites) and surface chemistry[193]. Given that $Ru(NH_3)_6Cl_3$ is a near-ideal outer-sphere electron transfer redox probe, for future studies, it is suggested to determine a wider range of FR, using CV and EIS with $Ru(NH_3)_6Cl_3$ as a redox probe.

5.4.12. Reproducibility of laser scribed GO-FA electrodes and its effect on the addition of FR in $Ru(NH_3)_6Cl_3$ redox probe

As shown in Figure 5.18A and 5.18B, the initial CV and DPV signals for all the laser scribed GO-FA electrodes were very consistent and reproducible (up to 96 %), when using $Ru(NH_3)_6Cl_3$ as a redox probe. The average cathodic and anodic current obtained using CV were about -6.8E-06±2.4E-07 A and 1.1E-05±1.5E-07 A, respectively. For DPV, the basal current was at -9.5E-06±7.6E-07 A.

For CV, a decrease in current was observed for most electrodes after modification with FR, with a bigger change in the cathodic peak than the anodic peak. The results for modification with 1.0 and 10.0 ng/mL of FR were consistent.

However, for DPV, an increase of current was observed for most of the electrodes after modification with FR. The difference before and after modifications were not significant, as compared to CV.

As mentioned in the experimental section, all the electrodes were divided into four groups, with five electrodes in each group. Each group of electrodes were subjected to modification with different concentrations of FR, which were 0.1, 1.0, 10.0 and 40.0 ng/mL, respectively. For EIS, not all the electrodes in each group gave consistent results and showed significant changes in EIS signals after modification with FR. The semicircle in the high-frequency region almost disappeared, suggesting that the electrode reaction was controlled by a diffusion-limited process. The charge transfer resistance was also high.

In short, the reproducibility of the laser scribed GO-FA electrodes with the use of $Ru(NH_3)_6Cl_3$ as a redox probe was confirmed. However, more optimisation work is needed to determine the interaction between FR and reduced FA on the laser scribed GO-FA electrodes.

Future work can focus on studying the electrochemical reversibility of the $Ru(NH_3)_6Cl_3$ redox probe; comparing the data obtained with both Fe^{2+}/Fe^{3+} and $Ru(NH_3)_6Cl_3$ redox probe; obtaining a calibration curve before and after modification with FR and modifying the electrodes with higher concentrations of FRs (such as more than 40 ng/mL) for proof-of-concept.

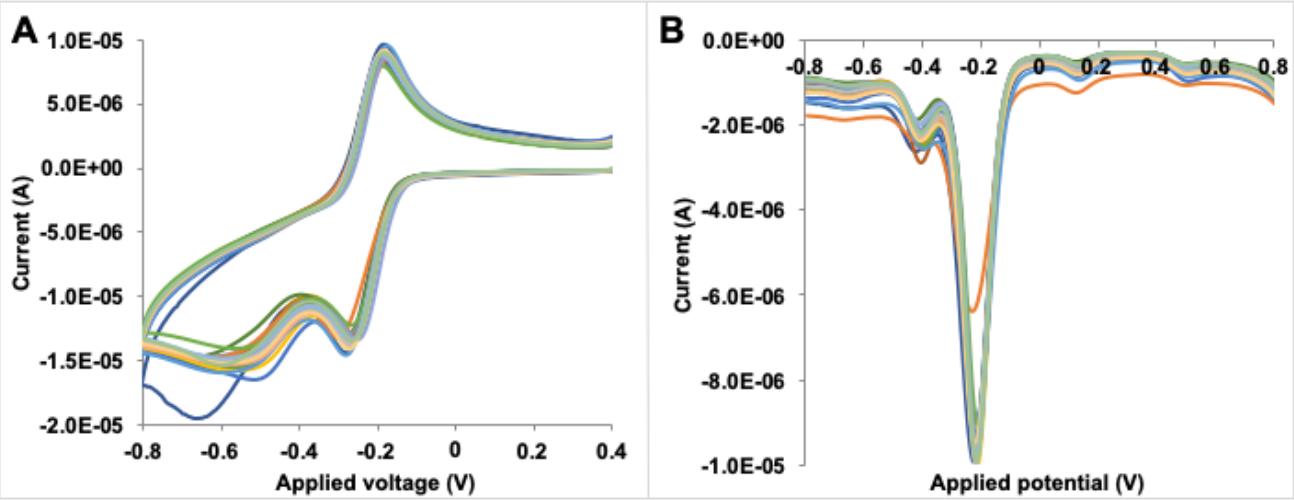

Figure 5.18 Reproducibility of laser scribed GO-FA electrodes in $Ru(NH_3)_6Cl_3$ redox probe. (A) CV and (B) DPV of the laser scribed GO-FA electrodes prior to any modification with FR.

5.4.13. Modification on the surface of working electrodes of SPEs with polymers

The results obtained after the modification of the surface of working electrodes of SPEs with PVA and PEG were discussed.

5.4.13.1. Modification on the surface of working electrodes of SPEs with PVA

For CV, a reduction of cathodic current was observed for all the SPEs after modification with PVA. The cathodic current of the SPEs modified with FA in PBS, and deionised water was reduced to about 11.9±1.0 % and 15.2±0.1 %.

PVA was found to reduce the anodic current of the SPEs to about 12.8±0.3 %. STD of anodic currents was found to be smaller as compared to the cathodic current of the SPEs modified with PVA. The mixture of PVA-FA dissolved in deionised water shows an increase in anodic current by 8.6±1.4 %. Reduction of the anodic current of FA dissolved in PBS (by 4.7±0.5 %) was higher than FA dissolved in deionised water (by 0.5±1.4 %).

For DPV, an increase in current was observed for all groups of SPEs. The SPEs with PVA, a mixture of PVA-FA dissolved in PBS, a mixture of PVA-FA dissolved in deionised water show an increase of 35.7±0.2 %, 39.8±7.9 % and 49.1±12.1 %, respectively.

Potential of the SPEs was not changed when modified the surface of working electrodes with FA dissolved in deionised water and PBS. The results obtained with DPV were more consistent than the CV.

It was suspected that PVA film was removed or interacted with the $Ru(NH_3)_6Cl_3$ redox probe. The film appeared to be removed after a 2nd wash using deionised water. There was an additional peak observed for DPV of the SPEs modified with FA.

5.4.13.2. Modification on the surface of working electrodes of SPEs with PEG

For DPV, modification on the surface of working electrodes with PEG increased the current at about 11.4±8.9 %. In the presence of PEG, an increase in current for SPEs modified with FA dissolved in deionised water (50.1±9.9 %) was higher (almost double) than FA dissolved in PBS (21.6±9.8 %). STD obtained for the triplicates of SPEs after modification with PEG was high (about 8.8-9.8 %), even though all the SPEs have shown an increase in current.

In short, modification of the surface of working electrodes with PVA and PEG improved the electrical conductivity of the SPEs. However, PVA and PEG film could interact with the redox probe and be removed after 2nd or 3rd wash with deionised water. It was found that subjecting the SPEs to 5 min of plasma cleaning prior to use is not ideal. Plasma cleaning increased the hydrophilicity of the SPEs, made the analyte dispersed easily and not possible to be trapped on the surface of the working electrodes.

5.5. Conclusions

In the previous chapters, a facile and optimised protocol for the synthesis of fluorescent BSA/AuNCs and RNase A/AuNCs was developed. Different characterisation tests for BSA/AuNCs and RNase A/AuNCs were conducted. In chapter 3, we reported a novel

nanobiosensor composed of BSA/AuNCs, rGO and FA for sensitive and selective detection of GSH. The nanosensing of GSH was based on "turn-off" fluorescence. In chapter 4, RNase A/AuNCs were integrated with FA and rGO for sensing of metal ions (Na^+ and K^+), based on "turn-off/turn-on" fluorescence strategy.

This chapter began with covalent conjugation of FA onto BSA/AuNCs. This was to determine the effect of the conjugation of FA onto BSA/AuNCs *via* EDC/NHS, and its potential as an FR targeting agent. However, it was found that the use of EDC and NHS linkers quenched the fluorescence intensity of BSA/AuNCs. FA was found to be able to act as a fluorescence quencher for BSA/AuNCs, without the need of GO platform. It was, therefore, deduced that the use of FA-conjugated BSA/AuNCs for targeting of FR could be challenging, as it involved complicated fluorescence mechanism.

Meanwhile, different GO platforms for loading of BSA/AuNCs were studied using several substrates such as glass fibre, photographic paper, plastic, and nitrocellulose membrane. GO acts as a fluorescence quencher for BSA/AuNCs. Development of different GO platforms was challenged by non-homogeneity of the GO. Inspired by the idea that GO and FA may serve as a nanocarrier for delivery of chemotherapy drugs, different electrochemical approaches were employed to investigate the interaction between FA and FR, on a graphene platform.

Different techniques were employed for direct patterning, laser scribing and rGO transfer to several substrates. The aim was to develop a sensitive electrochemical platform for detection of FR. From different trials, laser-scribed GO, and GO-FA electrodes were prepared using laser DVD-burner with a 3-step process. Different optimisation studies were conducted to enhance the reproducibility and functionality of the electrodes. The effect of the addition of FR onto the working electrodes of the laser-scribed GO and GO-FA electrodes were studied and recorded. XPS characterisation confirmed the efficiency

of laser reduction in preparation of both the laser scribed GO and GO-FA electrodes, providing a positive interpretation to the project proposal.

As a proof-of-concept, it is of utmost importance to confirm the interaction between FR and the reduced FA on the laser-scribed GO-FA electrodes. Extended efforts could be put to improve the reproducibility and characterisation of these electrodes, provided that the proposal works. Once the interaction between FA and FR is confirmed, *in vitro* studies can be done. It would be interesting to determine if the FR on the surface of the cancer cells could be detected using laser-scribed GO-FA electrodes. For future studies, RNase A/AuNCs could also be loaded onto the platform, to determine if the RNase A protein could exert therapeutic effects on the cancer cells.

CHAPTER 6

6. Conclusions and future research

The design, development, and application of protein-templated AuNCs in biosensing applications have been achieved within this work. Considering the objectives described in Chapter 2, along with the obtained results presented from Chapter 3 to Chapter 5, the following specific conclusions were achieved in this PhD thesis:

6.1. Integrating gold nanoclusters, folic acid and reduced graphene oxide for nanosensing of glutathione based on "turn-off" fluorescence

GSH is a useful biomarker in the development, diagnosis, and treatment of cancer. However, most of the reported GSH biosensors are expensive, time-consuming, and often require more complex sample treatment, which limits its biological applications. Herein, a nanobiosensor for the detection of GSH using FA-rGO-BSA/AuNCs based on the fluorescence quenching interactions was presented. Firstly, a facile and optimised protocol for the fabrication of BSA/AuNCs was developed. Functionalisation of rGO with FA was performed using EDC/NHS cross-linking reagents, and their interaction after loading with BSA/AuNCs was demonstrated. The formation of FA-rGO, BSA/AuNCs and FA-rGO-BSA/AuNCs were confirmed by the state-of-art characterisation techniques. Finally, a fluorescence "turn-off" sensing strategy was developed using the as-synthesised FA-rGO-BSA/AuNCs for the detection of GSH.

Briefly, the optimised protocol in the present work comes with the advantages of shorter synthesis time (only 6 h), higher QY (10.62 %), need for lower protein amount (only 20 mg mL^{-1}); and employing mild conditions. The protocol is also applicable for the fabrication of AuNCs with different protein templates, not only limited to BSA. In this work, BSA/AuNCs were loaded onto FA-functionalised GO platform. This is the first work done in exploring the potential of FA-rGO not only as a carrier of BSA/AuNCs but also testing its potential as a nanobiosensor. This is the first time that BSA/AuNCs, FA and

rGO were combined for fluorescent sensing of GSH, with a simple experimental process which requires short incubation time (only 2 min). The nanobiosensor revealed an excellent sensing performance for the detection of GSH with high sensitivity and desirable selectivity over other potential interfering species. The fluorescence quenching was linearly proportional to the concentration of GSH between 0-1.75 μM, with a LOD of 0.1 μM under the physiological pH conditions (pH 7.4).

Despite the current GSH nanobiosensor is sensitive to detect the milli-molar concentrations of endogenous GSH in most mammalian cells, further work can be conducted to enhance the biosensing performance of the biosensor, especially in real-life sample detection. Besides, literature has suggested that "turn-on" fluorescence strategy may provide more sensitive results with lower background signal and LOD. Therefore, this work serves as a preliminary study for the design of "turn-on" fluorescence strategy with improved selectivity and sensitivity performance. In future work, the effect of the addition of FR, a promising cancer biomarker, on the FA-rGO-BSA/AuNCs can be investigated. Therefore, this simple approach may grab the attention of researchers further to explore the potential of AuNCs in various biological applications.

6.2. Fluorescence "turn-off/turn-on" biosensing of metal ions by gold nanoclusters, folic acid and reduced graphene oxide

Metal ions homeostasis plays an important role in biological processes. The ability to detect the concentration of metal ions in biological fluids is often challenged by the obvious interference or competitive binding nature of other alkaline metals ions. Common analytical techniques employed for metal ions detection are electrochemical, fluorescence and colorimetric methods. However, most of the reported metal ion sensors involve complicated, time-consuming, and costly procedures with limited effectiveness. Herein, a nanobiosensor for the detection of Na^+ and K^+ ions using FA-rGO-RNase A/AuNCs based on fluorescence "turn-off/turn-on" was presented. Firstly, a facile and

optimised protocol for the fabrication of RNase A/AuNCs was developed. The activity of RNase A protein after the formation of RNase A/AuNCs was studied. RNase A/AuNCs was then loaded onto FA-rGO, in which FA-rGO was used as a potential carrier and fluorescence quencher for RNase A/AuNCs. Finally, a fluorescence "turn-on" sensing strategy was developed using the as-synthesised FA-rGO-RNase A/AuNCs for detection of Na^+ and K^+ ions.

Briefly, the nanobiosensor revealed an excellent sensing performance and met the sensitivity required for the detection of both Na^+ and K^+ ions. However, further work can be focused on the improvement of the sensitivity and selectivity of the nanobiosensor against other alkaline ions in aqueous solutions or complex matrices. This can be achieved by modification of the nanoplatform with metal ion binding ligand or subject the nanoplatform to pretreatment with blocking agents. To the best of our knowledge, this is the first work done on determining the RNase A protein activity in RNase A/AuNCs and exploring the potential application of RNase A/AuNCs as a metal ion sensor. This work serves as a proof-of-concept for combining the potential of drug delivery, active targeting, and therapy on cancer cells as well as biosensing of metal ions into a single platform.

6.3. Development of an electrochemical sensing platform for determination of folate receptor using laser scribed graphene electrodes

This chapter began with covalent conjugation of FA onto BSA/AuNCs. EDC and NHS linkers as well as FA, were found to act as a fluorescence quencher for BSA/AuNCs. The use of FA-conjugated BSA/AuNCs for targeting of FR can be challenging, as it involved complicated fluorescence mechanism. In addition, different GO platforms for loading of BSA/AuNCs were studied using several substrates such as glass fibre, photographic paper, plastic, and nitrocellulose membrane. GO acts as a fluorescence quencher for

BSA/AuNCs. Development of different GO platforms was also challenged by non-homogeneity of the GO.

Different electrochemical approaches (CV, DPV, EIS, CA, *etc*.) were then employed to investigate the interaction between FA and FR, on a graphene platform. Different techniques were employed for direct patterning, laser scribing and rGO transfer to several substrates to develop a sensitive electrochemical platform for detection of FR. From different trials, laser-scribed GO, and GO-FA electrodes were prepared using laser DVD-burner with a 3-step process. Different optimisation studies were conducted to enhance the reproducibility and functionality of the electrodes. The effect of the addition of FR onto the working electrodes of the laser-scribed GO and GO-FA electrodes were studied and recorded.

Briefly, $Ru(NH_3)_6Cl_3$ is more suitable to be used as the redox probe in the present electrochemical measurements than Fe^{2+}/Fe^{3+}. This is because Fe^{2+}/Fe^{3+} is an inner-sphere probe and its electrochemical performance are influenced by the surface functional groups and surface chemistry on both the electronic structure and electrode's surface. It was also suspected that Fe^{2+}/Fe^{3+} redox probe interacted with FA on the working electrodes and affected the electrochemical response. On the other hand, $Ru(NH_3)_6Cl_3$ is an outer-sphere electron transfer redox probe with fast electron transfer. Such redox probes are influenced by the electronic structure of the electrode surface only. The reproducibility of the laser scribed GO-FA electrodes was confirmed with the use of $Ru(NH_3)_6Cl_3$.

Besides, FA improved the electrical conductivity of the electrodes. Interaction of the FR with the reduced FA in the laser scribed GO-FA electrode was briefly confirmed. XPS characterisation confirmed the efficiency of laser reduction in preparation of both the laser scribed GO and GO-FA electrodes. Future work can focus on studying the electrochemical reversibility of the $Ru(NH_3)_6Cl_3$ redox probe; comparing the data

obtained with both Fe^{2+}/Fe^{3+} and $Ru(NH_3)_6Cl_3$ redox probe; obtaining a calibration curve before and after modification with FR and modifying the electrodes with higher concentrations of FRs (such as more than 40 ng/mL) for proof-of-concept. Extended efforts could also be put to improve the reproducibility and characterisation of laser scribed GO and GO-FA electrodes. Once the interaction between FA and FR is confirmed, *in vitro studies* can be done to determine if laser-scribed GO-FA electrodes can be used in the detection of FR on the surface of the cancer cells. RNase A/AuNCs could also be loaded onto the platform, to determine if the RNase A protein could exert therapeutic effects on the cancer cells.

References

1. Lim, E. *et al.* Nanomaterials for theranostics: recent advances and future challenges. *Chemical Reviews* **115**, 327–394 (2015).
2. Patel, K. D., Singh, R. K. & Kim, H. W. Carbon-based nanomaterials as an emerging platform for theranostics. *Materials Horizons* **6**, 434–469 (2019).
3. Thakor, A. S. & Gambhir, S. S. Nanooncology: the future of cancer diagnosis and therapy. *CA: A Cancer Journal for Clinicians* **63**, 395–418 (2013).
4. Kojima, R., Aubel, D. & Fussenegger, M. Novel theranostic agents for next-generation personalized medicine: small molecules, nanoparticles, and engineered mammalian cells. *Current Opinion in Chemical Biology* **28**, 29–38 (2015).
5. Roma-Rodrigues, C. *et al.* Nanotheranostics targeting the tumor microenvironment. *Frontiers in Bioengineering and Biotechnology* **7**, 197 (2019).
6. Nasaruddin, R. R., Chen, T., Yan, N. & Xie, J. Roles of thiolate ligands in the synthesis, properties and catalytic application of gold nanoclusters. *Coordination Chemistry Reviews* **368**, 60–79 (2018).
7. Goswami, N., Yao, Q., Chen, T. & Xie, J. Mechanistic exploration and controlled synthesis of precise thiolate-gold nanoclusters. *Coordination Chemistry Reviews* **329**, 1–15 (2016).
8. Qu, X. *et al.* Fluorescent gold nanoclusters: synthesis and recent biological application. *Journal of Nanomaterials* **2015**, 1–23 (2015).
9. Olesiak-Banska, J., Waszkielewicz, M., Obstarczyk, P. & Samoc, M. Two-photon absorption and photoluminescence of colloidal gold nanoparticles and nanoclusters. *Chemical Society Reviews* **48**, 4087–4117 (2019).
10. Kong, Y. *et al.* Near-infrared fluorescent ribonuclease-A-encapsulated gold nanoclusters: preparation, characterization, cancer targeting and imaging. *Nanoscale* **5**, 1009–17 (2013).

11. Li, H., Li, H. & Wan, A. Luminescent gold nanoclusters for *in vivo* tumor imaging. *Analyst* **145**, 348–363 (2020).
12. Tao, Y., Li, M., Ren, J. & Qu, X. Metal nanoclusters: novel probes for diagnostic and therapeutic applications. *Chemical Society Reviews* **44**, 8636–8663 (2015).
13. Farzin, L., Shamsipur, M., Samandari, L., Sadjadi, S. & Sheibani, S. Biosensing strategies based on organic-scaffolded metal nanoclusters for ultrasensitive detection of tumor markers. *Talanta* **214**, 120886 (2020).
14. Russell, B. A., Kubiak-Ossowska, K., Mulheran, P. A., Birch, D. J. S. & Chen, Y. Locating the nucleation sites for protein encapsulated gold nanoclusters: a molecular dynamics and fluorescence study. *Physical Chemistry Chemical Physics* **17**, 21935–21941 (2015).
15. Chib, R. *et al.* Effect of quencher, denaturants, temperature and pH on the fluorescent properties of BSA protected gold nanoclusters. *Journal of Luminescence* **168**, 62–68 (2015).
16. Wang, Y., Chen, J. & Irudayaraj, J. Nuclear targeting dynamics of gold nanoclusters for enhanced therapy of HER2+ breast cancer. *ACS Nano* **5**, 9718–9725 (2011).
17. Vankayala, R., Gollavelli, G. & Mandal, B. K. Highly fluorescent and biocompatible iridium nanoclusters for cellular imaging. *Journal of Materials Science: Materials in Medicine* **24**, 1993–2000 (2013).
18. Zheng, K., Setyawati, M. I., Leong, D. T. & Xie, J. Surface ligand chemistry of gold nanoclusters determines their antimicrobial ability. *Chemistry of Materials* **30**, 2800–2808 (2018).
19. Genji Srinivasulu, Y., Yao, Q., Goswami, N. & Xie, J. Interfacial engineering of gold nanoclusters for biomedical applications. *Materials Horizons* **7**, 2596–2618 (2020).
20. Akshath, U. S., Bhatt, P. & Singh, S. A. Differential interaction of metal ions with gold nanoclusters and application in detection of cobalt and cadmium. *Journal of*

Fluorescence **30**, 537–545 (2020).

21. Fehér, B. *et al.* Effect of pH on the conformation of bovine serum albumin-gold bioconjugates. *Journal of Molecular Liquids* **309**, 113065 (2020).
22. Putra, R. P., Ikumura, Y., Horino, H., Hori, A. & Rzeznicka, I. I. Adsorption and conformation of bovine serum albumin with blue-emitting gold nanoclusters at the air/water and lipid/water interfaces. *Langmuir* **35**, 16576–16582 (2019).
23. Liu, R., Xiao, W., Hu, C., Xie, R. & Gao, H. Theranostic size-reducible and no donor conjugated gold nanocluster fabricated hyaluronic acid nanoparticle with optimal size for combinational treatment of breast cancer and lung metastasis. *Journal of Controlled Release* **278**, 127–139 (2018).
24. Fu, C., Ding, C., Sun, X. & Fu, A. Curcumin nanocapsules stabilized by bovine serum albumin-capped gold nanoclusters (BSA-AuNCs) for drug delivery and theranosis. *Materials Science and Engineering: C* **87**, 149–154 (2018).
25. Xie, J., Zheng, Y. & Ying, J. Y. Protein-directed synthesis of highly fluorescent gold nanoclusters. *Journal of the American Chemical Society* **131**, 888–889 (2009).
26. Boix, E., Acquati, F., Leonidas, D. & Pulido, D. Role of ribonucleases in immune response regulation during infection and cancer. *Frontiers in immunology* **11**, 236 (2020).
27. Nogués, M. V., Vilanova, M. & Cuchillo, C. M. Bovine pancreatic ribonuclease A as a model of an enzyme with multiple substrate binding sites. *Biochimica et Biophysica Acta (BBA) - Protein Structure and Molecular Enzymology* **1253**, 16–24 (1995).
28. Kong, Y. *et al.* A multifunctional ribonuclease–a–conjugated CdTe quantum dot cluster nanosystem for synchronous cancer imaging and therapy. *Small* **6**, 2367–2373 (2010).
29. Kong, Y. *et al.* Highly fluorescent ribonuclease-A-encapsulated lead sulfide

quantum dots for ultrasensitive fluorescence *in vivo* imaging in the second near-infrared window. *Chemistry of Materials* **28**, 3041–3050 (2016).

30. Ardelt, W., Ardelt, B. & Darzynkiewicz, Z. Ribonucleases as potential modalities in anticancer therapy. *European Journal of Pharmacology* **625**, 181–189 (2009).
31. Dang, W. *et al.* RNase A activity analysis and imaging using label-free DNA-templated silver nanoclusters. *Talanta* **209**, 120512 (2020).
32. Nazir, K. *et al.* Development of gold nanoclusters based direct fluorescence restoration approach for sensitive and selective detection of pesticide. *Applied Nanoscience* **10**, 3411–3420 (2020).
33. Wang, W. *et al.* Engineering the protein corona structure on gold nanoclusters enables red-shifted emissions in the second near-infrared window for gastrointestinal imaging. *Angewandte Chemie International Edition* **59**, 22431–22435 (2020).
34. Krupa, P. *et al.* Dynamics of disulfide-bond disruption and formation in the thermal unfolding of ribonuclease A. *Journal of Chemical Theory and Computation* **13**, 5721–5730 (2017).
35. Likis, F. Folic acid. *Journal of Midwifery & Women's Health* **61**, 673–674 (2016).
36. Yin, J. J. *et al.* Synthesis and biological evaluation of novel folic acid receptor-targeted, β-cyclodextrin-based drug complexes for cancer treatment. *PLoS ONE* **8**, e62289 (2013).
37. Wang, Y., Dai, C. & Yan, X.-P. Fabrication of folate bioconjugated near-infrared fluorescent silver nanoclusters for targeted *in vitro* and *in vivo* bioimaging. *Chemical Communications* **50**, 14341 (2014).
38. Sahoo, A. K. *et al.* Silver nanocluster embedded composite nanoparticles for targeted prodrug delivery in cancer theranostics. *ACS Biomaterials Science & Engineering* **2**, 1395–1402 (2016).

39. Kuo, C.-T., Chang, C. & Lee, W.-S. Folic acid inhibits COLO-205 colon cancer cell proliferation through activating the FRα/c-SRC/ERK1/2/NFκB/TP53 pathway: *in vitro* and *in vivo* studies. *Scientific Reports* **5**, 11187 (2015).

40. Wang, D. *et al.* Multi-layered tumor-targeting photothermal-doxorubicin releasing nanotubes eradicate tumors: *in vivo* with negligible systemic toxicity. *Nanoscale* **10**, 8536–8546 (2018).

41. Shi, X. *et al.* Fabrication and characterization of a folic acid-bound 5-fluorouracil loaded quantum dot system for hepatocellular carcinoma targeted therapy. *RSC Advances* **8**, 19868–19878 (2018).

42. Low, P. S., Henne, W. A. & Doorneweerd, D. D. Discovery and development of folic-acid-based receptor targeting for imaging and therapy of cancer and inflammatory diseases. *Accounts of Chemical Research* **41**, 120–129 (2008).

43. Zwicke, G. L., Ali Mansoori, G. & Jeffery, C. J. Utilizing the folate receptor for active targeting of cancer nanotherapeutics. *Nano Reviews* **3**, 18496 (2012).

44. Luo, Y. *et al.* Engineering graphene oxide with ultrasmall SPIONs and smart drug release for cancer theranostics. *Chemical Communications* **55**, 1963–1966 (2019).

45. Bai, R. G., Ninan, N., Muthoosamy, K. & Manickam, S. Graphene: a versatile platform for nanotheranostics and tissue engineering. *Progress in Materials Science* **91**, 24–69 (2017).

46. Lamb, J., Fischer, E., Rosillo-Lopez, M., Salzmann, C. G. & Holland, J. P. Multi-functionalised graphene nanoflakes as tumour-targeting theranostic drug-delivery vehicles. *Chemical Science* **10**, 8880–8888 (2019).

47. Huang, H. *et al.* Graphene-based sensors for human health monitoring. *Frontiers in Chemistry* **7**, 399 (2019).

48. Raidongia, K., Tan, A. T. L. & Huang, J. Chapter 14 - Graphene Oxide: some new insights into an old material. in *Carbon Nanotubes and Graphene (Second edition)*

(eds. Tanaka, K. & Iijima, S. B. T.-C. N. and G. (Second E.) 341–374 (Elsevier, 2014).

49. Ding, Y.-H. *et al.* Surface adhesion properties of graphene and graphene oxide studied by colloid-probe atomic force microscopy. *Applied Surface Science* **258**, 1077–1081 (2011).

50. Tang, H. *et al.* Theoretical insight into the adsorption of aromatic compounds on graphene oxide. *Environmental Science: Nano* **5**, 2357–2367 (2018).

51. Stankovich, S. *et al.* Synthesis of graphene-based nanosheets via chemical reduction of exfoliated graphite oxide. *Carbon* **45**, 1558–1565 (2007).

52. Shearer, C. J., Slattery, A. D., Stapleton, A. J., Shapter, J. G. & Gibson, C. T. Accurate thickness measurement of graphene. *Nanotechnology* **27**, 125704 (2016).

53. Chen, D., Feng, H. & Li, J. Graphene oxide: preparation, functionalization, and electrochemical applications. *Chemical Reviews* **112**, 6027–6053 (2012).

54. Karimi Shervedani, R., Samiei Foroushani, M., Kefayat, A., Torabi, M. & Rahnemaye Rahsepar, F. Construction and characterization of a theranostic system based on graphene/manganese chelate. *Biosensors and Bioelectronics* **117**, 794–801 (2018).

55. Hwang, D. W. *et al. In vivo* visualization of endogenous miR-21 using hyaluronic acid-coated graphene oxide for targeted cancer therapy. *Biomaterials* **121**, 144–154 (2017).

56. Wong, X. Y., Sena-Torralba, A., Alvarez-Diduk, R., Muthoosamy, K. & Merkoçi, A. Nanomaterials for nanotheranostics: tuning their properties according to disease needs. *ACS Nano* **14**, 2585–2627 (2020).

57. Cheon, Y. A., Bae, J. H. & Chung, B. G. Reduced graphene oxide nanosheet for chemo-photothermal therapy. *Langmuir* **32**, 2731–2736 (2016).

58. Muthoosamy, K., Abubakar, I. B., Bai, R. G., Loh, H.-S. & Manickam, S. Exceedingly

higher co-loading of curcumin and paclitaxel onto polymer-functionalized reduced graphene oxide for highly potent synergistic anticancer treatment. *Scientific Reports* **6**, 32808 (2016).

59. Akhavan, O. & Ghaderi, E. Graphene nanomesh promises extremely efficient *in vivo* photothermal therapy. *Small* **9**, 3593–3601 (2013).
60. Qiu, Y., Huang, J. & Jia, L. A turn-on fluorescent sensor for glutathione based on bovine serum albumin-stabilized gold nanoclusters. *International Journal of Analytical Chemistry* **2018**, 1979684 (2018).
61. Li, R. Selective detection of glutathione based on the recovered fluorescence of BSA-AuNCs/Cu^{2+} system. *Micro & Nano Letters* **14**, 952-956(4) (2019).
62. Akhavan, O. Bacteriorhodopsin as a superior substitute for hydrazine in chemical reduction of single-layer graphene oxide sheets. *Carbon* **81**, 158–166 (2015).
63. Akhavan, O., Ghaderi, E. & Rahighi, R. Toward single-DNA electrochemical biosensing by graphene nanowalls. *ACS Nano* **6**, 2904–2916 (2012).
64. Zhang, L., Xia, J., Zhao, Q., Liu, L. & Zhang, Z. Functional graphene oxide as a nanocarrier for controlled loading and targeted delivery of mixed anticancer drugs. *Small* **6**, 537–544 (2010).
65. Sun, X. *et al.* Nano-graphene oxide for cellular imaging and drug delivery. *Nano Research* **1**, 203–212 (2008).
66. Feng, G., Zhang, G.-Q. & Ding, D. Design of superior phototheranostic agents guided by jablonski diagrams. *Chemical Society Reviews* **49**, 8179–8234 (2020).
67. Li, J. F., Li, C. Y. & Aroca, R. F. Plasmon-enhanced fluorescence spectroscopy. *Chemical Society Reviews* **46**, 3857–4112 (2017).
68. Bourassa, P., Hasni, I. & Tajmir-Riahi, H. A. Folic acid complexes with human and bovine serum albumins. *Food Chemistry* **129**, 1148–1155 (2011).
69. Gu, Y., Wen, Q., Kuang, Y., Tang, L. & Jiang, J. Peptide-templated gold

nanoclusters as a novel label-free biosensor for the detection of protease activity. *RSC Advances* **4**, 13753–13756 (2014).

70. Sha, Q. *et al.* A fluorescence turn-on biosensor based on transferrin encapsulated gold nanoclusters for 5-hydroxytryptamine detection. *Sensors and Actuators B: Chemical* **294**, 177–184 (2019).
71. Bai, Y., Shu, T., Su, L. & Zhang, X. Fluorescent gold nanoclusters for biosensor and bioimaging application. *Crystals* **10**, 357 (2020).
72. Zhang, Y. *et al.* Ultrasmall Au nanoclusters for biomedical and biosensing applications: a mini-review. *Talanta* **200**, 432–442 (2019).
73. Liu, C., Wang, Z., Jia, H. & Li, Z. Efficient fluorescence resonance energy transfer between upconversion nanophosphors and graphene oxide: a highly sensitive biosensing platform. *Chemical Communications (Cambridge, England)* **47**, 4661–4663 (2011).
74. Gaucher, C. *et al.* Glutathione: antioxidant properties dedicated to nanotechnologies. *Antioxidants* **7**, 62 (2018).
75. Fan, H. *et al.* A smart photosensitizer–manganese dioxide nanosystem for enhanced photodynamic therapy by reducing glutathione levels in cancer cells. *Angewandte Chemie International Edition* **55**, 5477–5482 (2016).
76. Zhang, X., Wu, F. G., Liu, P., Gu, N. & Chen, Z. Enhanced fluorescence of gold nanoclusters composed of $HAuCl_4$ and histidine by glutathione: glutathione detection and selective cancer cell imaging. *Small* **10**, 5170–5177 (2014).
77. Desideri, E., Ciccarone, F. & Ciriolo, M. R. Targeting glutathione metabolism: partner in crime in anticancer therapy. *Nutrients* **11**, 1926 (2019).
78. Lin, S., Cheng, H., Ouyang, Q. & Wei, H. Deciphering the quenching mechanism of 2D MnO_2 nanosheets towards Au nanocluster fluorescence to design effective glutathione biosensors. *Analytical Methods* **8**, 3935–3940 (2016).

79. Jahanban-Esfahlan, A. & Panahi-Azar, V. Interaction of glutathione with bovine serum albumin: spectroscopy and molecular docking. *Food Chemistry* **202**, 426–431 (2016).

80. Liou, G.-Y. & Storz, P. Reactive oxygen species in cancer. *Free Radical Research* **44**, 479–496 (2010).

81. Mandal, P. K., Saharan, S., Tripathi, M. & Murari, G. Brain glutathione levels–a novel biomarker for mild cognitive impairment and Alzheimer's disease. *Biological Psychiatry* **78**, 702–710 (2015).

82. Nunes, S. C. & Serpa, J. Glutathione in ovarian cancer: a double-edged sword. *International Journal of Molecular Sciences* **19**, 1882 (2018).

83. Hadipour Moghaddam, S. P., Yazdimamaghani, M. & Ghandehari, H. Glutathione-sensitive hollow mesoporous silica nanoparticles for controlled drug delivery. *Journal of Controlled Release* **282**, 62–75 (2018).

84. Wu, S., Liu, X., Ren, J. & Qu, X. Glutathione depletion in a benign manner by MoS_2-based nanoflowers for enhanced hypoxia-irrelevant free-radical-based cancer therapy. *Small* **15**, 1904870 (2019).

85. García-Fernández, A., Aznar, E., Martínez-Máñez, R. & Sancenón, F. New advances in *in vivo* applications of gated mesoporous silica as drug delivery nanocarriers. *Small* **16**, 1902242 (2020).

86. Giustarini, D. *et al.* Pitfalls in the analysis of the physiological antioxidant glutathione (GSH) and its disulfide (GSSG) in biological samples: an elephant in the room. *Journal of Chromatography. B, Analytical Technologies in the Biomedical and Life Sciences* **1019**, 21–28 (2016).

87. Kurbanoglu, S., Ozkan, S. A. & Merkoçi, A. Nanomaterials-based enzyme electrochemical biosensors operating through inhibition for biosensing applications. *Biosensors and Bioelectronics* **89**, 886–898 (2017).

88. Quesada-González, D. & Merkoçi, A. Nanomaterial-based devices for point-of-care diagnostic applications. *Chemical Society Reviews* **47**, 4697–4709 (2018).

89. Joshi, A. & Kim, K.-H. Recent advances in nanomaterial-based electrochemical detection of antibiotics: challenges and future perspectives. *Biosensors and Bioelectronics* **153**, 112046 (2020).

90. Arduini, F. *et al.* Carbon black as an outstanding and affordable nanomaterial for electrochemical (bio)sensor design. *Biosensors and Bioelectronics* **156**, 112033 (2020).

91. Kong, X.-J., Wu, S., Chen, T.-T., Yu, R.-Q. & Chu, X. MnO_2-induced synthesis of fluorescent polydopamine nanoparticles for reduced glutathione sensing in human whole blood. *Nanoscale* **8**, 15604–15610 (2016).

92. Song, C. *et al.* High peroxidase-like activity realized by facile synthesis of FeS_2 nanoparticles for sensitive colorimetric detection of H_2O_2 and glutathione. *Biosensors and Bioelectronics* **151**, 111983 (2020).

93. Li, Z. *et al.* Carbon dots based photoelectrochemical sensors for ultrasensitive detection of glutathione and its applications in probing of myocardial infarction. *Biosensors and Bioelectronics* **99**, 251–258 (2018).

94. Wang, T., Su, P., Lin, F., Yang, Y. & Yang, Y. Self-sacrificial template synthesis of mixed-valence-state cobalt nanomaterials with high catalytic activities for colorimetric detection of glutathione. *Sensors and Actuators, B: Chemical* **254**, 329–336 (2018).

95. Liu, J. *et al.* MnO_2 nanosheets as an artificial enzyme to mimic oxidase for rapid and sensitive detection of glutathione. *Biosensors and Bioelectronics* **90**, 69–74 (2017).

96. Wang, M. *et al.* Recent advances in glucose-oxidase-based nanocomposites for tumor therapy. *Small* **15**, 1903895 (2019).

97. Halawa, M. I. *et al.* Turn-on fluorescent glutathione detection based on lucigenin and MnO_2 nanosheets. *Journal of Materials Chemistry. B* **8**, 3542–3549 (2020).

98. Wu, M. *et al.* Manganese dioxide nanosheets: from preparation to biomedical applications. *International Journal of Nanomedicine* **14**, 4781–4800 (2019).

99. Gray, E. P. *et al.* Chemical and colloidal dynamics of MnO_2 nanosheets in biological media relevant for nanosafety assessment. *Small* **16**, 2000303 (2020).

100. Zaidi, S. A. & Shin, J. H. A review on the latest developments in nanostructure-based electrochemical sensors for glutathione. *Analytical Methods* **8**, 1745–1754 (2016).

101. Hun, X. *et al.* Photoelectrochemical platform for cancer cell glutathione detection based on polyaniline and nanoMoS_2 composites modified gold electrode. *Biosensors and Bioelectronics* **112**, 93–99 (2018).

102. Rawat, B. *et al.* Two-dimensional MoS_2-based electrochemical biosensor for highly selective detection of glutathione. *IEEE Sensors Journal* **20**, 6937–6944 (2020).

103. Forman, H. J., Zhang, H. & Rinna, A. Glutathione: overview of its protective roles, measurement, and biosynthesis. *Molecular Aspects of Medicine* **30**, 1–12 (2009).

104. Vallet-Regí, M., Colilla, M., Izquierdo-Barba, I. & Manzano, M. Mesoporous silica nanoparticles for drug delivery: current insights. *Molecules* **23**, 47 (2017).

105. Zheng, Z., Huyan, Y., Li, H., Sun, S. & Xu, Y. A lysosome-targetable near infrared fluorescent probe for glutathione sensing and live-cell imaging. *Sensors and Actuators B: Chemical* **301**, 127065 (2019).

106. Mao, X., Yuan, P., Yu, C., Li, L. & Yao, S. Q. Nanoquencher-based selective imaging of protein glutathionylation in live mammalian cells. *Angewandte Chemie - International Edition* **57**, 10257–10262 (2018).

107. Wang, Q. *et al.* Construction of CPs@MnO_2–AgNPs as a multifunctional nanosensor for glutathione sensing and cancer theranostics. *Nanoscale* **11**, 18845–18853

(2019).

108. Wang, Y., Jiang, K., Zhu, J., Zhang, L. & Lin, H. A FRET-based carbon dot–MnO_2 nanosheet architecture for glutathione sensing in human whole blood samples. *Chemical Communications* **51**, 12748–12751 (2015).
109. Tian, D., Qian, Z., Xia, Y. & Zhu, C. Gold nanocluster-based fluorescent probes for near-infrared and turn-on sensing of glutathione in living cells. *Langmuir* **28**, 3945–3951 (2012).
110. Balasubramanian, K. & Swaminathan, H. Highly sensitive sensing of glutathione based on Förster resonance energy transfer between MoS_2 donors and rhodamine 6G acceptors and its insight. *Sensors and Actuators B: Chemical* **259**, 980–989 (2018).
111. Dai, C., Yang, C. & Yan, X. Self-quenched gold nanoclusters for turn-on fluorescence imaging of intracellular glutathione. *Nano Research* **11**, 2488–2497 (2018).
112. Du, Y. *et al.* Protein-assisted formation of gold clusters-MnO_2 nanocomposite for fluorescence imaging of intracellular glutathione. *Talanta* **209**, 120524 (2020).
113. Ding, C., Xu, Y., Zhao, Y., Zhong, H. & Luo, X. Fabrication of BSA@AuNC-based nanostructures for cell fluoresce imaging and target drug delivery. *ACS Applied Materials & Interfaces* **10**, 8947–8954 (2018).
114. Wei, Y., Luan, W., Gao, F. & Hou, X. Supramolecules-guided synthesis of brightly near-infrared Au_{22} nanoclusters with aggregation-induced emission for bioimaging. *Particle & Particle Systems Characterization* **36**, 1900314 (2019).
115. Song, G. *et al.* A mitochondria-targeting NIR fluorescent potassium ion sensor: real-time investigation of the mitochondrial K^+ regulation of apoptosis in situ. *Chemical Communications* **56**, 5405–5408 (2020).
116. Huang, C. C. & Chang, H. T. Aptamer-based fluorescence sensor for rapid detection

of potassium ions in urine. *Chemical Communications* **12**, 1461–1463 (2008).

117. Liu, X. *et al.* Highly sensitive and selective potassium ion detection based on graphene hall effect biosensors. *Materials* **11**, 399 (2018).
118. Kaur, G. & Kaur, N. Estimation of sodium ions using easily engineered organic nanoparticles-based turn-on fluorescent sensor: application in biological and environmental samples. *Sensors and Actuators B: Chemical* **265**, 134–141 (2018).
119. Yuan, Q. *et al.* Sensitivity enhancement of potassium ion (K^+) detection based on graphene field-effect transistors with surface plasma pretreatment. *Sensors and Actuators B: Chemical* **285**, 333–340 (2019).
120. Zhou, X. *et al.* Triazacryptand-based fluorescent sensors for extracellular and intracellular K^+ sensing. *Biomaterials* **32**, 8574–8583 (2011).
121. Liu, Y., Li, B., Cheng, D. & Duan, X. Simple and sensitive fluorescence sensor for detection of potassium ion in the presence of high concentration of sodium ion using berberine-G-quadruplex complex as sensing element. *Microchemical Journal* **99**, 503–507 (2011).
122. Kim, I. *et al.* Two-step energy transfer dynamics in conjugated polymer and dye-labeled aptamer-based potassium ion detection assay. *Polymers* **11**, 1206 (2019).
123. Zainudin, A. A. *et al.* Incorporation of surface plasmon resonance with novel valinomycin doped chitosan-graphene oxide thin film for sensing potassium ion. *Spectrochimica Acta Part A: Molecular and Biomolecular Spectroscopy* **191**, 111–115 (2018).
124. Kumbhat, S. & Singh, U. A potassium-selective electrochemical sensor based on crown-ether functionalized self assembled monolayer. *Journal of Electroanalytical Chemistry* **809**, 31–35 (2018).
125. Zhou, X. *et al.* A new highly selective fluorescent K^+ sensor. *Journal of the American Chemical Society* **133**, 18530–18533 (2011).

126. Benco, J. S., Nienaber, H. A. & Grant McGimpsey, W. A sodium ion sensor based on a covalently-linked aminorhodamine B–calix[4]arene chromoionophore. *Sensors and Actuators B: Chemical* **85**, 126–130 (2002).

127. Kim, E. H., Lee, E.-S., Lee, D. Y. & Kim, Y.-P. Facile determination of sodium ion and osmolarity in artificial tears by sequential DNAzymes. *Sensors* **17**, 2840 (2017).

128. Sun, H. *et al.* Colorimetric detection of sodium ion in serum based on the G-quadruplex conformation related DNAzyme activity. *Analytica Chimica Acta* **912**, 133–138 (2016).

129. Giovannitti, A. *et al.* Sodium and potassium ion selective conjugated polymers for optical ion detection in solution and solid state. *Advanced Functional Materials* **26**, 514–523 (2016).

130. Song, G., Sun, R., Du, J., Chen, M. & Tian, Y. A highly selective, colorimetric, and environment-sensitive optical potassium ion sensor. *Chemical Communications* **53**, 5602–5605 (2017).

131. Naderi, M., Hosseini, M. & Ganjali, M. R. Naked-eye detection of potassium ions in a novel gold nanoparticle aggregation-based aptasensor. *Spectrochimica Acta Part A: Molecular and Biomolecular Spectroscopy* **195**, 75–83 (2018).

132. Wei, W., Xu, C., Ren, J., Xu, B. & Qu, X. Sensing metal ions with ion selectivity of a crown ether and fluorescence resonance energy transfer between carbon dots and graphene. *Chemical Communications* **48**, 1284–1286 (2012).

133. Jiang, Z. *et al.* Ordered mesoporous carbon sphere-based solid-contact ion-selective electrodes. *Journal of Materials Science* **54**, 13674–13684 (2019).

134. Ahn, M.-S., Ahmad, R., Yoo, J.-Y. & Hahn, Y.-B. Synthesis of manganese oxide nanorods and its application for potassium ion sensing in water. *Journal of Colloid and Interface Science* **516**, 364–370 (2018).

135. Li, C., Peng, Y., Wang, H., Liang, A. & Jiang, Z. A nanosol SERS method for

quantitative analysis of trace potassium based on aptamer recognition and silver nanorod catalysis of Ag(I)-glucose reaction. *Sensors and Actuators B: Chemical* **281**, 53–59 (2019).

136. Traiwatcharanon, P., Siriwatcharapiboon, W. & Wongchoosuk, C. Electrochemical sodium ion sensor based on silver nanoparticles/graphene oxide nanocomposite for food application. *Chemosensors* **8**, 58 (2020).
137. Hemmateenejad, B., Shakerizadeh-shirazi, F. & Samari, F. BSA-modified gold nanoclusters for sensing of folic acid. *Sensors and Actuators B: Chemical* **199**, 42–46 (2014).
138. Xu, J., Zeng, F., Wu, H., Yu, C. & Wu, S. Dual-targeting nanosystem for enhancing photodynamic therapy efficiency. *ACS Applied Materials & Interfaces* **7**, 9287–9296 (2015).
139. Vinothini, K., Rajendran, N. K., Ramu, A., Elumalai, N. & Rajan, M. Folate receptor targeted delivery of paclitaxel to breast cancer cells *via* folic acid conjugated graphene oxide grafted methyl acrylate nanocarrier. *Biomedicine & Pharmacotherapy* **110**, 906–917 (2019).
140. Park, Y. H., Park, S. Y. & In, I. Direct non-covalent conjugation of folic acid on reduced graphene oxide as anticancer drug carrier. *Journal of Industrial and Engineering Chemistry* **30**, 190–196 (2015).
141. Hu, C. *et al.* Fabrication of reduced graphene oxide and silver nanoparticle hybrids for Raman detection of absorbed folic acid: a potential cancer diagnostic probe. *ACS Applied Materials & Interfaces* **5**, 4760–4768 (2013).
142. Zhan, L., Zhang, Y., Zeng, Q. L., Liu, Z. De & Huang, C. Z. Facile one-pot synthesis of folic acid-modified graphene to improve the performance of graphene-based sensing strategy. *Journal of Colloid and Interface Science* **426**, 293–299 (2014).
143. Chauhan, G. *et al.* Gold nanoparticles composite-folic acid conjugated graphene

oxide nanohybrids for targeted chemo-thermal cancer ablation: *in vitro* screening and *in vivo* studies. *European Journal of Pharmaceutical Sciences* **96**, 351–361 (2017).

144. Muthoosamy, K. *et al.* Exceedingly biocompatible and thin-layered reduced graphene oxide nanosheets using an eco-friendly mushroom extract strategy. *International Journal of Nanomedicine* **10**, 1505–1519 (2015).
145. Armbruster, D. A. & Pry, T. Limit of blank, limit of detection and limit of quantitation. *The Clinical Biochemist. Reviews* **29**, S49–S52 (2008).
146. Li, H., Cheng, Y., Liu, Y. & Chen, B. Fabrication of folic acid-sensitive gold nanoclusters for turn-on fluorescent imaging of overexpression of folate receptor in tumor cells. *Talanta* **158**, 118–124 (2016).
147. Borzova, V. A. *et al.* Kinetics of thermal denaturation and aggregation of bovine serum albumin. *PLoS ONE* **11**, e0153495–e0153495 (2016).
148. Su, R., Qi, W., He, Z., Zhang, Y. & Jin, F. Multilevel structural nature and interactions of bovine serum albumin during heat-induced aggregation process. *Food Hydrocolloids* **22**, 995–1005 (2008).
149. Russell, B. A., Jachimska, B., Komorek, P., Mulheran, P. A. & Chen, Y. Lysozyme encapsulated gold nanoclusters: effects of cluster synthesis on natural protein characteristics. *Physical Chemistry Chemical Physics* **19**, 7228–7235 (2017).
150. Wang, Y., Chen, J.-T. & Yan, X.-P. Fabrication of transferrin functionalized gold nanoclusters/graphene oxide nanocomposite for turn-on near-infrared fluorescent bioimaging of cancer cells and small animals. *Analytical Chemistry* **85**, 2529–2535 (2013).
151. Meng, H., Yang, D., Tu, Y. & Yan, J. Turn-on fluorescence detection of ascorbic acid with gold nanoclusters. *Talanta* **165**, 346–350 (2017).
152. Gamcsik, M. P., Kasibhatla, M. S., Teeter, S. D. & Colvin, O. M. Glutathione levels

in human tumors. *Biomarkers* **17**, 671–691 (2012).

153. Zhu, S., Wang, X., Cong, Y. & Li, L. Regulating the optical properties of gold nanoclusters for biological applications. *ACS Omega* **5**, 22702–22707 (2020).
154. Zhou, W. *et al.* Ultrastable BSA-capped gold nanoclusters with a polymer-like shielding layer against reactive oxygen species in living cells. *Nanoscale* **8**, 9614–9620 (2016).
155. Xiong, J., Xu, K., Hou, X. & Wu, P. AuNCs-catalyzed hydrogen selenide oxidation: mechanism and application for headspace fluorescent detection of Se(IV). *Analytical Chemistry* **91**, 6141–6148 (2019).
156. Liu, Y., Ai, K., Cheng, X., Huo, L. & Lu, L. Gold-nanocluster-based fluorescent sensors for highly sensitive and selective detection of cyanide in water. *Advanced Functional Materials* **20**, 951–956 (2010).
157. Cui, H., Shao, Z.-S., Song, Z., Wang, Y.-B. & Wang, H.-S. Development of gold nanoclusters: from preparation to applications in the field of biomedicine. *Journal of Materials Chemistry C* **8**, 14312–14333 (2020).
158. Nain, A. *et al.* Tuning the photoluminescence of metal nanoclusters for selective detection of multiple heavy metal ions. *Sensors and Actuators B: Chemical* **321**, 128539 (2020).
159. Qin, X. C. *et al.* Folic acid-conjugated graphene oxide for cancer targeted chemo-photothermal therapy. *Journal of Photochemistry and Photobiology B: Biology* **120**, 156–162 (2013).
160. Chen, T.-H. & Tseng, W.-L. (Lysozyme type VI)-stabilized Au_8 clusters: synthesis mechanism and application for sensing of glutathione in a single drop of blood. *Small* **8**, 1912–1919 (2012).
161. Chen, Z., Lu, D., Cai, Z., Dong, C. & Shuang, S. Bovine serum albumin-confined silver nanoclusters as fluorometric probe for detection of biothiols. *Luminescence*

29, 722–727 (2014).

162. He, H. *et al.* Fluorescent turn-on assay of C-type natriuretic peptide using a molecularly imprinted ratiometric fluorescent probe with high selectivity and sensitivity. *Microchimica Acta* **187**, 614 (2020).
163. Li, Q., Jiang, L., Kamra, T. & Ye, L. Synthesis of fluorescent molecularly imprinted nanoparticles for turn-on fluorescence assay using one-pot synthetic method and a preliminary microfluidic approach. *Polymer* **138**, 352–358 (2018).
164. Zhang, L. *et al.* A chemical covalent tactic for bio-thiol sensing and protein labeling agent design. *Chemical Communications* **56**, 11485–11488 (2020).
165. Yang, J. *et al.* A facile fluorescence assay for rapid and sensitive detection of uric acid based on carbon dots and MnO_2 nanosheets. *New Journal of Chemistry* **42**, 15121–15126 (2018).
166. Vrbka, L., Vondrášek, J., Jagoda-Cwiklik, B., Vácha, R. & Jungwirth, P. Quantification and rationalization of the higher affinity of sodium over potassium to protein surfaces. *Proceedings of the National Academy of Sciences* **103**, 15440–15444 (2006).
167. Wong, X. Y. *et al.* Integrating gold nanoclusters, folic acid and reduced graphene oxide for nanosensing of glutathione based on "turn-off" fluorescence. *Scientific Reports* **11**, 2375 (2021).
168. Phillips, C. M., Mizutani, Y. & Hochstrasser, R. M. Ultrafast thermally induced unfolding of RNase A. *Proceedings of the National Academy of Sciences* **92**, 7292–7296 (1995).
169. Fabian, H. & Mantsch, H. H. Ribonuclease A revisited: infrared spectroscopic evidence for lack of native-like secondary structures in the thermally denatured state. *Biochemistry* **34**, 13651–13655 (1995).
170. Kadonosono, T., Chatani, E., Hayashi, R., Moriyama, H. & Ueki, T. Minimization of

cavity size ensures protein stability and folding: structures of Phe46-replaced bovine pancreatic RNase A. *Biochemistry* **42**, 10651–10658 (2003).

171. Xu, Y. *et al.* The role of protein characteristics in the formation and fluorescence of Au nanoclusters. *Nanoscale* **6**, 1515–1524 (2014).
172. Biter, A. B. *et al.* A method to probe protein structure from UV absorbance spectra. *Analytical Biochemistry* **587**, 113450 (2019).
173. Gotte, G. & Menegazzi, M. Biological activities of secretory RNases: focus on their oligomerization to design antitumor drugs. *Frontiers in Immunology* **10**, 2626 (2019).
174. Shapiro, R. & Vallee, B. L. Site-directed mutagenesis of histidine-13 and histidine-114 of human angiogenin. Alanine derivatives inhibit angiogenin-induced angiogenesis. *Biochemistry* **28**, 7401–7408 (1989).
175. Sun, Q., Wang, X., Cui, C., Li, J. & Wang, Y. Doxorubicin and anti-VEGF siRNA co-delivery *via* nano-graphene oxide for enhanced cancer therapy *in vitro* and *in vivo*. *International Journal of Nanomedicine* **13**, 3713–3728 (2018).
176. Kumawat, M. K. *et al.* Preparation of graphene oxide-graphene quantum dots hybrid and its application in cancer theranostics. *Materials Science and Engineering: C* **103**, 109774 (2019).
177. Gao, G. *et al.* Fluorescent sensors for sodium ions. *Analytical Methods* **9**, 5570–5579 (2017).
178. Cruz-León, S. & Schwierz, N. Hofmeister series for metal-cation–RNA interactions: the interplay of binding affinity and exchange kinetics. *Langmuir* **36**, 5979–5989 (2020).
179. Giacomelli, C., Álvarez-Diduk, R., Testolin, A. & Merkoçi, A. Selective stamping of laser scribed rGO nanofilms: from sensing to multiple applications. *2D Materials* **7**, 24006 (2020).

180. Khan, S., Lorenzelli, L. & Dahiya, R. S. Technologies for printing sensors and electronics over large flexible substrates: a review. *IEEE Sensors Journal* **15**, 3164–3185 (2015).

181. Baptista-Pires, L., de la Escosura-Muñiz, A., Balsells, M., Zuaznabar-Gardona, J. C. & Merkoçi, A. Production and printing of graphene oxide foam ink for electrocatalytic applications. *Electrochemistry Communications* **98**, 6–9 (2019).

182. Parolo, C. & Merkoçi, A. Paper-based nanobiosensors for diagnostics. *Chemical Society Reviews* **42**, 450–457 (2013).

183. Akbar, S., Anwar, A. & Kanwal, Q. Electrochemical determination of folic acid: a short review. *Analytical Biochemistry* **510**, 98–105 (2016).

184. Stinson, D. G. & Maguire, M. LightScribe direct disc labeling. in *International Symposium on Optical Memory and Optical Data Storage* MA4 (Optical Society of America, 2005). doi:10.1364/ISOM_ODS.2005.MA4.

185. Mistry, K. K., Layek, K., Mahapatra, A., RoyChaudhuri, C. & Saha, H. A review on amperometric-type immunosensors based on screen-printed electrodes. *Analyst* **139**, 2289–2311 (2014).

186. Xu, Q., Yan, F., Lei, J., Leng, C. & Ju, H. Disposable electrochemical immunosensor by using carbon sphere/gold nanoparticle composites as labels for signal amplification. *Chemistry – A European Journal* **18**, 4994–4998 (2012).

187. Chiticaru, E. A. *et al.* Influence of graphene oxide concentration when fabricating an electrochemical biosensor for DNA detection. *Biosensors* **9**, 113 (2019).

188. Negishi, R., Akabori, M., Ito, T., Watanabe, Y. & Kobayashi, Y. Band-like transport in highly crystalline graphene films from defective graphene oxides. *Scientific Reports* **6**, 28936 (2016).

189. Negishi, R., Matsui, Y. & Kobayashi, Y. Improving sensor response using reduced graphene oxide film transistor biosensor by controlling the adsorption of pyrene as

an anchor molecule. *Japanese Journal of Applied Physics* **56**, 06GE04 (2017).

190. Gunho, J. *et al.* The application of graphene as electrodes in electrical and optical devices. *Nanotechnology* **23**, 112001 (2012).
191. Clement, N. F. & Kendall, B. S. Effect of light on vitamin B_{12} and folate. *Laboratory Medicine* **40**, 657–659 (2009).
192. Ghosh, M., Gayen, S. & Dey, K. K. An atomic resolution description of folic acid using solid state NMR measurements. *RSC Advances* **10**, 24973–24984 (2020).
193. García-Miranda Ferrari, A., Foster, C. W., Kelly, P. J., Brownson, D. A. C. & Banks, C. E. Determination of the electrochemical area of screen-printed electrochemical sensing platforms. *Biosensors* **8**, 53 (2018).

Supplementary Information

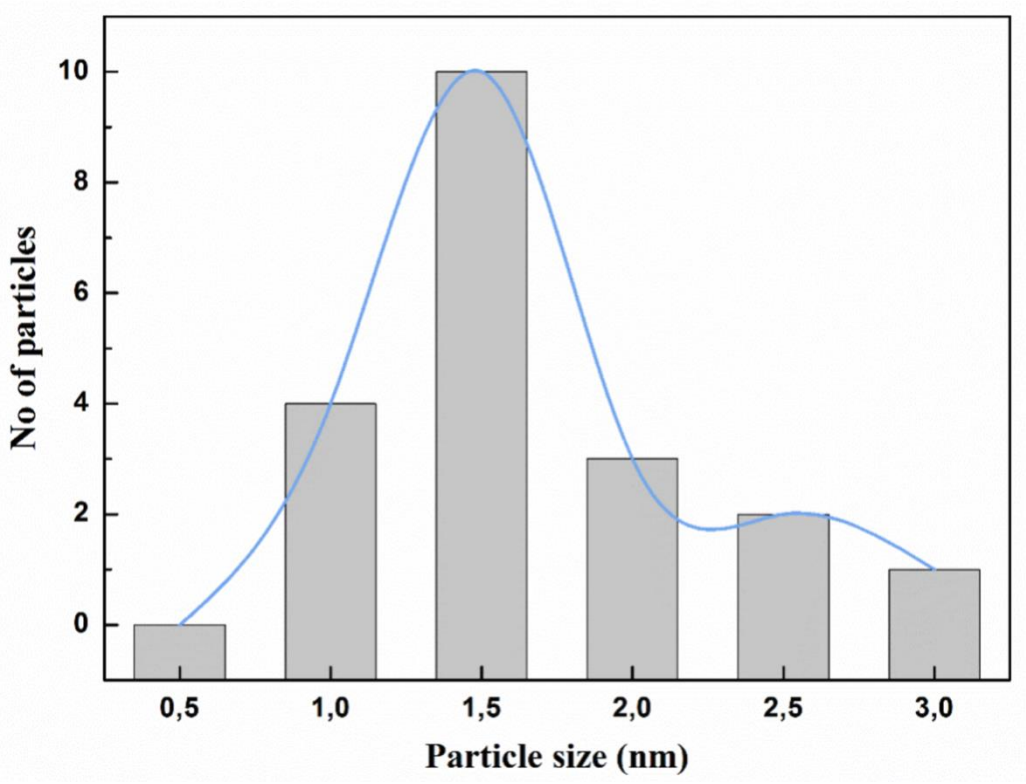

Figure S3.1 Particle size distribution of BSA/AuNCs.

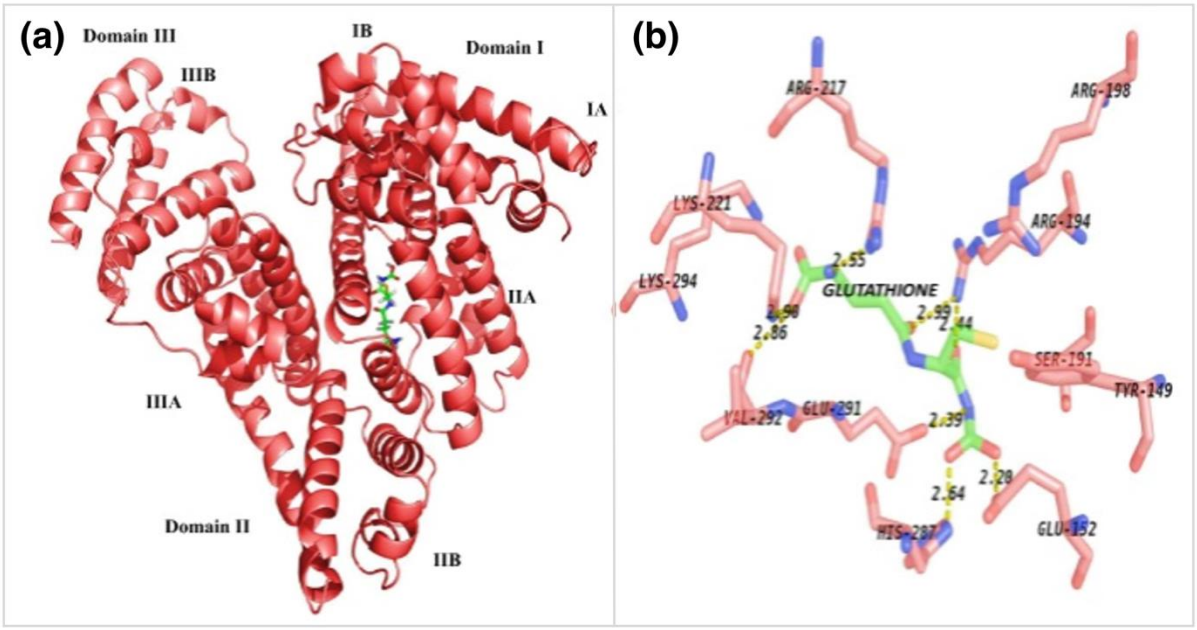

Figure S3.2 Interaction of GSH with BSA. (a) Conformation of the binding mode between GSH and BSA. GSH binds within the site I of sub-domain IIA pocket in the domain II of

BSA. (b) Hydrogen bonds between GSH and amino acid residues of BSA. Reprinted with permission from ref.[60]. Copyright Elsevier, 2016.

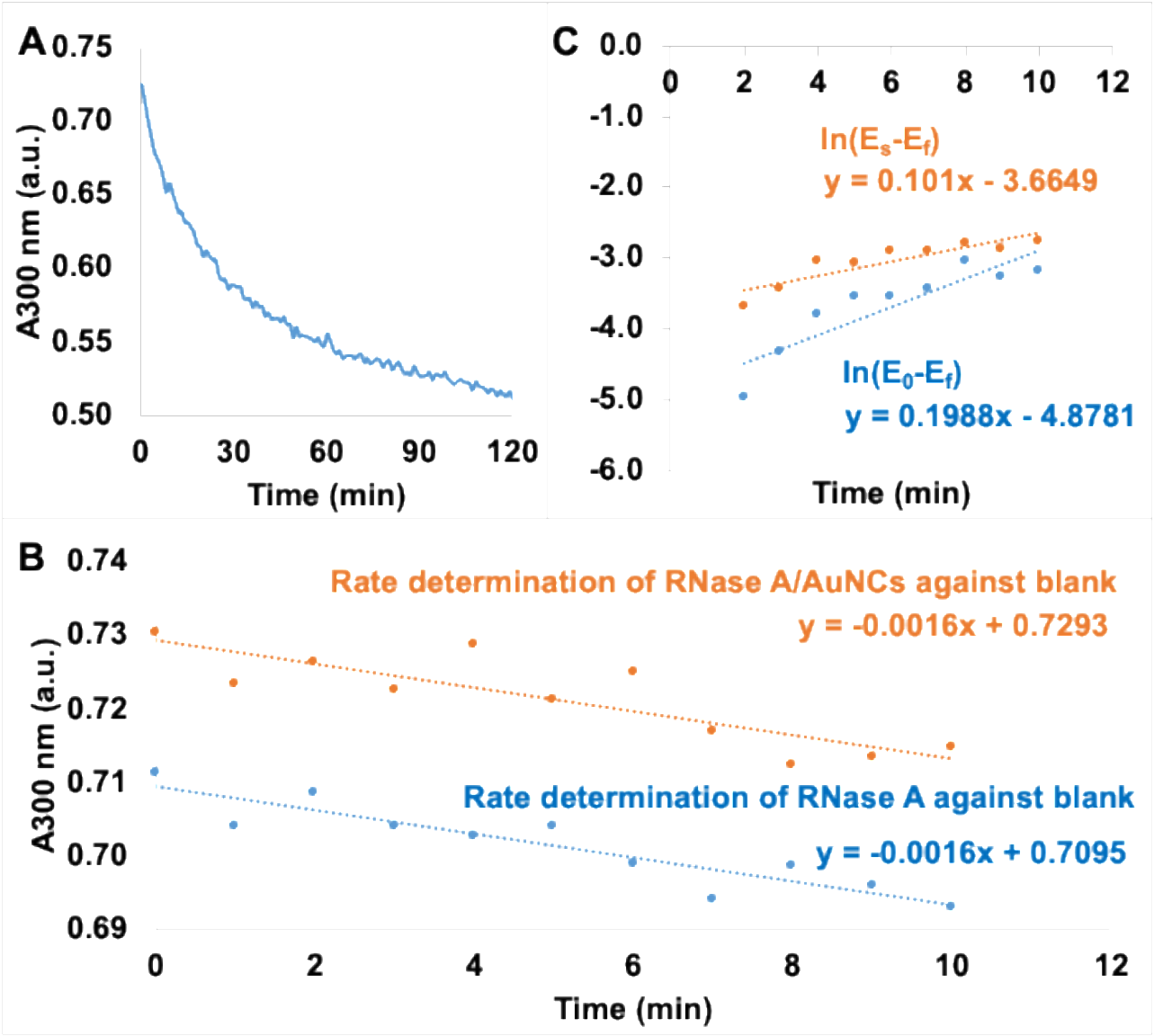

Figure S4.1 RNase A protein activity assay. Representative graph of (A) Total RNase A protein hydrolysis, (B) Rate determination of RNase A (blue line) and RNase A/AuNCs (orange line) against blank and (C) $\ln(E_0-E_f)$ (blue line) and $\ln(E_s-E_f)$ (orange line) against time. E_f is the total hydrolysis, E_0 is the rate determination, and E_s is the rate determination of RNase A/AuNCs samples.

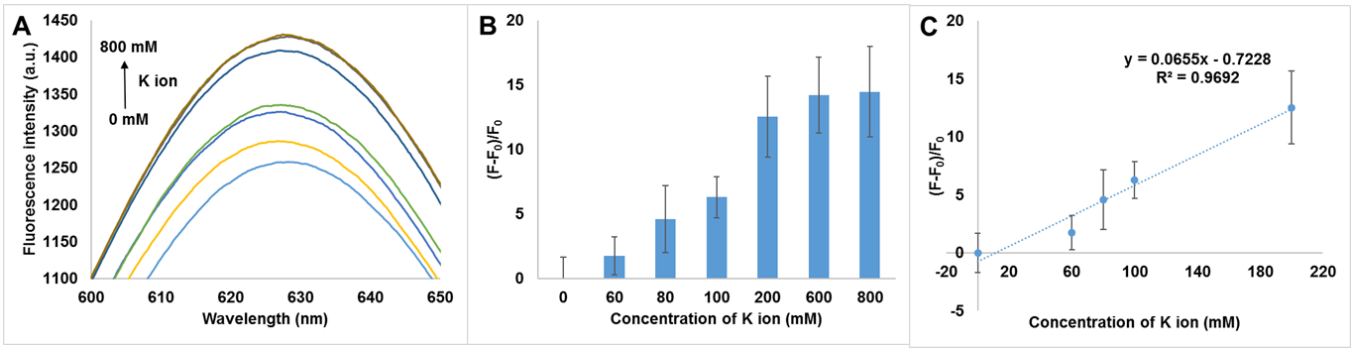

Figure S4.2 Sensitive detection of K^+ using RNase A/AuNCs. (A) Fluorescence intensity of RNase A/AuNCs by varying the concentration of K^+. The relative concentrations of K^+ were 0, 60, 80, 100, 200, 600 and 800 mM at λ_{ex}= 365 nm. (B) Relationship between the fluorescence intensity values $(F-F_0)/F_0$ and the target concentrations. (C) Linear response of the fluorescence intensity values $(F-F_0)/F_0$ to the concentration of K^+. Error bars are the standard deviation of three repetitive experiments.

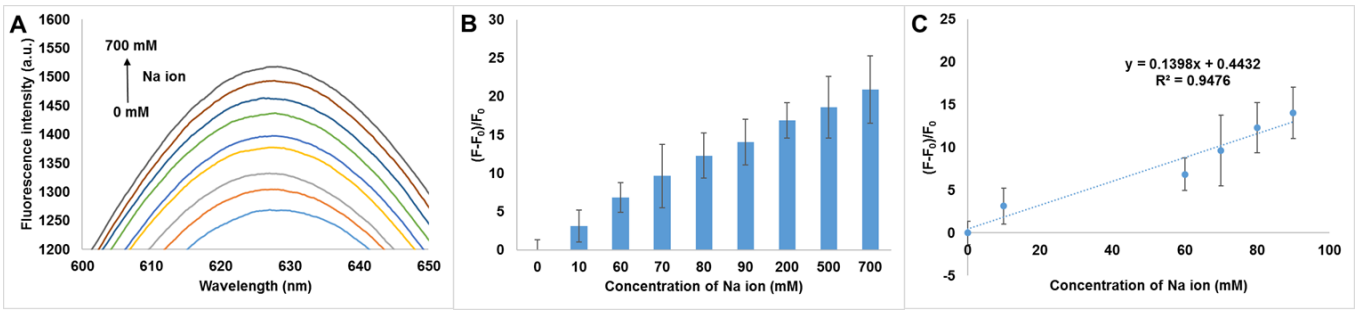

Figure S4.3 Sensitive detection of Na^+ using RNase A/AuNCs. (A) Fluorescence intensity of RNase A/AuNCs by varying the concentration of Na^+. The relative concentrations of Na^+ were 0, 10, 60, 70, 80, 90, 200, 500 and 700 mM at λ_{ex}= 365 nm. (B) Relationship between the fluorescence intensity values $(F-F_0)/F_0$ and the target concentrations. (C) Linear response of the fluorescence intensity values $(F-F_0)/F_0$ to the concentration of Na^+. Error bars are the standard deviation of three repetitive experiments.

Appendix

ACSNANO

www.acsnano.org

REVIEW

Nanomaterials for Nanotheranostics: Tuning Their Properties According to Disease Needs

Xin Yi Wong, Amadeo Sena-Torralba, Ruslan Álvarez-Diduk, Kasturi Muthoosamy,* and Arben Merkoçi*

Cite This: *ACS Nano* 2020, 14, 2585−2627

Read Online

ACCESS | Metrics & More | Article Recommendations

ABSTRACT: Nanotheranostics is one of the biggest scientific breakthroughs in nanomedicine. Most of the currently available diagnosis and therapies are invasive, time-consuming, and associated with severe toxic side effects. Nanotheranostics, on the other hand, has the potential to bridge this gap by harnessing the capabilities of nanotechnology and nanomaterials for combined therapeutics and diagnostics with markedly enhanced efficacy. However, nanomaterial applications in nanotheranostics are still in its infancy. This is due to the fact that each disease has a particular microenvironment with well-defined characteristics, which promotes deeper selection criteria of nanomaterials to meet the disease needs. In this review, we have outlined how nanomaterials are designed and tailored for nanotheranostics of cancer and other diseases such as neurodegenerative, autoimmune (particularly on rheumatoid arthritis), and cardiovascular diseases. The penetrability and retention of a nanomaterial in the biological system, the therapeutic strategy used, and the imaging mode selected are some of the aspects discussed for each disease. The specific properties of the nanomaterials in terms of feasibility, physicochemical challenges, progress in clinical trials, its toxicity, and their future application on translational medicine are addressed. Our review meticulously and critically examines the applications of nanotheranostics with various nanomaterials, including graphene, across several diseases, offering a broader perspective of this emerging field.

KEYWORDS: *nanotheranostics, nanomaterials, cancer, solid tumor, liquid tumor, neurodegenerative diseases, autoimmune diseases, cardiovascular diseases, clinical trials, graphene*

In 2002, John Funkhouser, the PharmaNetics president and CEO, was credited by scientists for introducing the term theranostics (a portmanteau of Therapeutics and Diagnostics), which epitomes the development of nanoparticle (NP) systems for personalized medicine.[1,2] Theranostics (or theragnostics) refers to a comprehensive effort that integrates diagnostics and therapy in a single system/platform.[3,4]

With the emergence of nanotechnologies and nanomaterials, the concept of nanotheranostics was then introduced (Figure 1). Nanotheranostics was able to provide non-invasive imaging, targeting, and therapy at the disease sites, without affecting surrounding healthy cells.[3,5] Hence, the use of empirical treatment can be avoided (therapy given based on experience, usually without a prior definitive medical diagnosis and likely to cause infectious disease), greatly improve the prognoses, and subsequently expedite clinician's therapeutic decisions.

Received: October 15, 2019
Accepted: February 7, 2020
Published: February 7, 2020

https://dx.doi.org/10.1021/acsnano.9b08133
ACS Nano 2020, 14, 2585−2627

scientific reports

OPEN

Integrating gold nanoclusters, folic acid and reduced graphene oxide for nanosensing of glutathione based on "turn-off" fluorescence

Xin Yi Wong[1], Daniel Quesada-González[2], Sivakumar Manickam[1,3,4], Siu Yee New[5], Kasturi Muthoosamy[3]✉ & Arben Merkoçi[6,7,8]✉

Glutathione (GSH) is a useful biomarker in the development, diagnosis and treatment of cancer. However, most of the reported GSH biosensors are expensive, time-consuming and often require complex sample treatment, which limit its biological applications. Herein, a nanobiosensor for the detection of GSH using folic acid-functionalized reduced graphene oxide-modified BSA gold nanoclusters (FA-rGO-BSA/AuNCs) based on the fluorescence quenching interactions is presented. Firstly, a facile and optimized protocol for the fabrication of BSA/AuNCs is developed. Functionalization of rGO with folic acid is performed using EDC/NHS cross-linking reagents, and their interaction after loading with BSA/AuNCs is demonstrated. The formation of FA-rGO, BSA/AuNCs and FA-rGO-BSA/AuNCs are confirmed by the state-of-art characterization techniques. Finally, a fluorescence turn-off sensing strategy is developed using the as-synthesized FA-rGO-BSA/AuNCs for the detection of GSH. The nanobiosensor revealed an excellent sensing performance for the detection of GSH with high sensitivity and desirable selectivity over other potential interfering species. The fluorescence quenching is linearly proportional to the concentration of GSH between 0 and 1.75 µM, with a limit of detection of 0.1 µM under the physiological pH conditions (pH 7.4). Such a sensitive nanobiosensor paves the way to fabricate a "turn-on" or "turn-off" fluorescent sensor for important biomarkers in cancer cells, presenting potential nanotheranostic applications in biological detection and clinical diagnosis.

Glutathione (GSH) is a low molecular weight (307.32 g mol^{-1}) tri-peptide composed of glutamate, cysteine and glycine[1–3]. As an endogenous antioxidant, GSH may scavenge reactive oxygen species, protect cells from oxidative stress and subsequently inhibit cancer progression[1,3,4–7]. GSH levels are found to be elevated in illness/cancers such as Alzheimer's disease[8] as well as ovarian[9], liver[3], lung, colorectal, breast, head and neck cancer patients[10]. Reducing intracellular GSH has been proposed as one of the strategies of cancer treatment[11,12]. Hence, sensing of GSH in the biological samples for diagnosis of diseases is of great interest in biological applications.

Although commercial kits for the detection of GSH are available, there is still a need for a detection platform with the advantages of lower cost, fast response time, more sensitive and essentially stable[13]. The use of nanomaterials in biosensing is becoming popular in recent years due to the improvements in sensitivity and its robustness[14–17] since contrary to enzymes and other biological compounds, nanomaterials are stable in time and do not require, in most of the cases, special storage conditions (i.e. low temperature, buffered medium, etc.). In

[1]Department of Chemical and Environmental Engineering, Faculty of Science and Engineering, University of Nottingham Malaysia, 43500 Semenyih, Selangor, Malaysia. [2]Paperdrop Diagnostics, Av. de Can Domènech s/n, Eureka Building, Campus UAB, 08193 Bellaterra, Barcelona, Spain. [3]Nanotechnology Research Group, Centre of Nanotechnology and Advanced Materials, University of Nottingham Malaysia, 43500 Semenyih, Selangor, Malaysia. [4]Petroleum and Chemical Engineering, Faculty of Engineering, Universiti Teknologi Brunei, Bandar Seri Begawan BE1410, Brunei Darussalam. [5]School of Pharmacy, Faculty of Science and Engineering, University of Nottingham Malaysia, 43500 Semenyih, Selangor, Malaysia. [6]Nanobioelectronics and Biosensors Group, Catalan Institute of Nanoscience and Nanotechnology (ICN2), CSIC, Barcelona, Spain. [7]The Barcelona Institute of Science and Technology (BIST), Campus UAB, 08036 Bellaterra, Barcelona, Spain. [8]ICREA, Institució Catalana de Recerca i Estudis Avançats, Pg. Lluis Companys 23, 08010 Barcelona, Spain. ✉email: Kasturi.Muthoosamy@nottingham.edu.my; arben.merkoci@icn2.cat